

PROPERTIES OF CHARGED-PARTICLE PRODUCTION AT
MID-RAPIDITY FOR AU+AU COLLISIONS AT RHIC ENERGIES

BY

ANETA IORDANOVA

M.Sc. (Sofia University St. Kliment Ohridski) 1994

THESIS

Submitted in partial fulfillment of the requirements
for the degree of Doctor of Philosophy in Physics
in the Graduate College of the
University of Illinois at Chicago, 2005

Chicago, Illinois

Copyright by

Aneta Iordanova

2005

To Richi,

Richard S. Hollis,

the amazing miracle of love in my life.

ACKNOWLEDGMENTS

I would like to thank my thesis committee, Clive Halliwell, Russell Betts, Fleming Videbaeck, Wai-Yee Keung and David Hofman, for carefully reading the manuscript and bringing this work to a conclusion.

I am grateful to Michael Reuter for starting me with this analysis and helping me along the way and to Burt Holzman for guiding my first programming steps. I would like to say thank you to the PHOBOS multiplicity working group for providing support and comments during the analysis for all collision energies: Rachid, Robin, Patrick, Richard, Dave, Peter, Mark and Birger. Also, Marguerite and Iouri for repassing the data. I additionally thank the multiplicity committee for reviewing the analysis for publication of the 19.6 GeV data: Birger Back, Robert Pak and Gunther Roland.

This analysis would not have been possible without the collective work from all members of the PHOBOS collaboration. Thank you all for the great work and providing me support during the pass four years. I want to say a special and very warm thanks to all past and present students and postdocs in PHOBOS. Guys, I really enjoyed working and partying with you.

I am deeply indebted to my advisor, David Hofman, for all the help and support of my analysis and for seeing my Thesis to a conclusion. Thanks.

I want to thank my family and Richard's family for being incredibly supporting during the last five years of our study. Thanks to Richard's mum, Patricia Hollis, for reading the manuscript and helping me with the corrections.

ACKNOWLEDGMENTS (Continued)

I want to thank Richard Hollis, my fellow student and future husband. His analysis on centrality was a major contribution to my thesis. Thanks for helping me and listen to me every single day.

Finally, I would like to thank the UIC physics department for supporting me with a teaching assistantship for the first two years of my graduate study.

This work was partially supported by U.S. DOE grants DE-AC02-98CH10886, DE-FG02-93ER40802, DE-FC02-94ER40818, DE-FG02-94ER40865, DE-FG02-99ER41099, and W-31-109-ENG-38, by U.S. NSF grants 9603486, 0072204, and 0245011, by Polish KBN grant 1-P03B-062-27(2004-2007), and by NSC of Taiwan Contract NSC 89-2112-M-008-024.

TABLE OF CONTENTS

<u>CHAPTER</u>		<u>PAGE</u>
1	INTRODUCTION	1
1.1	Concepts	1
1.2	Background	1
1.3	Goals	3
2	THEORY AND MODEL EXPECTATIONS	5
2.1	The search for a new state of matter	5
2.1.1	Quantum Chromo-Dynamics, QCD	5
2.1.2	QGP	7
2.1.3	Ultra-relativistic heavy ion collisions and the QGP	10
2.2	Description of heavy ion collisions	12
2.2.1	Time-evolution of a nuclear-nuclear collision	12
2.2.2	Description of the collision geometry	14
2.2.3	Soft and hard interactions	16
2.2.3.1	Nucleon-nucleon collisions (NN)	17
2.2.3.2	Nucleus-nucleus collisions (AA)	18
2.3	Models for particle production in heavy ion collisions	20
2.3.1	Two component picture	20
2.3.2	HIJING	21
2.3.3	KLN Saturation model	23
2.4	The motivation for measuring multiplicity	26
3	INITIAL ANALYSIS: TRIGGERING, EVENT SELECTION AND CENTRALITY DETERMINATION	27
3.1	Nomenclature	27
3.2	Trigger system	31
3.2.1	Paddle counters	31
3.2.2	Time Zero counters	32
3.2.3	Čerenkov counters	33
3.2.4	Zero Degree Calorimeters	33
3.2.5	Trigger logic	34
3.2.6	The main triggers for this analysis	34
3.2.7	Trigger and data quality	36
3.3	Silicon based detectors	38
3.3.1	Vertex detector	39
3.3.2	Silicon detectors and data quality	42
3.3.3	Dead and hot channel map	42

TABLE OF CONTENTS (Continued)

<u>CHAPTER</u>		<u>PAGE</u>
3.4	DAQ and software	42
3.4.1	Vertex finders	43
3.5	Event selection	45
3.5.1	200 GeV Au+Au event selection	47
3.5.1.1	Paddle time restrictions	47
3.5.1.2	ZDC time restrictions	49
3.5.1.3	Paddle energy signal	50
3.5.2	62.4 GeV Au+Au event selection	51
3.5.3	19.6 GeV Au+Au event selection	52
3.5.4	Additional event selection criteria	52
3.6	Centrality of the collision	53
3.6.1	Paddle Mean centrality overview ($\sqrt{s_{NN}} = 200$ and 62.4 GeV)	55
3.6.2	EOct centrality overview (all energies)	58
4	TRACKLETS	60
4.1	Reconstruction procedure	60
4.2	Corrections	64
4.2.1	Combinatorial background	67
4.2.2	Acceptance and efficiency correction factor α'	69
4.2.2.1	Geometrical correction component in α'	71
4.2.2.2	Dead/Hot channel correction component in α'	72
4.2.2.3	Reconstruction efficiency component in α'	73
4.2.3	Secondary interactions	74
4.2.4	Decays	75
4.3	Reconstruction	77
4.4	Low centrality studies	79
4.4.1	Vertex reconstruction quality	79
4.4.2	Modifications to the α -matrix	81
4.5	Centrality overview	82
4.5.1	19.6 and 200 GeV	83
4.5.2	62.4 GeV	86
4.6	Tracklet analysis systematic errors	86
4.6.1	Individual measurement	86
4.6.1.1	Tracklet reconstruction uncertainty	87
4.6.1.2	Real and combinatorial background	87
4.6.1.3	Weak decays	88
4.6.1.4	MC generators	89
4.6.1.5	Additional errors	89
4.6.2	Ratio of two datasets	91
4.6.2.1	R_α	92
4.6.2.2	R_β	94
4.6.2.3	$R_{N_{rec}}$	94

TABLE OF CONTENTS (Continued)

<u>CHAPTER</u>		<u>PAGE</u>
4.6.2.4	$R_{N_{part}}$	97
4.6.2.5	Final error on the ratio	98
4.6.2.6	Final error on the ratio for 200/62.4 GeV	99
5	RESULTS FROM MID-RAPIDITY CHARGED PARTICLE MULTIPLICITY MEASUREMENTS	100
5.1	Results for individual energy measurements, 0-50% most central data	100
5.1.1	Centrality dependence for 200 GeV	101
5.1.2	Centrality dependence for 19.6 GeV	103
5.1.3	Centrality dependence for 62.4 GeV	104
5.2	Results for ratio measurements, 0-50% most central data . . .	105
5.2.1	Ratio 200/19.6 GeV	105
5.2.2	Ratio 200/62.4 GeV	108
5.3	Energy density	109
6	COMMENTARY ON THE RESULTS	114
6.1	Energy density versus collision energy	114
6.2	Comparison of Au+Au and p+p charged particle multiplicities	116
6.3	Comparison with lower energy A+A	119
6.4	Comparison with theoretical models	120
6.5	Scaling properties	125
6.6	Discussion on centrality	127
7	CONCLUSION	129
	APPENDICES	131
	Appendix A	132
	Appendix B	133
	Appendix C	142
	Appendix D	151
	Appendix E	164
	Appendix F	175
	CITED LITERATURE	187
	VITA	192

LIST OF TABLES

<u>TABLE</u>		<u>PAGE</u>
I	DATA TRIGGERS FOR DIFFERENT YEARS	37
II	VERTEX RESOLUTIONS	44
III	YEARLY COUNT ON NON-WORKING CHANNELS	74
IV	CONTRIBUTION OF K_S^0 (WEAK) DECAY PRODUCTS TO TRACK- LET RESULTS	77
V	SYSTEMATIC ERROR ON THE RATIO OF TRACKLET RESULTS	99
VI	RESULTS FOR THE PSEUDORAPIDITY DENSITY AT 200 GEV	102
VII	RESULTS FOR THE PSEUDORAPIDITY DENSITY AT 19.6 GEV	104
VIII	RESULTS FOR THE PSEUDORAPIDITY DENSITY AT 62.4 GEV	106
IX	RESULTS FOR ENERGY DENSITY	113
X	BEAM ENERGIES FOR AU+AU COLLISIONS	136
XI	VALUES FROM DIFFERENT CORRECTION FACTORS	156
XII	TRIGGER EFFICIENCIES	180
XIII	EXAMPLE OF THE FINAL SYSTEMATIC ERRORS ON $\langle N_{PART} \rangle$ FOR D+AU	186

LIST OF FIGURES

<u>FIGURE</u>		<u>PAGE</u>
1	The RHIC complex	2
2	A single heavy ion event	4
3	Running of the QCD coupling constant, α_s	6
4	Current understanding of the QCD phase diagram	8
5	Results from lattice QCD calculations	9
6	Time evolution of a nucleus-nucleus collision	13
7	Participants and spectators	14
8	Schematic illustration of a collision	15
9	Glauber model for N_{part} and N_{coll}	16
10	Woods-Saxon distribution for the gold nucleus	17
11	Setting the saturation scale	24
12	The PHOBOS detector setup for the 2001-2002 Au+Au run.	30
13	Paddle counters	32
14	Paddle time difference and triggers for 200 GeV	36
15	Trigger Inspector Paddle tracking	38
16	Trigger Inspector L1 tracking	39
17	Three-dimensional view of the Vertex detector	40
18	Energy MIP in the Inner Top Vertex	41
19	Non-working channels for one Vertex detector sensor	43

LIST OF FIGURES (Continued)

<u>FIGURE</u>		<u>PAGE</u>
20	Vertex resolution and efficiency for 62.4 GeV versus centrality	46
21	Paddle time difference and event selection for 200 GeV	48
22	Event selection and ZDC time restrictions	49
23	ZDC time signals versus run for 200 GeV from the Inspector	50
24	ZDC and event selection for 19.6 and 62.4 GeV	51
25	Paddle time difference and event selection for 19.6 GeV	53
26	Paddle time restrictions and event selection for 19.6 GeV	54
27	Pile-up and event selection for 62.4 GeV	55
28	Trigger efficiency determination	56
29	Centrality determination with Paddles	57
30	Schematic depiction of a tracklet	61
31	Non-merged and merged hits in the Vertex detector	62
32	Outer Vertex hits versus Paddle Mean	65
33	Outer Vertex hits versus OHB	66
34	Tracklet residuals in η	67
35	β versus Outer Vertex hits	68
36	Maximum OHB versus energy	70
37	The α' correction factor for 200 GeV	71
38	The α' correction factor versus OHB for all energies	72
39	Geometrical acceptance of the Vertex detector	73
40	Fraction of background particles versus η	75

LIST OF FIGURES (Continued)

<u>FIGURE</u>		<u>PAGE</u>
41	Number of K_s^0 decays per HIJING event	76
42	Truth and reconstructed tracklets in MC, 200 GeV	78
43	Effect of vertex resolution on Vertex hits and residuals	80
44	Effect on tracklet residuals from the vertex resolution	81
45	The α correction factor	82
46	Correction factors with geometrical acceptance accounted for	83
47	Pseudorapidity regions used to derive the centrality for 200 and 19.6 GeV data	84
48	Effect on multiplicity from the uncertainty in the trigger efficiency	91
49	Final error on the ratio of tracklet results	98
50	Results for charged particle multiplicity for 200 GeV Au+Au	101
51	Results for charged particle multiplicity for 19.6 GeV Au+Au	103
52	Results for charged particle multiplicity for 62.4 GeV Au+Au	105
53	Ratio of the multiplicity versus centrality for 200/19.6 GeV	107
54	Ratio of the multiplicity versus centrality for 200/62.4 GeV	108
55	Energy density estimated for 200 GeV	110
56	Energy density estimated for 19.6 GeV	111
57	Energy density estimated for 62.4 GeV	112
58	Estimated energy density as a function of $\sqrt{s_{NN}}$	115
59	Charged particle multiplicity per participant pair as a function of center-of-mass energy	116
60	Comparison of final results with $p(\bar{p}) + p$ multiplicity.	117

LIST OF FIGURES (Continued)

<u>FIGURE</u>		<u>PAGE</u>
61	Final results scaled by the corresponding $p(\bar{p}) + p$ data	118
62	Multiplicity results for 200 GeV p+p, d+Au and Au+Au collisions . . .	120
63	Results compared to models	121
64	Ratio results for the 200/19.6 GeV data, with models	122
65	Results of ratios of 200 GeV to all energies	125
66	Total number of charged particles versus $\langle N_{part} \rangle$	126
67	Ratios of charged particle spectra at 200/62.4 GeV	127
68	Example diagrams of the Strong Interaction	134
69	HIJING calculation for $dN/d\eta$ versus η and dN/dy versus y	137
70	Deep inelastic scattering in QCD	138
71	Beam and target interaction	140
72	The RHIC complex	143
73	The BRAHMS detector at RHIC	145
74	The PHENIX detector at RHIC	146
75	The STAR detector at RHIC	147
76	The PHOBOS detector at RHIC	148
77	PHOBOS detector at RHIC, view closest to the IP	149
78	Reconstruction at 200 GeV, effect of the efficiency correction factor . .	152
79	Reconstruction at 200 GeV, effect of background and geometry	153
80	Reconstruction at 62.4 GeV, effect from using different subdetector . .	154
81	Reconstruction at 62.4 GeV, effect from using different vertex range . .	154

LIST OF FIGURES (Continued)

<u>FIGURE</u>		<u>PAGE</u>
82	Reconstruction at 62.4 GeV, effect from using different pass method . .	155
83	Reconstruction at 62.4 GeV, effect from using different tracklet residual cut	155
84	Reconstruction at 62.4 GeV, effect from using different energy cut . . .	156
85	Charged particle multiplicity per participant pair as a function of $\langle N_{part} \rangle$ for $\sqrt{s_{NN}} = 200, 130$ and 19.6 GeV compared to other experiments at RHIC	157
86	Charged particle multiplicity per participant pair as a function of $\langle N_{part} \rangle$ for $\sqrt{s_{NN}} = 19.6$ GeV compared to other experiments	158
87	Extrapolating the p+p inelastic result for 19.6 GeV	159
88	Calculating the effective collision area of a Au+Au collision	163
89	Pedestal and MIP position from a Paddle counter	165
90	Detector timing diagram	166
91	TDC and ADC fractions for a Paddle counter	167
92	Paddle time difference monitored from the Inspector	168
93	Paddle time for the Positive side monitored from the Inspector	169
94	Beam orbits monitored from the Inspector	171
95	z -vertex range selected by the TAC monitored from the Inspector . . .	172
96	The fraction of good events written to tape, monitored by the Inspector	173
97	Estimate for the total number of events for PR04 Au+Au from the Inspector	174
98	N_{part} and EOct correlation in d+Au	176
99	Steps for centrality determination in d+Au	177

LIST OF FIGURES (Continued)

<u>FIGURE</u>		<u>PAGE</u>
100	The average N_{part} values and widths for percentile cross-section bins in d+Au	178
101	Paddle and T0 trigger efficiency in d+Au	179
102	Trigger and Vertex bias effect on MC	180
103	Effect of smearing on the $\langle N_{part} \rangle$ values	181
104	$\langle N_{part} \rangle$ values determined from different definitions of the deuteron nuclear density profile	182
105	Glauber studies	185

LIST OF ABBREVIATIONS

AA	Nucleus-nucleus collision
ADC	Amplitude to Digital Converter
AGS	Alternating Gradient Synchrotron
Au+Au	Gold-gold collision
BEVALAC	A high energy synchrotron accelerator at Lawrence Berkeley Laboratory
BNL	Brookhaven National Laboratory
CERN	Conseil Europeen pour la Recherche Nucleaire (Eu- ropean Laboratory for Particle Physics)
d+Au	Deuteron-gold collision
DAQ	Data Acquisition
EOct	Energy liberated in the Octagon detector
IP	Interaction Point
L0	Level zero trigger
L1	Level one trigger
LHC	Large Hadron Collider
MC	Monte Carlo

LIST OF ABBREVIATIONS (Continued)

MIP	Minimum Ionizing Peak
NIM	Nuclear Instrumentation Module
NN	Nucleon-nucleon collision
N_{part}	Number of participants
N_{coll}	Number of collisions
PID	Particle Identification
PMT	Photo Multiplier Tube
PMC	PHOBOS Monte Carlo
PN	Paddle Negative counters
p+p	Proton-proton collisions
PP	Paddle Positive counters
pQCD	perturbative Quantum Chromodynamics
QCD	Quantum Chromodynamics
QGP	Quark Gluon Plasma
RHIC	Relativistic Heavy Ion Collider
SPS	Super Proton Synchrotron
TAC	Time to Amplitude Converter
TDC	Time to Digital Converter

LIST OF ABBREVIATIONS (Continued)

T0	Time Zero counters
TOF	Time of Flight
UIC	University of Illinois at Chicago
ZDC	Zero Degree Calorimeter

SUMMARY

Charged particle multiplicity is a global observable, measuring the number of particles produced in a single nucleus-nucleus collision. The data for the analysis is collected at the Relativistic Heavy Ion Collider at Brookhaven National Laboratory with the PHOBOS detector. Collisions of gold nuclei, accelerated to three different center of mass energies of $\sqrt{s_{NN}} = 19.6$, 62.4 and 200 GeV, are analyzed.

The Thesis begins with an overview of theoretical models and expectations for the measured charged particle multiplicity. The next chapter describes the initial analysis, introducing the detectors and setup used for the data collection. Event selection and the centrality determination are discussed only to the details relevant to this analysis. Centrality determination plays a major role in interpreting the charged particle multiplicity.

The *Vertex tracklets* method is used to measure the produced charged particle multiplicity at mid-rapidity. The name is taken from the Vertex detector which is used in the analysis. A description of the method is provided, along with some modifications and additional checks performed in order to obtain the results for the $\sqrt{s_{NN}} = 19.6$, 62.4 and 200 GeV collisions for the top 50% of the inelastic cross-section. Expansion of the analysis to provide high precision results on the ratio of two data sets is also discussed. The steps to extend the analysis in the future to a lower centrality are described.

Results are presented in two parts. In the first part, results for the individual measurements for the top 50% of the cross-section are shown for various centrality determinations. Estimation

SUMMARY (Continued)

of the energy density produced during the collisions is made using these results. In the second part, the ratio of these data are shown with respect to the 200 GeV dataset. The results as a function of collision centrality are compared with theoretical calculations in order to differentiate between competing models of particle production.

CHAPTER 1

INTRODUCTION

1.1 Concepts

Quarks and gluons are the building blocks of matter, as it is currently known to us. Everything surrounding us on Earth is made from these objects. The theory which describes how the partons, quarks and gluons, interact and bind to form the matter (nucleons, nuclei and hadrons) in nature is Quantum Chromodynamics. This theory has been proven in strength through many experiments. From its underlying symmetries many new concepts arise, such as the confinement of the quarks and gluons into hadrons in ordinary (cold) matter.

It is conjectured that subjecting “cold” matter to extreme conditions, such as high temperatures or high densities, can produce a deconfined state of free quarks and gluons, known as the Quark Gluon Plasma (QGP). Such conditions are believed to exist in neutron stars and at the early stage of the Universe. It is hoped that the hot and dense conditions for a QGP can be created from the collision of two heavy nuclei at high incident energies.

1.2 Background

For over three decades the search for the QGP has been ongoing. The energy to which the nuclei are accelerated and collided has constantly increased, making the initial state created hotter and denser. The Relativistic Heavy Ion Collider (RHIC) at Brookhaven National Laboratory is the largest (highest beam energy) accelerator for heavy ion collisions. Nuclei

are collided up to the highest center of mass energy of $\sqrt{s_{NN}} = 200$ GeV per nucleon. Four experiments, BRAHMS, PHENIX, PHOBOS and STAR, have been built with the goal to first observe and later study the new state of matter created during these collisions.

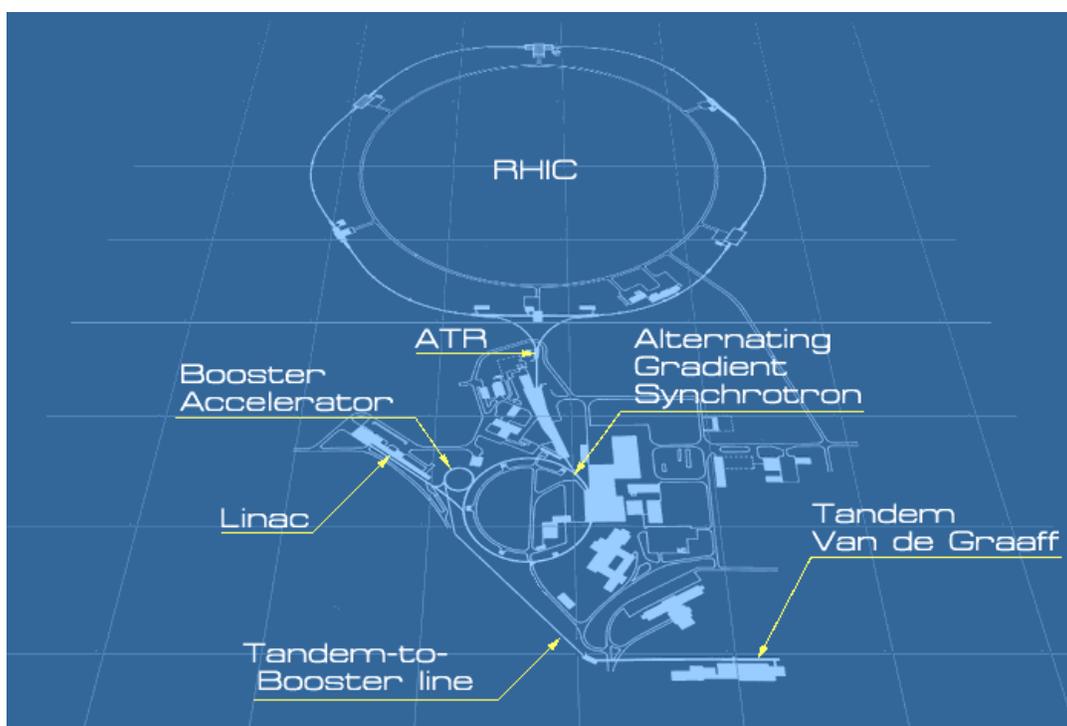


Figure 1. The RHIC complex.

In a heavy ion collision, the *Energy density* created is believed to be an essential factor when forming the QGP; a critical amount of energy per unit volume must be surpassed to reach this point. The first estimated value for this energy density was reported by the PHENIX

collaboration (1) and was calculated to approach $5 \text{ GeV}/\text{fm}^3$. This value far exceeds both the cold nucleon density ($\sim 500 \text{ MeV}/\text{fm}^3$) and the density of a gold nucleus ($\sim 150 \text{ MeV}/\text{fm}^3$). One can surmise that the system created is very different from the initial hadronic states existing immediately before the collision. In fact, all results presented in this Thesis are from collisions where the energy density is believed to be greater than $1 \text{ GeV}/\text{fm}^3$. This is the energy density predicted using lattice calculations (2) to be the critical energy density required for a transition from a hadron-gas phase into a QGP.

Despite these estimates of the energy density scientists from all RHIC experiments have been careful in declaring the discovery of the QGP. As can be seen from the overview of their programs (3; 4; 5; 6) there is no definitive statement.

Many models attempt to describe the different aspects of particle production in collisions involving heavy nuclei. Most of them rely on QCD. However, with the many input parameters in the models, it is difficult to calculate quantities experiments measure.

1.3 Goals

The search for the QGP starts with measuring the energy density. Immediately after relativistically-contracted nuclei collide, the maximum energy density is reached. Within an experimental environment a measurement of this is not possible. The energy density of the equilibrated system can be estimated from the charged particle multiplicity in the central rapidity region using Bjorken's estimate (8). This is the region bounded by the point where the particles are produced with comparable longitudinal and transverse momenta, known as

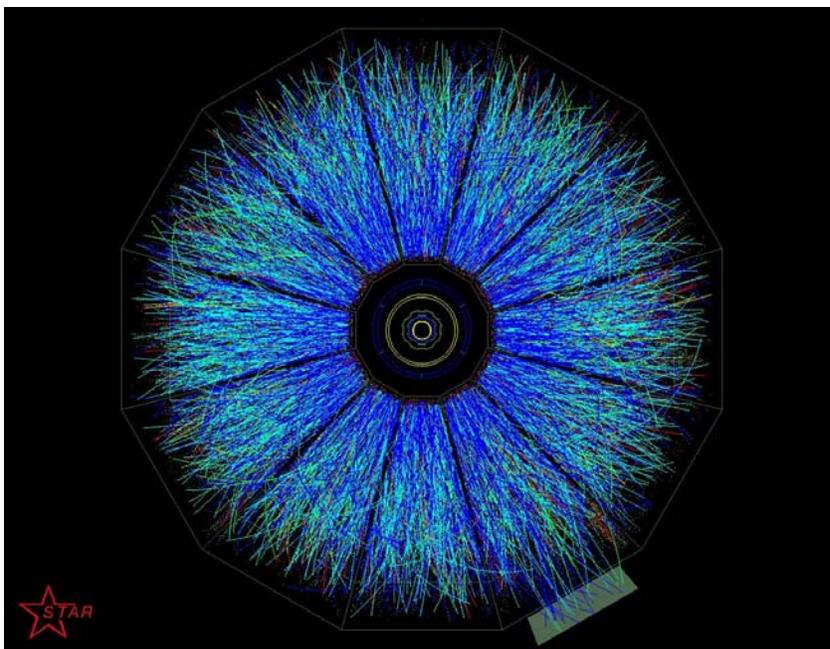


Figure 2. A heavy ion event as seen in the STAR detector. Figure is from (7).

mid-rapidity ($|\eta| < 1$). As can be seen from Figure 2, several thousand charged particles are created in a heavy ion collision at these energies.

This Thesis presents an experimental technique used in PHOBOS to measure the charged particle multiplicity at mid-rapidity. The results of such measurements are presented for three different center of mass energies. The study of the evolution of this multiplicity with energy and geometry of the collision has been used to differentiate between various proposed mechanisms of particle production (9). Initial theoretical expectations for charged particle multiplicities at RHIC varied by a factor of two, see (10) for a summary. Experimental measurements were much smaller than the majority of the predictions, resulting in the rejecting of most models.

CHAPTER 2

THEORY AND MODEL EXPECTATIONS

2.1 The search for a new state of matter

After predicting the existence of a new state of matter, for the last 30 years the collective efforts of theorists and experimentalists have been combined in order to connect the theory of the strong interaction with the experimental observations.

2.1.1 Quantum Chromo-Dynamics, QCD

QCD describes the strong interaction between constituent partons of hadronic matter (i.e. the quarks and gluons)¹. This is done by introducing a new *color* quantum number.

Quarks are spin- $\frac{1}{2}$ fermions, with fractional electric charge and come in six flavors: up, down, strange, charm, top and bottom. The quarks can exist in one of three color states: red, green or blue. Quarks are “glued” together by eight additional partons, gluons, which are massless spin-1 bosons. Gluons are color-anticolor states (e.g. a *red- $\overline{\text{blue}}$* state). All particles, observed in nature, are made up of either three quarks (qqq or $\overline{q}\overline{q}\overline{q}$) or a quark-antiquark pairs ($q\overline{q}$). As a result, all hadrons are found to have an integer electric charge and are colorless objects. As colored objects cannot exist in nature, the quarks and gluons are confined within hadrons. It is very important to note that gluons not only mediate the strong interaction between the quarks,

¹For a detailed description of the theory see for example (11), some basic concepts are presented in Appendix B.

but they can interact among themselves. This interaction is described by the QCD Lagrangian and is characterized by the strong coupling constant, α_s .

Because of gluon self-interaction, at short distances (high momentum transfer in the interaction) the color charges are anti-screened¹ via gluon radiation. The resulting effect is that the strong coupling constant, α_s , decreases in magnitude. This is known as the “*asymptotic freedom*” of quarks and gluons and leads to a deconfined state. α_s is calculated to have a momentum scale dependence, which has been confirmed experimentally, see Figure 3.

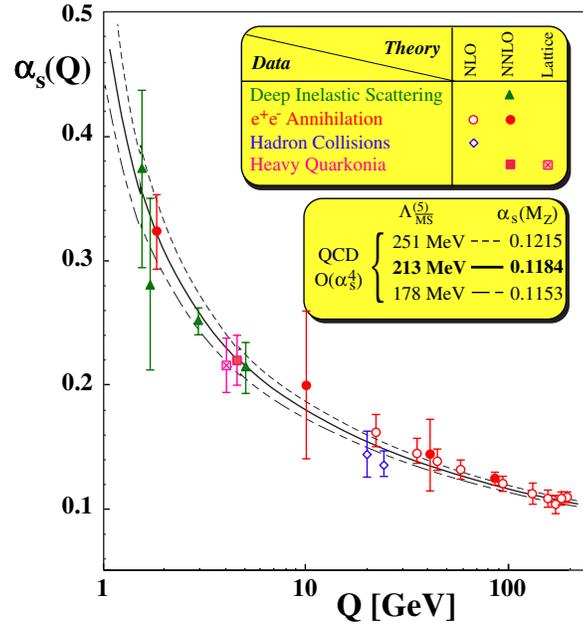


Figure 3. Experimental observation of the momentum dependence of the strong coupling constant, α_s . The figure is from (12).

¹the strength of the color field is diffused

To the leading order, the coupling constant is found to be inversely proportional to the momentum transfer squared in the interaction, $\alpha_s(Q^2) \approx \left(\log(Q^2/\Lambda_{QCD}^2)\right)^{-1}$. Λ_{QCD} is the momentum cut-off scale¹ in the theory. A small value of α_s ($Q^2 \gg \Lambda_{QCD}^2$) translates to weaker interactions, leading to calculable physical properties at short distances. This is the regime where perturbative calculations on QCD can be applied. Large α_s values (small momentum transfer or a momentum comparable to Λ_{QCD}), results in confinement of quarks and gluons in hadrons.

2.1.2 QGP

When the temperature, or density, in hadronic matter increases, the average distance between the partons becomes small and the interactions of quarks and gluons will weaken. This process can free the quarks and gluons from their confinement, forming a new state of matter, the *Quark Gluon Plasma*.

The current theoretical understanding of QCD is usually represented by a qualitative sketch of the QCD phase diagram, Figure 4. Phase boundaries (black lines) separate the phases of strongly-interacting matter: quark matter and hadronic matter. Any region on the diagram is in thermal and chemical equilibrium, characterized by some values of temperature, T and baryon chemical-potential, μ_B . There are two regions of interest that can explore the QCD phase diagram. First, the region of low T and high μ_B , found inside neutron stars. The region of the diagram characterized by a large temperature and small to medium values of μ_B is

¹This is needed to avoid an infra-red divergence when summing over all possible diagrams

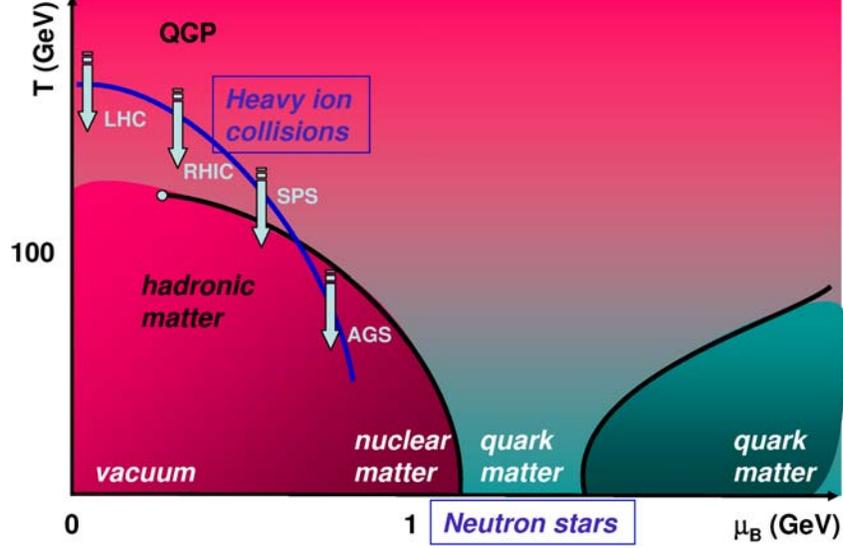


Figure 4. Current understanding of the QCD phase diagram. Phase boundaries are shown with black lines. Heavy ion collisions (represented by the blue arrows) probe the region with large T and $\mu_B < 1$ GeV, with highest energies closest to $\mu_B = 0$. The region of small T and large μ_B can be observed in neutron stars. See text for more details.

associated with the hot and dense matter created in a heavy ion collisions. The blue arrows represent estimates of T and μ_B (13), with higher energy collisions being at lower μ_B .

The properties of the created system in heavy ion collisions can be described by an equation of state $\epsilon(T, \mu_B)$. Currently there is no analytical method, which starts from the QCD Lagrangian and calculates the equation of state for the region of interest. Lattice QCD is the only technique able to calculate the relevant quantities from first principles. This method uses numerical calculations. The results give an understanding of the critical behavior of interacting

partonic matter only for zero baryon chemical potential¹, and obtain the equation of state as a function of temperature. Figure 5 illustrates that the equation of state for a non-interacting gas of quarks and gluons ($\epsilon_{SB}(T, \mu)$, arrows on left hand side) and that of a pion gas (ϵ_π , not shown), are found to give different results when compared to computations from lattice QCD (curves), indicating that interactions among partons exist in the quark matter.

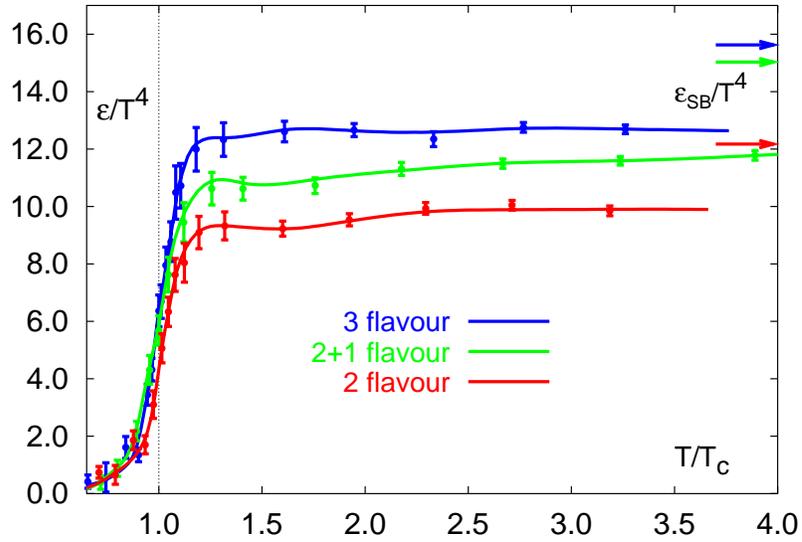


Figure 5. The energy density as a function of temperature from lattice QCD calculations. The arrows represent the case of a non-interacting gas of quarks and gluons. This figure is from (2).

¹The regime of $\mu_B = 0$ is preferable for the lattice simulations.

Lattice calculations currently predict an abrupt change in energy density going from a hadronic to a QGP regime (Figure 5). This could be a possible signal of a phase transition. The type of the transition between these two phases is not clear. Calculations assuming either a 2 or 3 light-quark flavor system predict a critical temperature, T_c , which varies between 150 and 200 MeV with the critical energy density $\epsilon_c \approx 1 - 3 \text{ GeV/fm}^3$ ¹.

The phase diagram has been subject to ongoing research. Reference (14) provides an extensive review of the recent progress in understanding the QCD phase diagram focusing on the types of phase transitions and phenomena close to the critical end point.

To summarize, the important properties of the QGP at very high T are²:

1. A large energy density,
2. A state of free quarks and gluons (no hadrons),
3. A phase transition at a critical temperature, T_c .

2.1.3 Ultra-relativistic heavy ion collisions and the QGP

High energy collisions of heavy ions can be used to probe the region of high density and temperature. The center-of-mass energy of the collisions, starting from LBL-BEVALAC ($\sqrt{s_{NN}} \approx 2 \text{ GeV}$) through BNL-AGS ($\sqrt{s_{NN}} \approx 4 \text{ GeV}$) and CERN-SPS ($\sqrt{s_{NN}} \approx 18 \text{ GeV}$) has constantly increased. $\sqrt{s_{NN}} \approx 5.5 \text{ TeV}$ will be reached in future at the planned CERN-LHC (closest to $\mu_B = 0$).

¹Predicted lattice critical temperature is $T_c \approx 170 \text{ MeV}$ and $\epsilon \approx 0.7 \text{ GeV/fm}^3$ (2)

²not discussed here, Chiral symmetry restoration (15)

Relativistic heavy ion collisions at RHIC are carried out at a maximum energy of $\sqrt{s_{NN}} = 200$ GeV, an order of magnitude higher than those at the fixed-target program of the CERN-SPS. With the increase of collision energy, the studied region is shifted to a higher temperature, but lower value of baryon chemical potential. This regime is preferred by the lattice simulations ($\mu_B \approx 0$). On the other hand, probing different parts of the phase diagram could lead to locating the critical point and the type of phase transition, see (14).

The energy density created in collisions at the highest RHIC energy was expected to be well above the critical density required for a deconfined state, predicted by lattice QCD, and well above the density of cold nuclear matter. The initial energy density of the produced medium at the time of thermalization τ_0 is given by the Bjorken estimation (8) in Equation 2.1.

$$\epsilon_{bj} = \left(\frac{dN^{y=0}}{dy} \right) \frac{w_h}{\tau_0 \pi R_A^2} \quad (2.1)$$

where $\frac{dN^{y=0}}{dy}$ is the number of particles (charged and neutral) created at mid-rapidity with average energy w_h . The effective interaction volume of the thermal medium is estimated by using the nuclear cross-section, πR_A^2 in the transverse plane and the formation time, τ_0 , along the beam axis.

Over the last four years, the RHIC machine has made it possible to study the hot and dense matter created in the most violent head on collisions. The primary objective of the experiments is to verify the existence of the QGP. Once this is accomplished, the task of understanding the properties of the QGP will begin in earnest.

2.2 Description of heavy ion collisions

A broad description of heavy ion collisions is presented in this Section. The expected time evolution, modeled geometrical parameters and the interplay between “hard” and “soft” collisions are discussed.

2.2.1 Time-evolution of a nuclear-nuclear collision

Figure 6 presents the current understanding of the time evolution of the nuclear-nuclear collision¹.

1. Pre-equilibrium

Two nuclei collide; the created matter is not thermally equilibrated.

2. Quark Gluon Plasma

Thermal equilibrium is assumed to be reached after a short time ($\tau_0 \approx 1fm$). If the created energy density is large enough, a deconfined state of quarks and gluons is created. Properties of this state can be directly probed by studying the p_T spectra of dilepton pairs and direct photons.

3. Hadronic matter

After rapid expansion and cooling, the partonic degrees of freedom convert into hadrons; this is known as the “hadronization” phase. This expansion can be studied by measuring the elliptic flow (v_2) versus p_T . Chemical freeze-out is complete when all inelastic collisions between the hadrons subside, fixing the chemical composition of the final system,

¹Bjorken presented the first time-evolution of a relativistic heavy ion collision in (8)

evident in the particle ratios. As suggested by (16), final hadronic interactions can be substituted by a non-interacting system of gas resonances leading to a description of relative abundances of all hadron species (particle ratios) by just two parameters T and μ_B .

4. Free hadrons

Kinetic freeze-out is the point where all elastic interactions between hadrons cease. The radii inferred from two-particle pion interferometry can estimate the size and the emission time of the source at this stage (17). At this point, the particle spectra are fixed.

These four stages comprise the description of the nucleus-nucleus collision. After completion, all particles are then measured in the detectors.

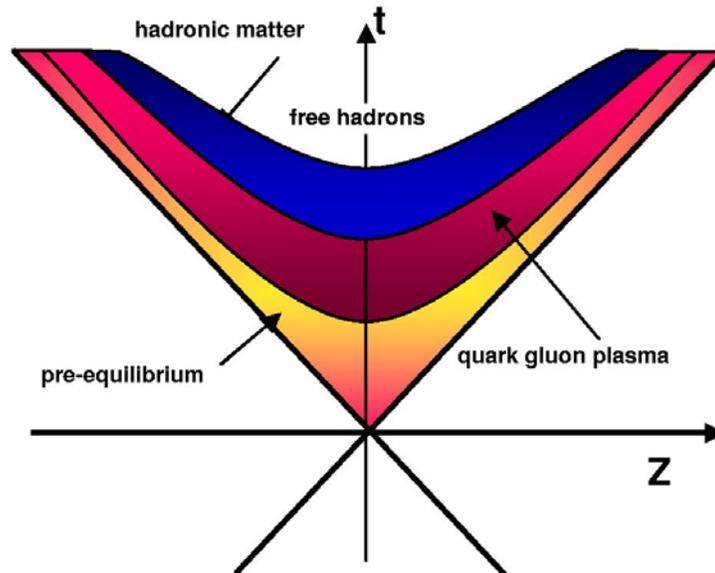


Figure 6. Time evolution of a nucleus-nucleus collision.

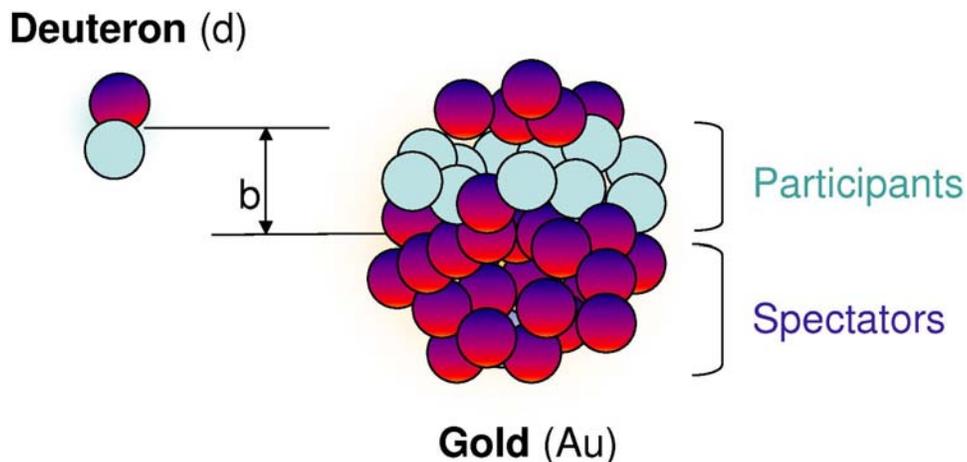


Figure 7. A representation of a d+Au collision, shown as not Lorentz-contracted for clarity. Nucleons participating in the collision, N_{part} , are shown in blue. The spectator nucleons are shown in red. b is the impact parameter.

2.2.2 Description of the collision geometry

A sketch of a d+Au collision is shown in Figure 7, illustrating the possible collision path of one nucleon from a deuteron as it traverses a gold nucleus. “Centrality” provides a description of the geometrical characteristics of a nucleus-nucleus collision, see Figure 8. Centrality is a very important variable in heavy ion physics and is used for direct comparison of results between experiments and theoretical predictions. Centrality is an estimate of the number of nucleons, N_{part} , which participate in the collision. When the impact parameter, b , is small, the nuclei will collide almost head-on and the collision will be termed “central”. For impact parameters that are close to the sum of radii of the nuclei, few nucleons participate and this event is classed as “peripheral”.

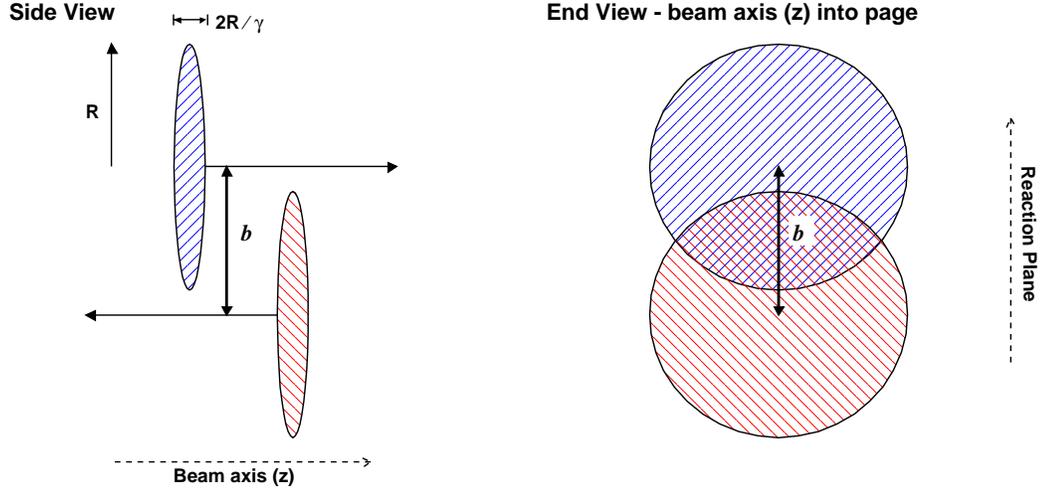


Figure 8. Heavy ion collision parameters. R is the radius of the nucleus, b impact parameter, γ is the Lorentz factor.

The geometrical overlap of the nuclei can also be described by the number of binary (p+p-like) collisions, N_{coll} . It is impossible to measure any of these quantities directly; they have to be deduced by comparison of a measured quantities (e.g. multiplicity) with MC model predictions.

MC generators use a *Glauber Model* (19) to estimate N_{part} and N_{coll} . The model is a simple nucleus-nucleus scattering model in which all individual nucleon-nucleon interactions are considered to be independent $p + p$ -like collisions. Input to the model is the collision nucleon-nucleon cross-section at the corresponding $\sqrt{s_{NN}}$ energy. Several assumptions are made in this model, such as that nucleons travel in straight lines, the nucleon-nucleon cross-section does not change after a collision and that nucleons within the nucleus distribution can be described by

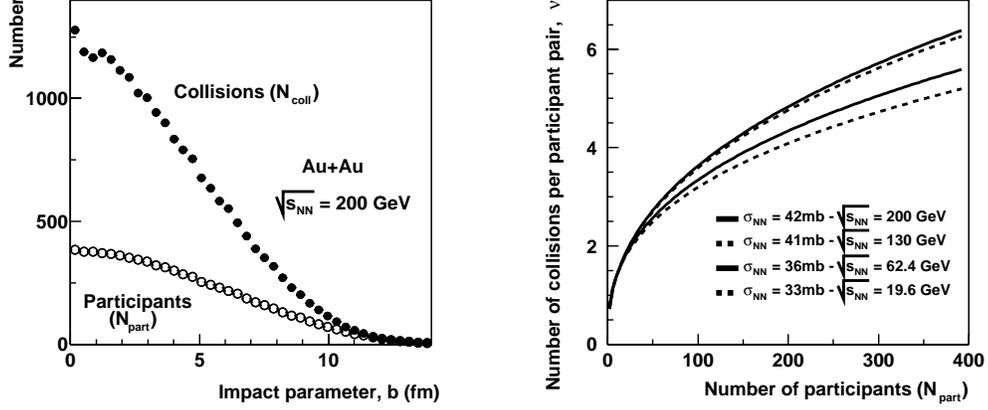


Figure 9. Glauber model calculations for N_{part} and N_{coll} . The left panel shows N_{part} and N_{coll} for different impact parameters. The right panel shows the evolution of the number of collisions per participant pair (ν) with N_{part} for different RHIC energies. The dependence can be parameterized as $N_{coll} \sim N_{part}^{4/3}$. The inelastic cross-sections for p+p collisions (σ_{NN}) are interpolated from (18).

the density profile shown in Figure 10 for the gold nucleus. This *Woods-Saxon* function has two parameters, obtained from experimental fits to data (20; 21). Most of the matter can be found within radius R which drops sharply after distance a , known as the nucleus skin.

2.2.3 Soft and hard interactions

According to QCD, the momentum scale is important, resulting in the way we can describe the collisions. Depending on the momentum transferred in the collision, the parton-parton interactions (hence nucleon-nucleon and nucleus-nucleus interactions) can be broadly split into two groups: “soft” and “hard”.

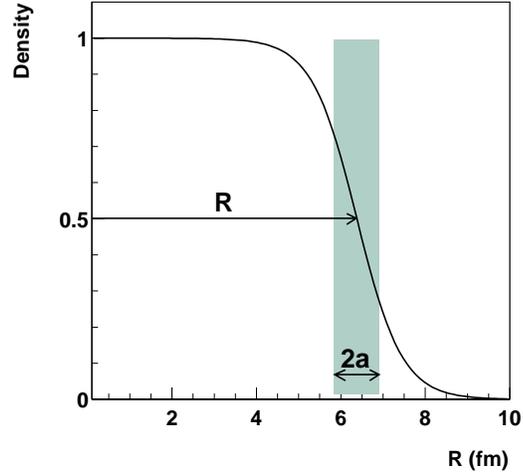


Figure 10. Woods-Saxon nucleon density distribution for the gold nucleus. The radius of the nucleus is $R = 6.38$ fm with skin width $a = 0.535$ fm.

2.2.3.1 Nucleon-nucleon collisions (NN)

Soft nucleon-nucleon collisions are those in which the momentum transferred between the nucleons is small ($\ll 1$ GeV). This collision type probes the whole hadron (large scale effects) and typically has large cross-sections which grow slowly (logarithmically) with center-of-mass energy. See (18) for the total $p + p$ cross-section.

Soft collisions are usually treated phenomenologically in models. One of the very successful non-QCD theories to calculate $p + p$ cross-sections is Regge theory (22). UA5 collaboration (23) and others have found a reasonable parameterization of the multiplicity produced with this type

of collision (p+p inelastic) with center-of-mass energy. The predominant feature is a logarithmic growth with \sqrt{s} .

Hard collisions are collisions with a large momentum transfer (> 10 GeV). They are typically connected with experimentally observed high- p_T jets (and heavy quark and lepton pair production). These collisions probe the structure of the hadron, have relatively small cross-sections which depend strongly on the collision energy.

High- p_T jets are experimentally observed as hadronic clusters, their transverse energy is measured by calorimeters with $E_T > 5$ GeV. They can be modeled using a straight forward pQCD calculation. Hard partonic scattering is theoretically expected to produce jets with lower E_T , however these are difficult to separate from the background. These *minijets* can also be calculated by pQCD and some models predict that they will play a major role in relativistic heavy ion collisions.

It is difficult to separate jets produced from gluons or quarks experimentally and resolve which type of partons participated in the hadron-hadron collision. The QCD calculations usually calculate the inclusive cross-section for jet production in hadronic collisions, summing over all possible partons in the hadrons. These processes are described by pQCD-inspired models (24).

2.2.3.2 Nucleus-nucleus collisions (AA)

The collisions between two heavy nuclei are more complex. Extrapolating from nucleon-nucleon to nucleus-nucleus collisions is not trivial. The nucleus-nucleus collisions are not merely a sum of $p + p$ collisions. In such interactions, the collision energy at RHIC is expected to

be sufficient to create a *medium* with more than just hadronic degrees of freedom. In this framework, it becomes necessary to move from a regime of a nucleonic description of the collision to a partonic one.

It is not known how exactly a parton-parton collision would evolve into hadrons (the hadronization stage) and how the soft-hard production relation is manifesting itself in the more complex nucleus-nucleus systems. Further uncertainties are introduced when the initially produced partons propagate into the medium, known as medium effects (for example jet quenching). This leads to substantial uncertainties in the particle production models, which in most cases rely on input parameters tuned to data measurements or scale parameters (e.g. momentum, energy).

The models, which try to describe the nucleus-nucleus collisions, use four different approaches:

1. Pure pQCD parton models (25)
2. String+pQCD models - HIJING (26)
3. Classical Yang-Mills - McLerran, Venugopalan (QM02) (27)
4. Phenomenological models(e.g.Initial state gluon saturation).

Reviews of models for particle production in heavy ion collisions can be found in (28) and see for example (29) talks.

2.3 Models for particle production in heavy ion collisions

Only the relevant models to the Thesis will be reviewed here. The regime of small coupling constant, which characterizes the relativistic heavy ion collisions, poses difficulties when trying to calculate quantities from the first principles of QCD. For most models, data from $p + p$ collisions are used as input.

2.3.1 Two component picture

One can consider that the multiplicity measured in p+p collisions at some energy, \sqrt{s} , can be factorized into two components. One component of the multiplicity is associated with hard processes (a fraction X of the total) and the other from soft processes ($1 - X$). In a similar manner, the multiplicity in nucleus-nucleus collisions could be considered to consist of hard processes, assumed to be incoherent and scale with the number of collisions (N_{coll}) and soft processes, assumed to scale with the number of participants (N_{part}). This reasoning leads to a two-component parametrization (30), of the charged particle multiplicity in nucleus-nucleus collisions, Equation 2.2.

$$\frac{dN_{ch}^{AA}}{d\eta} = \frac{dN_{ch}^{pp}}{d\eta} \left((1 - X(s)) \frac{N_{part}}{2} + X(s) N_{coll} \right) \quad (2.2)$$

where $\frac{dN_{ch}^{pp}}{d\eta}$ is the multiplicity measured for $|\eta| < 1$ in $p(\bar{p}) + p$ collisions.

The limits of this picture are pure hard or purely soft interactions. A model based on the limit of incoherent superposition of independent nucleon-nucleon collisions¹ ($X \rightarrow 1$) would

¹given by a Glauber model calculation

predict a multiplicity equal to number of collisions times the multiplicity for nucleon-nucleon collisions, see Figure 9 right panel. As such, the multiplicity would far exceed that in p+p collisions.

In the purely soft interaction limit ($X \rightarrow 0$), independent p+p collisions of only *wounded nucleons* contribute to the final multiplicity. The predicted multiplicity is simply the product of the number of participants and the multiplicity measured in p+p collisions. Wounded nucleons can further interact, but are assumed not to produce additional particles. This model is known as the “wounded” nucleon model (31).

The two following models use these concepts as their basis.

2.3.2 HIJING

HIJING, **H**eamy **I**on **J**et **I**Nteraction **G**enerator (26), uses the properties of $p+p$ collisions to extrapolate to nucleus-nucleus collisions. This two component model combines soft collisions and minijets, which arise from hard parton interactions.

The momentum cut-off, which separates the soft from hard collisions is an important input parameter. It is deduced from $p(\bar{p})+p$ data and set to be 2 GeV/c. Below this value the Lund string model (32; 33) is used to describe (soft) hadron production due to beam jet fragmentation. Above 2 GeV/c, pQCD is used to compute the minijet and high- p_T jet contribution. The other input parameter is the soft interaction cross-section ($\sigma_{soft} = 57$ mb). It is adjusted to fit

the measured inelastic nucleon-nucleon cross-section (σ_{in}^{NN}) in $p(\bar{p}) + p$ collisions at different energies¹.

The charged particle pseudorapidity density is described by two terms in Equation 2.3 (9): soft hadron production, proportional to N_{part} and minijet production, proportional to binary $p + p$ -like collisions, N_{coll} .

$$\frac{dN_{ch}^{AA}}{d\eta} = \langle n_{soft} \rangle \frac{\langle N_{part} \rangle}{2} + \langle n_{hard} \rangle \frac{\sigma_{jet}^{AA}}{\sigma_{in}^{NN}} \langle N_{coll} \rangle \quad (2.3)$$

$\sigma_{jet}^{AA}(s)$ is the average inclusive jet cross-section (per hadron-hadron collision) in the nucleus-nucleus collision. $\langle n_{soft} \rangle$ ($\langle n_{hard} \rangle$) represents multiplicity per unit of pseudorapidity from soft (hard) interactions.

Due to the σ_{jet}^{AA} dependence on energy, HIJING 1.35 (34)² predicts that the energy dependence of the Au+Au multiplicity is enhanced relative to p+p collisions. The centrality dependence of the multiplicity is expected to have the following features:

1. monotonic increase as a function of $\frac{N_{coll}}{N_{part}}$, see Equation 2.3,

¹where σ_{in}^{NN} comprises both the soft (σ_{soft}) and hard (σ_{jet}) cross-sections

²this version includes:

1. nuclear gluon shadowing, assumed to be identical to observed quark shadowing
2. jet quenching, modeled by a gluon splitting scheme with large p_T quarks having an energy loss of 1 GeV/fm.

This does not include final state rescattering, only the above schematic jet-quenching

2. The slope of the multiplicity per participant pair has to increase with collision energy since hadron multiplicity grows with energy as σ_{jet} ,
3. Very peripheral collisions have to agree with p+p (default input).

2.3.3 KLN Saturation model

The KLN Saturation model¹, as described in (35), is presented here. This is a phenomenological model using the concept of parton saturation to describe the relativistic heavy ion collisions in the weak coupling regime of high parton density.

Figure 11 presents an interaction of an external probe with a nuclear target of atomic number A . The momentum transfer in the interaction is denoted by Q , the Bjorken x stands for the part of the nucleon longitudinal momentum directly transferred to a parton. The probe, depending on the value of Q , can resolve a transverse area $\sim 1/Q^2$ ². For small values of x , the longitudinal distance (z) can exceed the nuclear diameter such that all partons in the transverse area interact coherently and the probe cannot resolve partons in this volume.

The critical value of the momentum transfer determines the *saturation scale* Q_s , Equation 2.4, above which the nucleus looks dense for the probe.

$$Q_s^2 \sim \alpha_s \frac{xG_a(x, Q_s^2)}{\pi R_A^2} \quad (2.4)$$

¹The Saturation model is described in (35), the connection to the two component picture was originally introduced in (30)

²From the uncertainty principle $\Delta p \Delta z \geq \frac{\hbar}{2}$

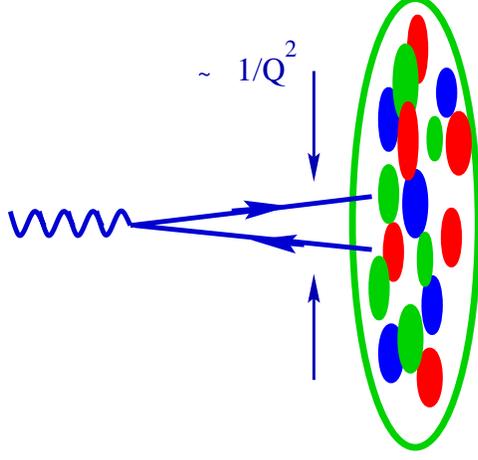


Figure 11. A hard probe interaction with a nuclear target; resolves the transverse area $\sim 1/Q^2$ (Q is the momentum transfer) and in the target rest frame the longitudinal distance $\sim \frac{1}{mx}$ (m is the nucleon mass and x Bjorken variable). This figure is from (35).

where $xG_a(x, Q_s^2)$ is the number of gluons, which becomes very large in the weak coupling regime, Equation 2.5.

$$xG_a \sim \frac{1}{\alpha_s(Q_s^2)} \sim \ln(Q_s^2/\Lambda_{QCD}^2) \quad (2.5)$$

As shown in (30), the multiplicity dependence on centrality around mid-rapidity is determined solely by the running coupling constant:

$$\frac{dN}{d\eta} = cN_{part}xG(x, Q_s^2) \quad (2.6)$$

The coefficient $c \approx 1.23$, known as gluon liberation, is determined from experimental measurements.

The two component parametrization is used as a connection between the data and the KLN model, Equation 2.2. In contrast to the perturbative expectations, where the hard component is proportional to the minijet cross-section and has to grow with centrality when \sqrt{s} increases, here X is related to the number of gluons and the increase of multiplicity with centrality comes only from the running coupling constant $\sim 1/\alpha_s$.

The energy dependence of the multiplicity arises from the dependence of the saturation scale on Bjorken x , $x = Q_s/\sqrt{s}$, and the relation of Q_s^2 to the gluon distribution functions (Equation 2.4). This dependence, Equation 2.7, is derived from HERA data on gluon distribution functions with saturation scale $Q_s^2 = 1 - 2 \text{ GeV}^2$ and parameter $\lambda \simeq 0.25 - 0.3$.

$$Q_s^2 \propto (\sqrt{s})^\lambda \quad (2.7)$$

The charged particle multiplicity is expected to grow logarithmically with center-of-mass energy (using Equation 2.6, Equation 2.5 and Equation 2.7).

$$\frac{dN}{d\eta} \sim \text{const} N_{part} \ln((\sqrt{s})^\lambda) \quad (2.8)$$

To summarize, the KLN Saturation model predicts a similar evolution of multiplicity with centrality for all center-of-mass energies. The energy dependence is expected to rise logarithmically with \sqrt{s} . If the lowest RHIC energy data confirms the Saturation model description, this could be a possible indication that the parton saturation scale sets in at energies lower than 19.6 GeV for heavy ion collisions.

2.4 The motivation for measuring multiplicity

The multiplicity of charged particles is a global observable, characterizing the entire heavy ion collision. The number of charged particles, produced in the central rapidity region, can be used to determine the energy density in the collision. This is the starting point in the search for the QGP.

The geometry of the collision is used to assess how the particle production in nucleus-nucleus collisions compares to that of simpler systems such as p+p and p+A. Scaling the charged particle multiplicity by the number of participating pairs is one way to directly compare the results from different collision systems and experiments. This also corrects for any effects in the measured multiplicity arising from the centrality determination.

The measured charged particle multiplicity is a result of the interplay between various physical processes at different stages of the collision. This could affect the number of degrees of freedom (entropy) available for particle production. Systematically varying the center-of-mass energy, the system size and the centrality of the collision is a way to separate these processes.

The centrality dependence, combined with other global measurements, can be used as a “key” observable to narrow the uncertainties of different theoretical models of particle production.

CHAPTER 3

INITIAL ANALYSIS: TRIGGERING, EVENT SELECTION AND CENTRALITY DETERMINATION

This Chapter describes the parts of the initial analysis used in this Thesis. First, the trigger detectors and setup used for the data collection are introduced. The detector design and construction was done before my joining the collaboration. This Chapter contains some general and important information about the main detectors used in the analysis. More information on the detectors can be found in (36).

The event selection used in the analysis is divided into two categories, first from the trigger and then by the selection of a reconstructed collision vertex. The latter part of this Chapter deals with the procedure of dividing the data into well defined bins of multiplicity, known as the centrality determination. Only the details pertinent to this analysis are discussed.

3.1 Nomenclature

This Section has some definitions used throughout the Thesis without further explanation.

1. ADC: Analog to Digital Converter.

An ADC converts the analog signal from a detector (e.g. from a detector's photomultiplier tube (PMT)) to a digital value. An important characteristic is the number of channels available in the ADC. This corresponds to the ability to digitize the analog signal, with more channels having a higher precision. Most of the PHOBOS ADC's have 4096 channels.

2. TDC: Time to Digital Converter.

Converts a time interval into a digital value.

3. TAC: Time to Amplitude Converter.

The “amplitude” is a voltage pulse height which is proportional to the time interval between two logic pulses (the start and stop) in fast NIM electronics. It is used for an online determination of the collision vertex.

4. Pedestal.

Electronic noise and (dark) leakage current of various components, even if there is no input signal, contribute to a non-zero analog output. The mean position of the corresponding ADC distribution is known as the pedestal, the width corresponds to the noise. An important characteristic of the detector is the signal to noise ratio (defined as the width of the pedestal relative to the mean of (real) signal).

5. MIP: Minimum Ionizing Particle.

One MIP corresponds to the energy a particle will lose when traveling through detector material.¹ For the Vertex detector, the MIP corresponds to ≈ 80 keV above the pedestal.

6. Gains and Calibrations.

One count in a particular ADC channel corresponds to the specific energy loss for that particle or event. This relation is most generally known as the *gain*. The gain is often

¹The energy loss of a particle is inversely proportional to the β^2 . With increasing velocity a minimum in dE/dx is reached. Particles at this point are called minimum ionizing.

different from detector to detector due to effects such as voltage settings or varying analog signal attenuation. The procedure of matching the gains in order that the same energy loss corresponds to the same ADC channel is known as a *gain calibration*. For the Paddle ADC channels, the voltages applied to the PMTs are such that the first MIP, after pedestal subtraction, are put at approximately the same ADC channel (channel 50).

7. NIM: Nuclear Instrument Module.

This is a standard in nuclear-experimental electronics. PHOBOS uses fast negative logic, where the logical 0 correspond to 0 V and logical 1 is -0.8 V.

8. Monte-Carlo simulations: MC.

Monte-Carlo simulations refer to theoretical models that generate collision events. They provide particle distributions close to what is expected in data by simulating the physics processes in the collisions. One of the most popular MC generators for heavy ion collisions is HIJING. After events are generated, interactions from the produced particles with the PHOBOS apparatus are simulated using the GEANT package (37).

9. PMC smearing: PHOBOS Monte-Carlo Smearing.

The energy loss for a given ADC channel, determined from GEANT, is found not to reproduce the data. Additional detector smearing is added to model the response of the detectors and associated readout electronics. Information about the smearing added to the MC in PHOBOS can be found in (38).

10. Collision vertex.

The collision vertex is the position in space (x, y, z) where the interaction between two

nuclei occur. For the PHOBOS experiment the measurement is relative to the center of the detector.

The PHOBOS Detector (2001)

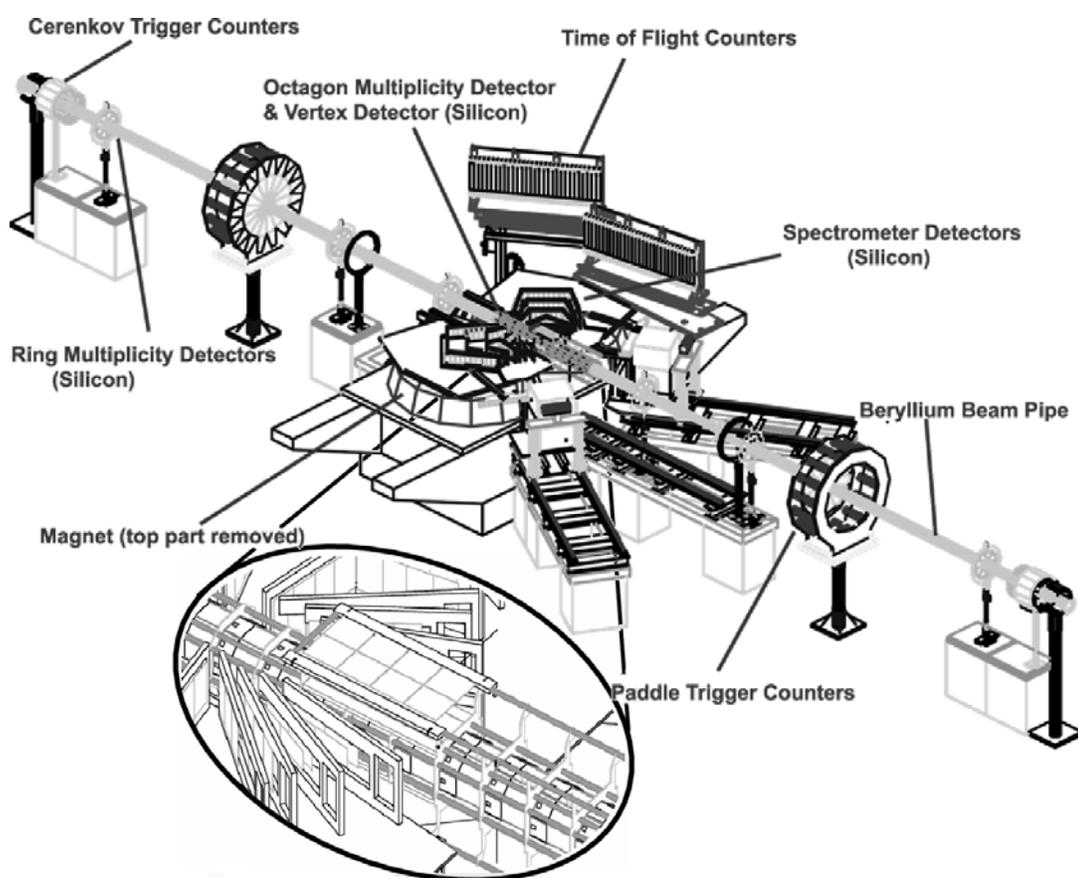


Figure 12. The PHOBOS detector setup for the 2001-2002 Au+Au run. The inset shows an enlarged view of the detector configuration closest to the interaction point with the Top Vertex detector planes visible and part of the Spectrometer and Octagon detectors.

3.2 Trigger system

When colliding heavy ion beams, not all events are of physics interest or occur in a usable region relative to the detector. Also, there are so many events per second (typically tens of thousands) that it is not possible to record all of them. The initial decision whether to save the events for further analysis consideration is made by the trigger system in fast electronics before they are digitized by the DAQ and written to tape. This system consists of the trigger detectors, NIM digital electronics and the DAQ.

The main trigger detectors for $Au + Au$ collisions at PHOBOS are the Paddles, Time Zero (T0), Čerenkov counters and Zero Degree Calorimeters. A brief description of the whole system follows.

3.2.1 Paddle counters

Each Paddle counter array (Figure 13) consists of 16 plastic scintillator slats, placed perpendicular to the beam at $z = \pm 3.21$ m from the nominal interaction point. These detectors cover $3.2 < |\eta| < 4.5$ for a nominal z -vertex position and 94% of the solid angle in this range. Their main advantage is that they cover a large area and have a fast read-out time. More information can be found in (39).

The primary use of the Paddles is to provide an efficient trigger for heavy ion collisions. The Paddles can also be configured to trigger exclusively on central (or peripheral) collisions and flag multiple events from different beam crossings (pile-up). Additionally, signals from these counters are used in offline event selection and centrality determination (through the truncated Paddle Mean), see Section 3.6.

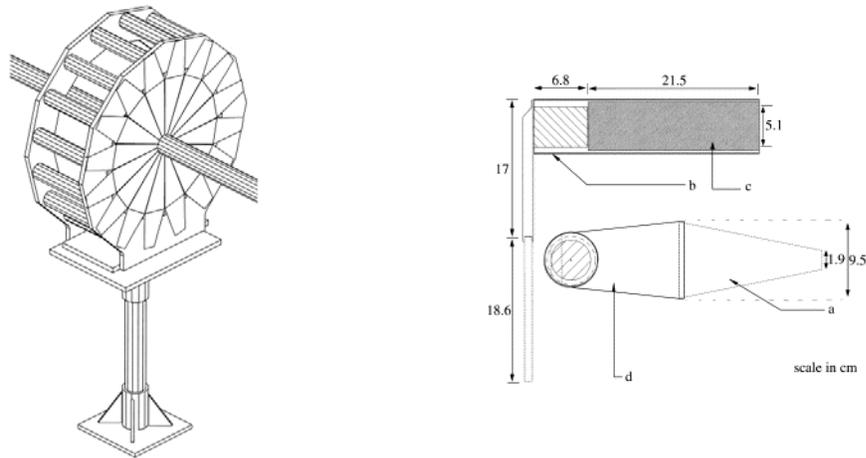


Figure 13. One Paddle counter array. Dimensions of a single slat and PMT shown on the right.

3.2.2 Time Zero counters

The T0's are the most important new addition to the trigger system, added for the PR03 d+Au run. These are two arrays of ten fast Čerenkov detectors. These arrays could be placed in a variety of positions, either symmetrically or in an asymmetric configuration around the interaction point (IP), depending on the collision system size and/or energy. For the $Au + Au$ collision system, the T0's were in the *out*-position at $\approx \pm 5.2 m$.

Initially introduced in order to provide a good online-vertex resolution (time) for TOF PID analyses, they also provide an ability to introduce a variety of new triggers. T0s are used as the main online vertex trigger (the start/stop for the TAC). The relative time resolution is 106 ps (less than 1.5 cm) for central Au+Au collisions.

3.2.3 Čerenkov counters

There are 2 additional arrays of 16 Čerenkov counters, situated after the third ring at $z = \pm 5.5m$ (behind the T0s). This symmetric system was designed initially to provide a fast online event vertex restriction (39). In the latest runs they are used as alternative information to the main triggers.

3.2.4 Zero Degree Calorimeters

Designed by a joint RHIC-experiment collaboration, the ZDC's provide necessary information for the accelerator functioning by monitoring the beam conditions in each experimental area, (40). The design purpose is to provide feed-back information to RHIC to ensure there are collisions occurring at each IP and give a measure of the luminosity at each experiment. Each ZDC consists of three tungsten-strip calorimeters. They are situated far down the beam-pipe on both sides of the IP ($\pm 18.5m$), behind the steering magnets.

The calorimeters measure the number of neutrons¹ not participating in the collision over a solid angle of 3.1 msr at a polar angle of 0° . This measurement is an important part of the event selection and centrality determination analysis. During the 2003-2004 run ZDCs were used in the trigger configuration directly to remove additional background, not previously observed in other production runs.

¹“free” neutrons, i.e. those not bound to other nucleons

3.2.5 Trigger logic

The trigger detectors provide information which characterizes the collision. NIM logic then uses this information for a fast, reliable decision as to whether a collision satisfies specific requirements. If these conditions are met, a signal is sent to the DAQ to record the event. The trigger logic is making decisions on two levels, known as Level 0 (L0) and Level 1 (L1).

L0 looks for some basic (loose) coincidences, occurring within 40 ns of the collision. A valid L0 decision starts the ADC and TDC digitization process for that event. L1 decisions are more restrictive, and often combine information from several detectors. The more restrictive decisions allow for a higher quality of data written to tape. If during some set time (500 ns after the L0 decision) an L1 condition has been fulfilled, the DAQ takes over and records the event. If no L1 comes, then the event is discarded.

All trigger control logic and synchronization (trigger board) is custom built¹ and uses a universal programmable logic module, described in (41).

3.2.6 The main triggers for this analysis

Data is recorded with a mixture of triggers on L1. This provides necessary information for event selection, centrality, trigger performance and beam quality. The event sample, though, is usually dominated by a particular trigger type, depending on the physics needs of different analysis groups. The main triggers used in the multiplicity analysis are outlined below.

¹by A.Sukhanov

MinBias PP*PN>0

This trigger requires at least one hit in each Paddle array, within a specified time interval (10 ns), yellow histogram in Figure 14, removing beam gas events. However, this trigger is susceptible to low multiplicity double beam gas events. These appear to be real collisions but do not pass further event selection criteria, such as ZDC timing requirements, see Section 3.5 for more details.

MinBias PP*PN>2

This trigger requires more than two hit slats in each Paddle array and also removes beam gas events. This is not so susceptible to low multiplicity double beam gas events, as a multiplicity of greater than two is required simultaneously on each array.

Online Vertex

Using either the Čerenkovs or T0 counters, the z -vertex range over which the collisions can occur is significantly reduced. This enhances the fraction of data occurring in the selected range, usually this is at the center of the PHOBOS detector. Special off-center runs can be made.

These three trigger configurations were used to collect the data presented in this Thesis. They are the most efficient triggers and ensure the least loss of peripheral events. Table I shows an example of the trigger mix for each dataset. Note that for some events all three triggers may simultaneously select an event, thereby the sum of the triggered events in a dataset can appear to be greater than 100%.

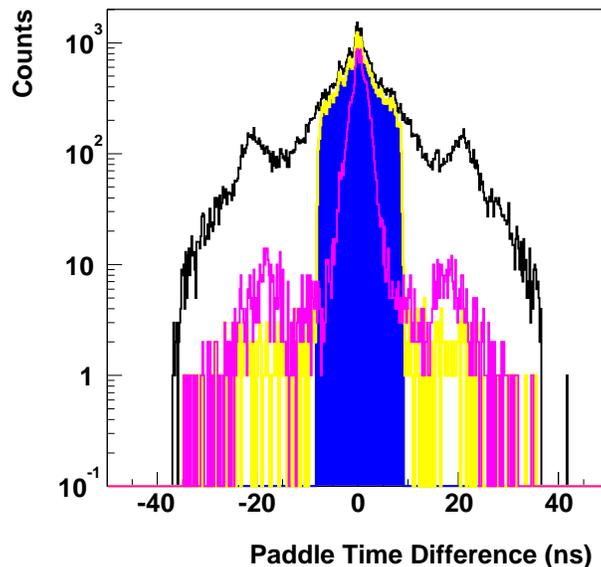


Figure 14. Black line corresponds to all triggered events, yellow is $MinBias PP*PN > 0$ triggered events, blue is $MinBias PP*PN > 2$. The purple histogram corresponds to the *Online Vertex* triggered by the T0s. The trigger mixture shown lets more $MinBias PP*PN > 2$ events compared to other triggers. Data shown is from one run in PR04 200 GeV.

3.2.7 Trigger and data quality

The performance of the trigger was monitored during the data taking by an *Online monitoring* and Trigger display system. Further checks were performed offline on a run-by-run basis from the *Trigger Inspector* software, developed by me. This proved vital when the PHOBOS trigger became more complicated in the $d + Au$ (PR03) run and the volume of data increased by a factor of ten over previous runs. At the same time, this proved an easy tool to perform

Year	Fraction of events recorded (%)		
	<i>MinBias PP*PN>0</i>	<i>MinBias PP*PN>2</i>	<i>Online Vertex</i>
PR01 pre	x	100	x
PR01 post	5	10	86
PR01 19.6	10	91	13
PR04 200	70	66	24
PR04 62.4mb	44	41	15
PR04 62.4vt	x	3	81

TABLE I

FRACTION OF EVENTS FROM A GIVEN DATA SAMPLE COMING FROM A SPECIFIC TRIGGER TYPE.

some detector trigger calibrations, beam quality monitoring, and event selection monitoring.

For further details see Appendix E.

As an example, Figure 15 shows the stability of the pedestal and MIP positions for a single Paddle counter over the whole PR04 Au+Au run. This careful tracking allowed to fine tune the trigger detector calibrations. Figure 16 represents the fraction of events from different triggers as monitored by the Inspector, over two days of data taking in PR04. This ensured collecting an uniform data sample, the observed small variations are due to changes in the overall beam conditions at the beginning and end of each accelerator store.

Monitoring the trigger detector performance is not only necessary for the general health of these detectors, but is also critical for the reliability of physics measurements. For example, the energy signals from the paddles are used for event centrality determination, any shift in the calibration of the signals in these detectors has to be tracked to ensure that the centrality definition for the whole run is consistent.

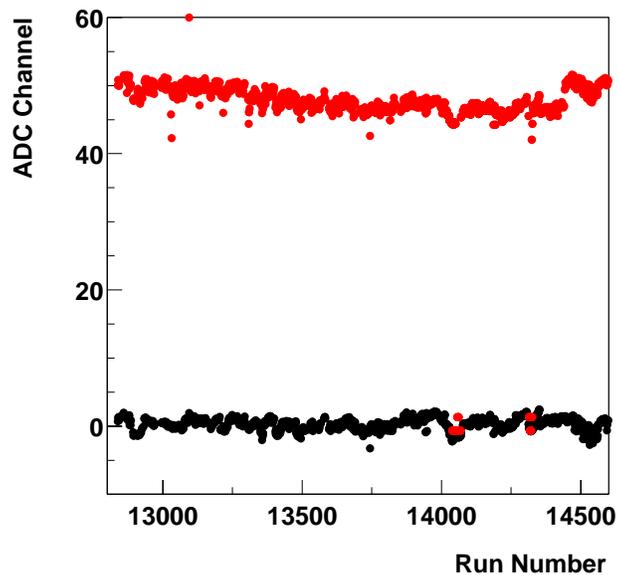


Figure 15. Paddle Positive 5, pedestal (black) and MIP (red) position tracking with the Inspector during PR04 200 GeV Au+Au. The deviation seen corresponds to test triggering runs.

3.3 Silicon based detectors

The PHOBOS multiplicity array and the two arm spectrometer use silicon pad technology. Depending on the specific design requirements for each detector, the pad (active area) size varies. The thickness of the wafers is between ≈ 300 and $340 \mu\text{m}$. More information about the technology, design, assembly and testing of the modules for the Vertex and other detectors can be found in (36) and (42).

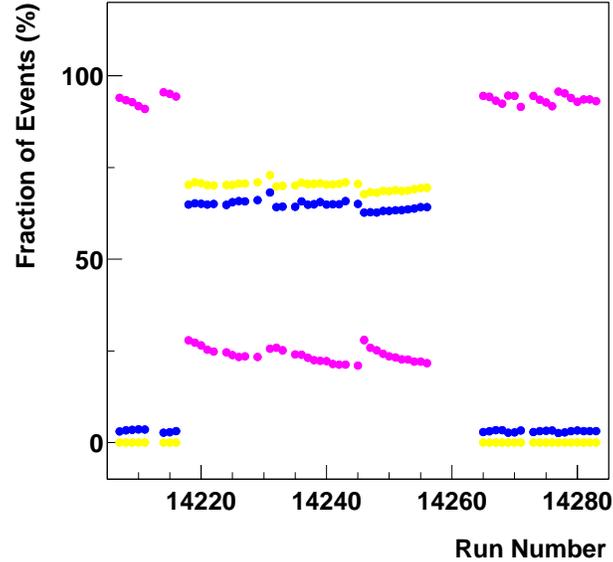


Figure 16. Tracking the fractions of triggered events with the Inspector. *MinBias* $PP*PN>0$ is shown with yellow markers, *MinBias* $PP*PN>2$ blue markers, and *Online Vertex* given from the T0s is with purple markers. The trigger mixture flips for predominantly **Vertex** and **MinBias** triggered datasets. Each marker is one run from PR04 200 GeV Au+Au data.

3.3.1 Vertex detector

The Vertex detector is the main detector used in the analysis presented in this Thesis. This detector is a compact silicon pad detector, situated close to the PHOBOS interaction point. The primary design purpose of this detector is to reconstruct the event vertex (the x, y, z coordinates of the collision position) to a high precision in z .

Figure 17 shows a schematic drawing of the Vertex detector. The detector consists of 4 horizontal silicon sensor planes, mounted on the Octagon frame. Two are located at 56.4

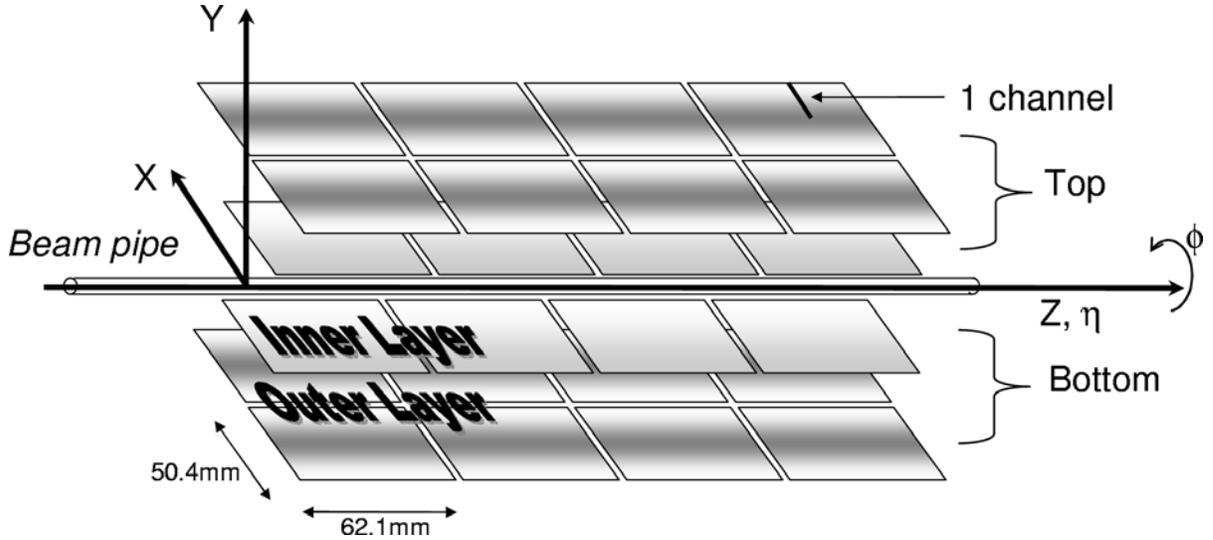


Figure 17. A schematic three-dimensional view of the Vertex detector.

and 117.8 mm above the beam pipe, and are known as the *Top Vertex*, the other two are symmetrically positioned below the beam pipe (*Bottom Vertex*). The detector is centered at $z = 0 \text{ cm}$, the nominal RHIC interaction point for PHOBOS. The *Inner* layers, closest to the beam pipe, are finely segmented, each having 2048 Si pads, with dimensions $0.47 \times 12.0 \text{ mm}^2$ in 4 silicon sensors. The *Outer* layers consist of 8 silicon sensors. These layers have the same number of channels, although wider (in x) than the Inner ($0.47 \times 24.0 \text{ mm}^2$). Each pad covers the same $\Delta\phi \approx 11.5^\circ$ by z . The pad size is made small in z to ensure a good vertex resolution (see Section 3.4.1) and a low number of hit pads per event. The coverage in η is smaller for the Outer Vertex and this determines the overall acceptance of the Vertex detector. For events with a nominal vertex position, the acceptance is $|\eta| < 0.92$ and $|\eta| < 1.54$ for the Outer and

Inner layers respectively. The azimuthal coverage is $\Delta\phi = 46.1^\circ$ for both the Top and Bottom detectors.

Figure 18 shows the average energy MIP position for data (black) and MC (red) in the Outer Vertex layers. The energy resolution, which is given by the ratio of the Signal (MIP peak) to noise (pedestal width) exceeds twice the design value and is found to be $S/N \approx 24$.

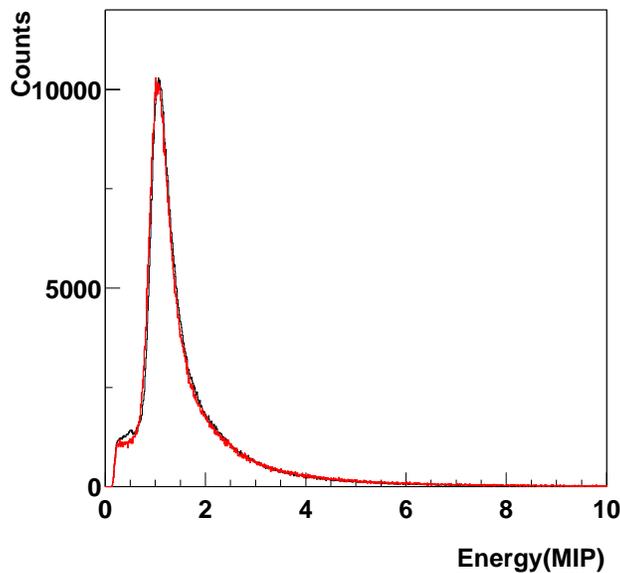


Figure 18. Average energy MIP for hits in Inner Top Vertex layer, for data (black) and MC (red).

3.3.2 Silicon detectors and data quality

PHOBOS has established a common silicon signal processing routine for all (Si) detectors. ADC signals for each sensor are preprocessed immediately after the data had been recorded, on a run-by-run basis. The mean pedestal position for each pad is calculated and subtracted from the ADC signals. Then, the procedure converts the ADC signal into a deposited energy (in keV units). One ADC channel corresponds to ≈ 2.1 keV. Next, MIPs are all aligned to ≈ 80 keV, depending on the thickness of the specific silicon wafer. All the detector hit information is finally collected and organized into a common *Hit Array* ready for data analysis.

3.3.3 Dead and hot channel map

For each data run, a software mask is applied to the silicon detectors to exclude pads from the analysis that do not operate properly, known as the dead channel map. Pads that do not respond to charged particles traversing them are flagged as dead. Pads that produce a signal, even if no charged-particle is present are marked as hot. An example for masked non-working pads, for PR01 postblast data, in a single sensor is shown in Figure 19.

3.4 DAQ and software

The signals from all PHOBOS detectors are converted to a usable format by the Data Acquisition system. This process has an intrinsically long readout time to record the silicon signals. The performance of the DAQ has dramatically improved over the operation of the PHOBOS experiment. The rate with which the data is written to disk has increased from 28 Hz (PR01) to 250 Hz (PR04) and is expected to reach up to 500 Hz (PR05). This success

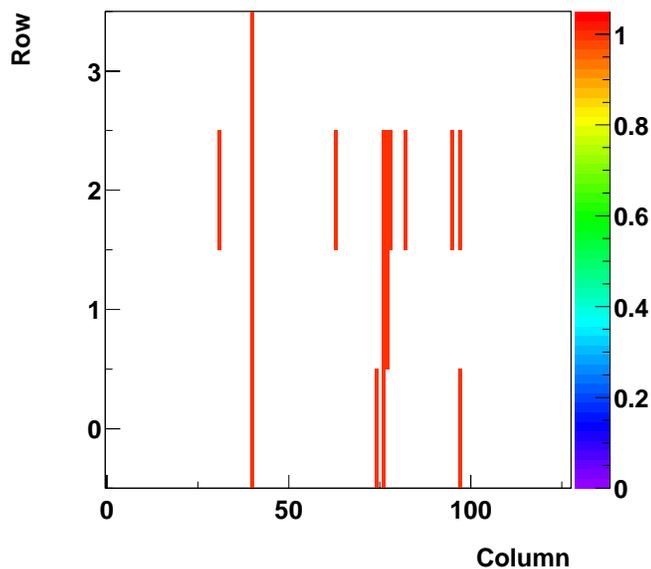


Figure 19. Non-working channels (dead or hot) in one silicon sensor, Top Vertex - Inner plane.

has enabled the experiment to take increasing amounts of valuable data. A description of the DAQ system, data compression, storage, event building and run control is given in (41).

3.4.1 Vertex finders

The Vertex finders were developed in PHOBOS at the beginning of the experiment and during the low multiplicity d+Au run (PR03). PHOBOS has a prolific set of vertex reconstruction algorithms, which use almost all detectors: Vertex, Octagon, Spectrometer, Paddle counters, T0s and other detectors. The details of the vertex finders are currently under publication preparation. Three main vertex reconstruction algorithms were used to obtain the multiplicity

results and event selection in this Thesis. The accuracy of these algorithms for the analyzed datasets are presented in Table II and Figure 20.

Energy	Algorithm	Central			Mid-central		
		σ_x mm	σ_y mm	σ_z mm	σ_x mm	σ_y mm	σ_z mm
200 GeV	ZVertex	n/a	0.16	0.07	n/a	0.19	0.08
	SpecMainVertex	0.26	0.25	0.32	0.47	0.44	0.56
	RMSSelVertex	0.17	0.16	0.07	0.36	0.19	0.08
62.4 GeV	ZVertex	n/a	0.16	0.07	n/a	0.19	0.08
	SpecMainVertex	0.29	0.26	0.31	0.56	0.46	0.62
	RMSSelVertex	0.21	0.16	0.07	0.43	0.19	0.08
19.6 GeV	ZVertex	n/a	0.18	0.08	n/a	0.23	0.10
	SpecMainVertex	0.34	0.32	0.40	0.62	0.51	0.77
	RMSSelVertex	0.29	0.18	0.76	0.56	0.24	1.04

TABLE II

VERTEX RECONSTRUCTION RESOLUTION FOR THE THREE AU+AU DATASETS. THE CENTRAL CORRESPONDS TO THE TOP 10% AND MID-CENTRAL FOR THE 40%-50% FRACTION OF CROSS-SECTION.

1. *ZVertex*

The ZVertex is a high resolution vertex finding algorithm utilizing the Vertex detector. Clusters of hits are produced, similar to the merging procedure discussed in Section 4.1, then probability histograms of the number of clusters as function of z are created. This imposes a limit on the vertex search range. Next, combinations of clusters from the Inner

and Outer layers are considered and projected back to the x - z plane. This then produces another probability histogram, where the peak is considered to be the found z -position. The level of the projection plane (x - z plane) is then changed until the height of the peak is maximized. This produces the y coordinate. Due to the large pad size in x , no information is available for that component.

2. *SpecMainVertex*

This reconstructs vertices by finding tracks from the first four planes from both arms of the Spectrometer. This provides x, y, z coordinates of the event vertex, although the resolution in z is not as precise as ZVertex.

3. *RMSSelVertex*

RMSSelVertex combines information from five different vertex finders. The selection is based on MC studies, as function of centrality, to determine which algorithm reconstructs the most accurate x, y, z components in a given centrality class. For a given event, the vertex is formed by selecting components from any vertex finder, but not necessarily from the same algorithm. Note: RMSSelVertex was not optimized for the 19.6 GeV dataset.

3.5 Event selection

Having a clean, uniform event sample, without losing too many events is very important. This is known as event selection, usually done after the data is taken, but before the physics analysis begins. Even if the trigger is performing as expected, small variations in beam quality or unexpected changes in the detector performance can cause problems. For this analysis, event

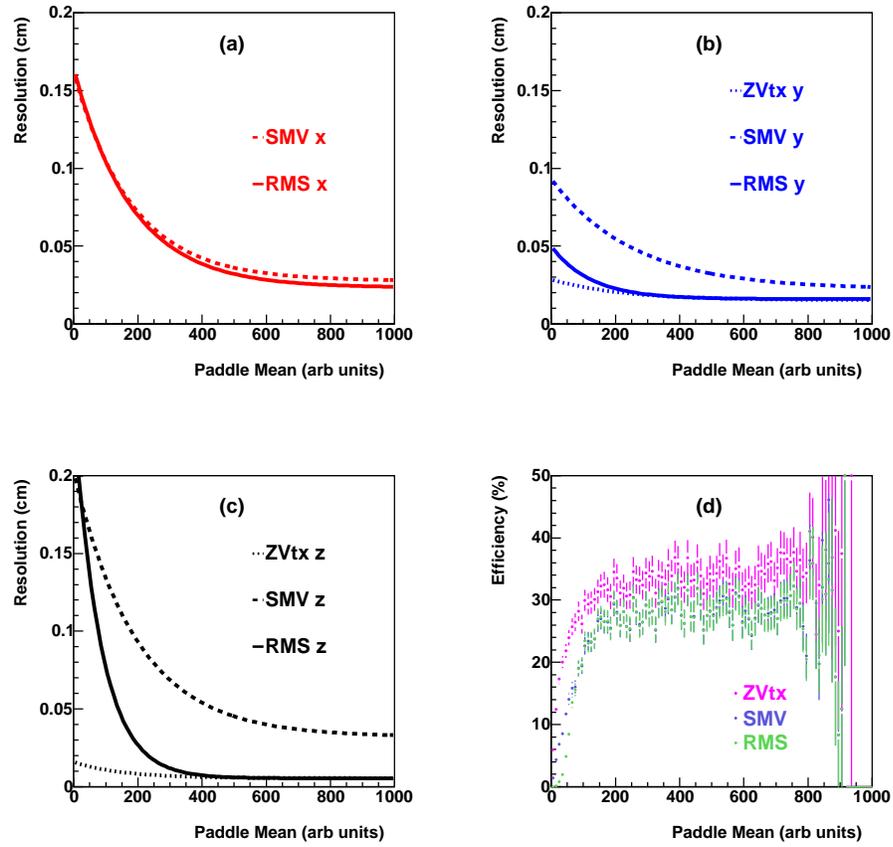


Figure 20. Vertex resolution for x, y, z components for 62.4 GeV MC as a function of centrality. The efficiency (for ± 10 cm) is also shown, relative to the $n > 0$ trigger.

selection removes non-collision and calibration events and restricts the data sample to a usable vertex region.

3.5.1 200 GeV Au+Au event selection

The rejection of non-collision events is performed by using the timing information from the Paddle counters and ZDCs relative to the crossing-clock. Central events have to satisfy additional multiplicity conditions to avoid the rejection of very central events, where no neutral spectators remain to trigger the ZDCs. A reconstructed event vertex within ± 10 cm is also required. This additional cut is applied for consistency with other multiplicity analysis, as this provides the optimum overlap between different detectors.

For the events to be selected, they have to pass the following cuts:

$$\text{GoodPaddleTime AND (GoodZDCTime OR VeryCentralEvent)} \quad (3.1)$$

$$\text{GoodPaddleTime} = |t_{PdN} - t_{PdP}| < 4ns \quad (3.2)$$

$$\begin{aligned} \text{GoodZDCTime} = t_{ZDCN} > 512ns \text{ AND } t_{ZDCP} > 512ns \text{ AND} \\ t_{ZDCN} + t_{ZDCP} > 1240ns \end{aligned} \quad (3.3)$$

$$\text{VeryCentralEvent} = \text{Sum}_{PdN} > 1500 \text{ AND } \text{Sum}_{PdP} > 1500 \quad (3.4)$$

The letters N and P stand for the negative and positive detector arrays.

3.5.1.1 Paddle time restrictions

Figure 21 shows the time difference between the two Paddle counter arrays, i.e. the difference between the fastest time signals from each array. The requirement for the Paddle time difference

to be less than 4 ns, red line, corresponds to events which occur in ± 60 cm of the nominal vertex. (Within this cut, the selected events have approximately the same maximum multiplicity in the Paddles, see for example Figure 26.) The beam-gas peaks, due to the non-collision events outside the Paddles, are removed. These peaks are fixed by the distance between the two arrays and are at $\approx \pm 20$ ns. The GoodPaddleTime cut is passed by 46% of the events in the considered trigger sample. If a valid event vertex within ± 10 cm is required, green line, only 7% of the initial event sample is left.

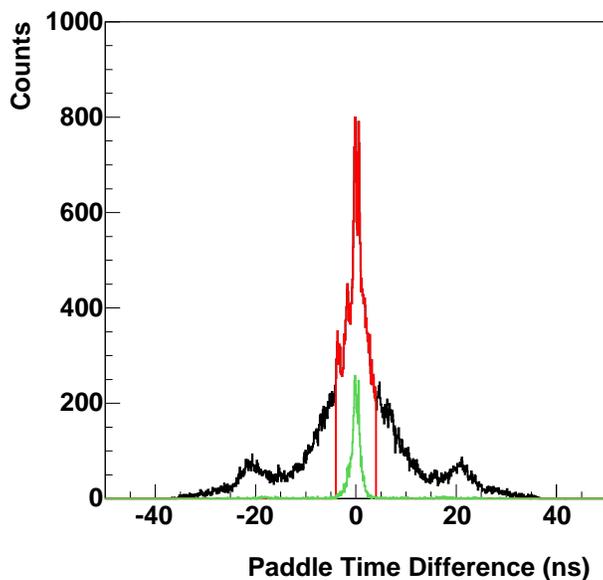


Figure 21. Event selection and Paddle time restrictions. The black line corresponds to all triggered events, the red line are events which pass the GoodPaddleTime cut, Equation 3.2. The green line represents the events with a reconstructed vertex within ± 10 cm.

3.5.1.2 ZDC time restrictions

The three timing requirements in GoodZDCTime remove all single and double beam-gas events. For a ZDC trigger, the spectator neutrons must traverse the ZDC with a minimum energy greater than the set threshold of ~ 60 GeV. For beam gas collisions, only one ZDC (on the positive or negative side) could be struck by the neutrons, therefore not passing the time requirement. The time signals from the ZDCs are very stable over the whole run, as shown in Figure 23.

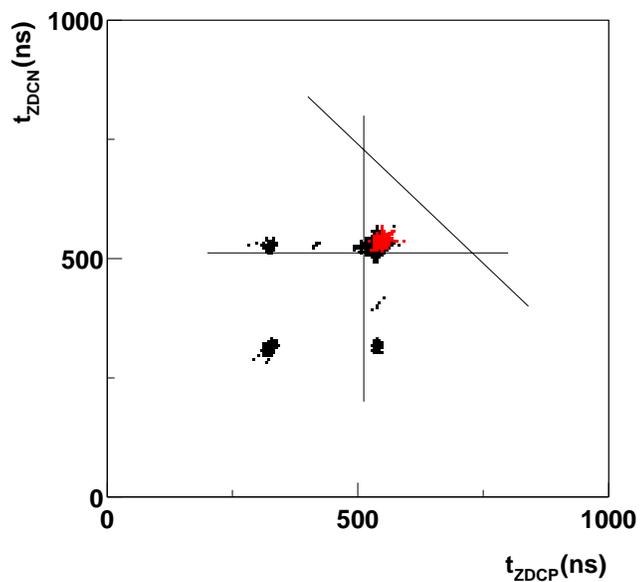


Figure 22. Event selection and ZDC time restrictions.

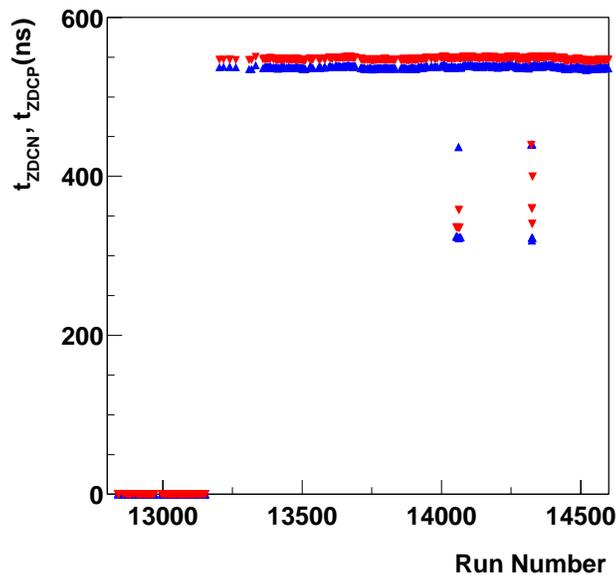


Figure 23. Stability of the ZDC time signals for PR04 200 GeV Au+Au, as tracked by the Inspector. t_{ZDCN} (blue) and t_{ZDCP} (red) were not read at the beginning. The deviation seen corresponds to test triggering runs.

3.5.1.3 Paddle energy signal

For very central events, no spectator neutrons may be available to impact the ZDCs. In this case a cross-check with the Paddles is performed to ensure there is no loss of very central events. Figure 29 shows that this additional event selection criteria was not needed for 200 GeV. There are no central events without signals in the ZDCs. The centrality variable in this figure, called *Paddle Mean*, is defined in Section 3.6.1.

3.5.2 62.4 GeV Au+Au event selection

The event selection for 62.4 GeV is very similar to that for 200 GeV (Equation 3.1). The ZDCs thresholds were not calibrated for that short run and two neutrons were needed to trigger the ZDC on each side. The left panel of Figure 24 shows that for the most central events (large Paddle Mean) there are events that are missing signals in the calorimeters and the distribution is “cut”, compared to Figure 29. To ensure that these events are not omitted, the requirement of Equation 3.4 is modified such that Equation 3.5.

$$\mathbf{VeryCentralEvent} = Sum_{PdN} > 300 \text{ AND } Sum_{PdP} > 300 \quad (3.5)$$

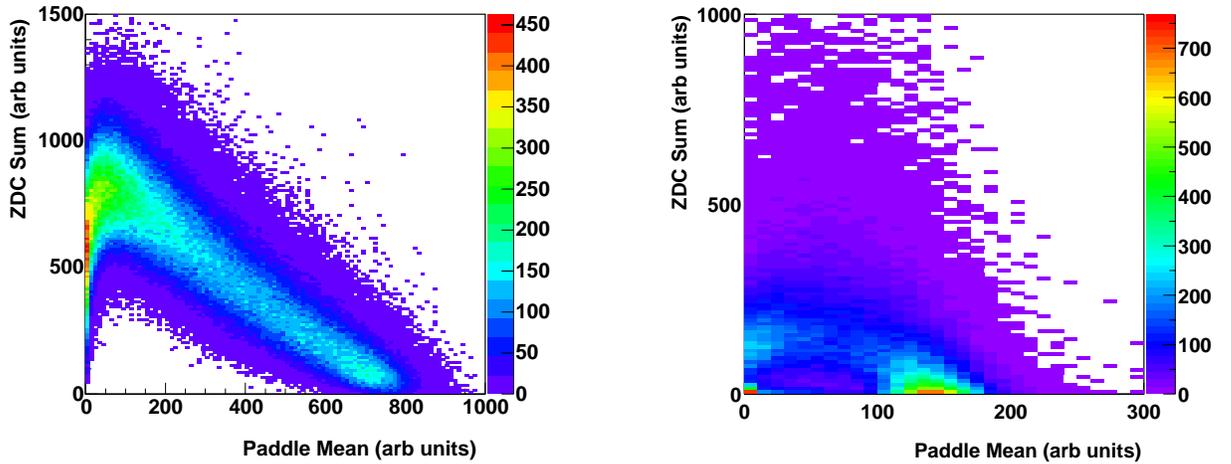


Figure 24. ZDC and Paddle signal anticorrelation for 62.4 GeV (left panel) where some central events are missed. The right panel shows the same anticorrelation for 19.6 GeV where most central events are missed.

3.5.3 19.6 GeV Au+Au event selection

Event selection for this energy relies on reconstructed vertex information. ZDC timing information could not be used as the calorimeters were not optimized for this short run (actually 6 neutrons were needed to trigger the ZDCs on each side), see Figure 24 (right panel). Paddle timing was not sufficient enough to provide a clean event sample. As can be seen from Figure 21, a vertex finder requirement can provide a sample within GoodPaddleTime for 200 GeV. A combination of two vertex finders, using information from different parts of the detector, provided the event selection for 19.6 GeV:

$$\textit{Valid ZVertex AND Valid SpecMainVertex AND } |SpecMainVertex z| < 10\textit{cm}, \quad (3.6)$$

Applying the additional GoodPaddleTime cut removes the tails of the selected distribution, Figure 25, but as it can be seen from Figure 26 these events are not from a particular centrality class or vertex position and they are less than 1% of the total events.

Also in Figure 26, ZVertex is found to mis-reconstruct events from outside the Vertex detector as though they originate from the ± 10 cm range. This is the reason that SpecMainVertex was used as the main vertex finder for the event selection and for the analysis.

3.5.4 Additional event selection criteria

The pile-up events are flagged during the data taking. As can be seen from Figure 27, they are not connected to a specific centrality class. Because the effect of pile-up on centrality determination and different analyses was not studied prior PR04 run, these events are explicitly

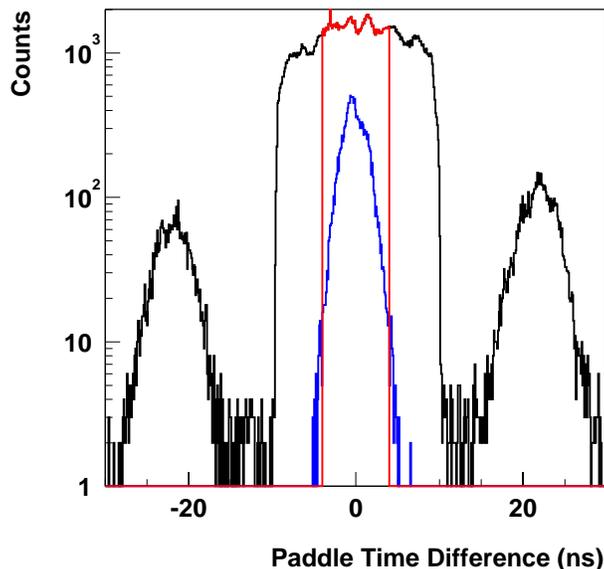


Figure 25. Paddle time difference and event selection for 19.6 GeV. The black line corresponds to all triggered events, the red line are events which pass the GoodPaddleTime cut, Equation 3.2. The blue line represents the events which pass the event selection cut for 19.6 GeV, Equation 3.6.

removed for the 62.4 GeV multiplicity analysis. (A cross-check was performed with and without this event selection, no effect was seen on the final result.)

3.6 Centrality of the collision

To find the centrality some basic steps are followed. The procedure starts with event selection, which will ensure a clean and uniform event sample. Next, the event selection efficiency has to be estimated to account for the missed part of the cross-section, imposed by trigger. After some careful considerations, a variable from data is chosen for the measure of collision

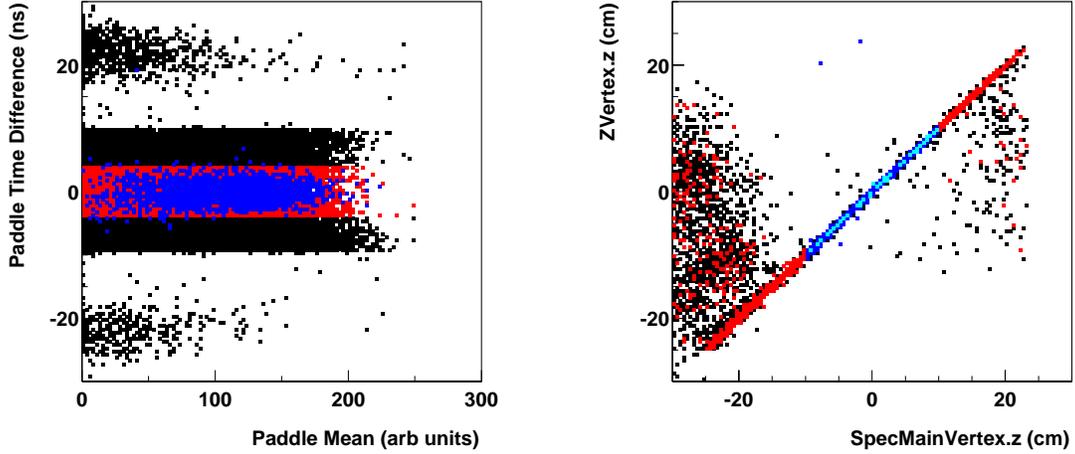


Figure 26. Event selection and Paddle time restrictions for 19.6 GeV. The black symbols correspond to all triggered events, the red symbols are events which pass the GoodPaddleTime cut, Equation 3.2. The blue symbols represent the events which pass the event selection cut for 19.6 GeV, Equation 3.6.

centrality. One requirement made here is that this variable correctly tracks the collision geometry, such that it will have a monotonic dependence with the number of participants. The next step is to map the same simulated variable in MC to the corresponding number of participants. Finally, the $\langle N_{part} \rangle$ found in MC for a given fraction of cross-section is associated to the same fraction found from the measured quantity in data. This defines the centrality.

The centrality of an event is presented as a percentile of the inelastic cross-section, where a small percentage (e.g. 3%) corresponds to a central event.

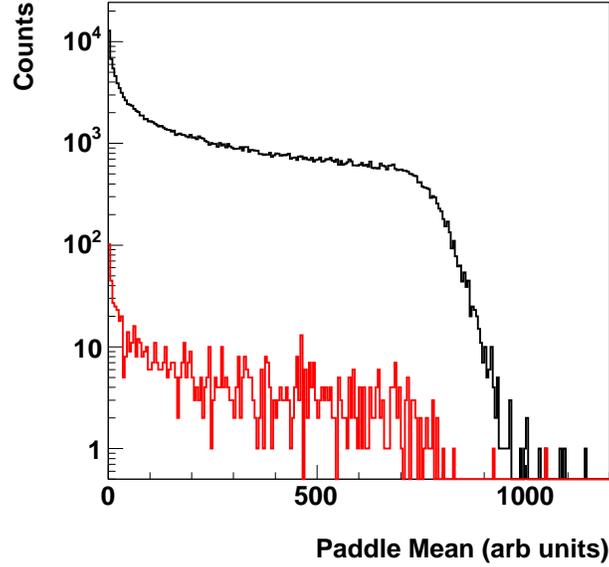


Figure 27. Pile-up and event selection for 62.4 GeV. The black line corresponds to all triggered events, the red line are events with pile-up removed.

3.6.1 Paddle Mean centrality overview ($\sqrt{s_{NN}} = 200$ and 62.4 GeV)

Paddle counters are not only used for triggering, but they are also utilized as a means to estimate the overall detection efficiency and to determine the centrality of the collision. The trigger efficiency is estimated using the number of paddle hit slats in data and MC (Figure 28). The two distributions are matched in a region where there is a common plateau and the efficiency is calculated using Equation 3.7. In this way the detailed distribution in MC is not wholly relevant and what matters is the missing cross-section for peripheral events. This procedure can be applied to both the $N > 0$ and $N > 2$ triggered data. The efficiency for the MinBias

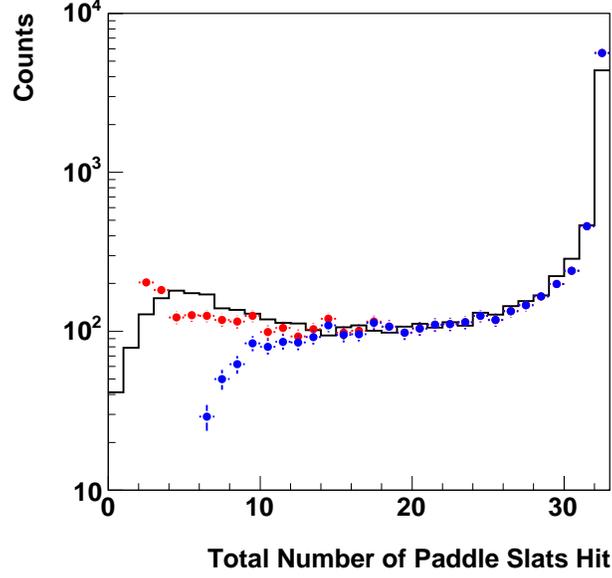


Figure 28. An example of the trigger efficiency determination for both the $N > 0$ (red) and $N > 2$ (blue) data in 200 GeV collisions. The black histogram is the MC reference.

trigger was determined from MC studies using HIJING and a full GEANT simulation of the PHOBOS detector and is $97 \pm 2\%$ for 200 GeV Au+Au data. The efficiency for the $N > 2$ trigger is $88 \pm 2\%$ for the same dataset.

$$\epsilon = \frac{N_{Events}^{Data}}{N_{Events}^{MC}(Nn + Np \leq 15) + N_{Events}^{Data}(Nn + Np > 15)} \quad (3.7)$$

The truncated Paddle mean, *Paddle Mean*, is the variable chosen to determine the centrality (Figure 29(a)). It is a sum of the 12 lowest deposited energy values on each Paddle array.

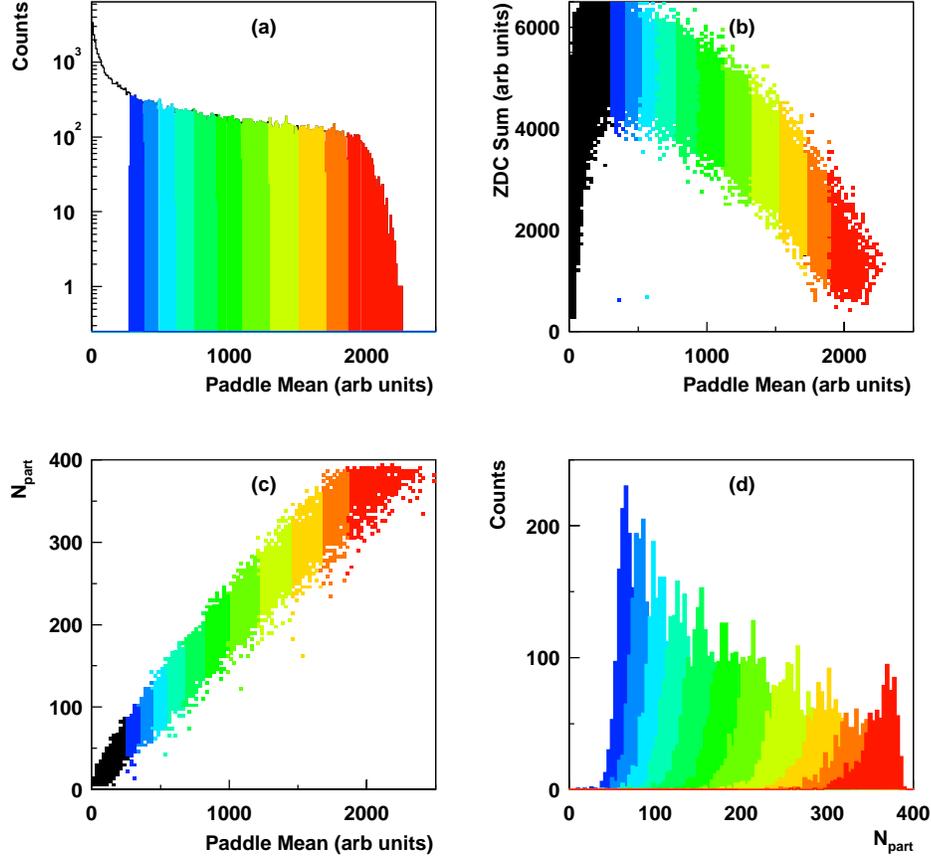


Figure 29. Centrality determination with Paddles.

This distribution is strongly anti-correlated with the ZDC sum for the central 50% of the cross-section (Figure 29(b)). Since the ZDC's directly measure the number of spectator neutrons, this gives us confidence that the Paddle Mean will be correlated with N_{part} . From MC (HIJING) a monotonic relation of the Paddle Mean and N_{part} is observed (Figure 29(c)). The same Paddle variable distribution in MC is split into percentile of cross-section bins, this distribution

represents an unbiased sample of the full geometrical cross-section. For each cross-section bin an average N_{part} is found (Figure 29(d)).

In data, the Paddle Mean distribution is additionally corrected for the trigger (in)efficiency (to calculate the expected number of events if unbiased) and then sliced into percentile bins. The found $\langle N_{part} \rangle$ in MC is associated to the same cross-section percentile slice in data. The data is considered only for the top 50% of the cross-section, where there is no loss of events due to triggering or the requirement of a found collision vertex.

3.6.2 EOct centrality overview (all energies)

The 19.6 GeV dataset was triggered with an $N > 2$ requirement in the Paddles. The trigger was sensitive to $\approx 80\%$ of the total inelastic cross-section, determined by MC simulations. The anti-correlation between Paddle Mean and the ZDC sum is not strong enough to allow the use of Paddle Mean as a centrality variable (Figure 24 (right panel)). This is partially due to needing six neutrons to trigger a ZDC counter at this low collision energy. Additionally, the Paddle counters covered a different area of phase space at 19.6 GeV, compared to 200 GeV, with different rates of particle production (Figure 47). The total yield observed in the Paddle counters was not enough to cleanly separate central from mid-peripheral data. Thus, the Paddle Mean variable was ruled out as a viable centrality determination measure.

A signal proportional to the liberated energy in the Octagon detector (at mid-rapidity), is used to determine the centrality at 19.6 GeV. This variable, $EOct$, additionally requires a valid event vertex for the merging and angle correction of hits in the Octagon. The resulting dataset is then not only biased by the intrinsic trigger efficiency, but also by the vertex reconstruction

efficiency. At $\sqrt{s_{NN}} = 19.6$ GeV, the trigger+vertex efficiency is found from the ratio of data and MC yields after shape matching the multiplicity distributions in the considered pseudorapidity region ($|\eta| < 3$). The matching is performed only for the 100% efficient region, i.e. the region of most central collisions.

After successfully establishing the method for 19.6 GeV, the centrality determination using signal from the whole or part of the Octagon detector was applied to all other energies. EOct based centrality determinations have vertex+trigger efficiency of $66\pm 2\%$, $60\pm 2\%$, $55.4\pm 2\%$ for 200, 62.4 and 19.6 GeV data respectively. The same value of $66\pm 2\%$ is applicable for 200 GeV Paddle Mean centrality determination when the same vertex bias is applied.

In this Thesis, the Au+Au data from three different $\sqrt{s_{NN}}$ are presented. The centrality determination, including evaluation of all systematic errors arising from it, was performed by Richard Hollis and more details can be found in (43). Here, only the relevant information about centrality will be discussed, without further reference to this work.

CHAPTER 4

TRACKLETS

The *Vertex tracklets* method is used to measure the produced primary charged particle multiplicity at mid-rapidity and derives its name from the Vertex detector which is used in the analysis. A “tracklet” is a two point straight line, that is extrapolated back to the reconstructed event vertex. The method was originally developed by Michael Reuter (44), to reconstruct multiplicity for 130 and 200 GeV $Au + Au$ collisions. The description of the method, which follows, presents the basic analysis reconstruction steps and introduces some modifications and additional checks performed in order to obtain the results for the $\sqrt{s_{NN}} = 200, 19.6, 62.4$ GeV collisions for the top 50% of the inelastic cross-section.

The expansion of the analysis to provide a high precision results on the ratio of two datasets as well as to extend to the future lower centrality measurements is described in the second part of this Chapter.

4.1 Reconstruction procedure

Numerous particles are produced during the collision of two gold nuclei, all originating from a common point in space, the event vertex. A schematic view of the top two planes of the Vertex detector is shown in Figure 30. Only charged particles, traversing the Inner and/or Outer Vertex planes, will liberate charge in the silicon sensor pads of this detector (shown in colors on the left panel of the figure), which are then amplified and read out electronically. This

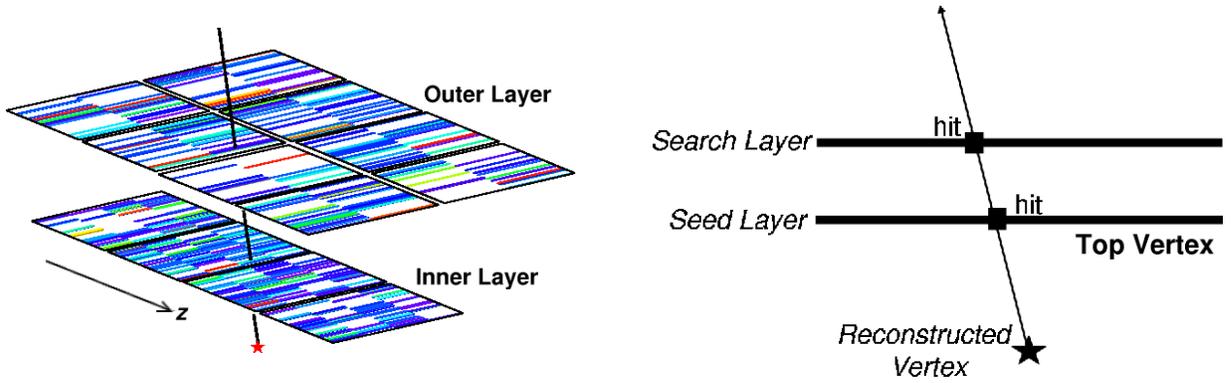


Figure 30. Hits (left) are shown for a central event in the Top Vertex planes. A tracklet, connecting two hits and the event vertex is also shown. An $z - y$ projection is shown (right) for the same tracklet.

information, along with the known position of each detector pad relative to the collision vertex, can be used to reconstruct the number of charged particles produced in the collision.

As described in Section 3.3.2, the silicon signals are pedestal subtracted and gain calibrated and form the *Detector hits*.

The *pre-analysis* starts from these Detector hits and ends with the *Vertex hits*. The first step in the pre-analysis is the initial cut on the Detector hit signals. This cut, at 15 keV, is applied to all hits to remove any noise residues (pedestal). After this, a merging procedure combines adjacent hits in the z -direction. Due to the small dimensions (0.47 mm) of the silicon pads along the $z(\eta)$ -direction, particles emitted at polar angles smaller than 33° (or $|\eta| > 1$) have 50% probability of traversing more than one pad. From simple geometry considerations, the maximum number of hit pads from one charged particle is two. A final Vertex hit is retained

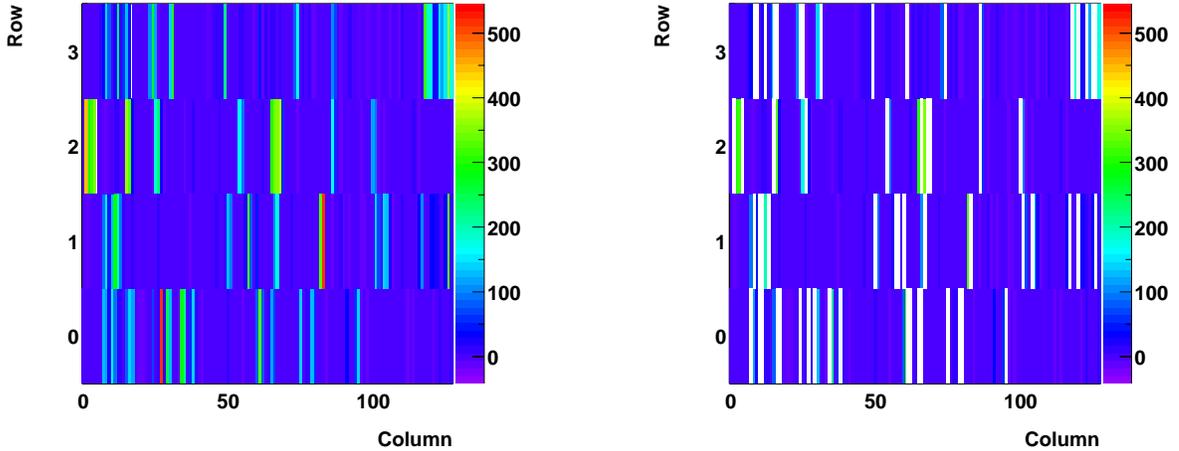


Figure 31. The left panel shows the Detector hits (non-merged) in one sensor in the Top Vertex, Inner plane for one central event at 200 GeV. The z -axis represents the energy deposited (keV). Colors other than dark-blue/purple are Detector hits. The white lines in the right panel represent the merged hits (Vertex hits) for the same sensor and event.

only if the sum of the energy of the two Detector hits is above 40 keV (which corresponds to approximately half of one MIP).

The precise position of a Vertex hit is calculated with an energy weight toward the pad with the higher energy liberated in it. Figure 31 displays the hits in part of the Vertex detector before and after the merging procedure is applied. The final Vertex hits are associated with energy deposited from one charged particle. As can be seen from the figure, the occupancy in the detector is low even for these very high multiplicity events.

The Vertex hits do not provide enough information to reconstruct the charged particle track alone. Knowledge of the event collision vertex is crucial for this analysis. With the help of the

reconstructed collision vertex, the η and ϕ position of each Vertex hit are calculated. A tracklet is formed if the differences $\delta\eta$ and $\delta\phi$ of two hits in the Inner (hit1) and Outer layer (hit2), known as tracklet residuals, satisfy the following conditions:

$$\delta\eta = |\eta_{hit1} - \eta_{hit2}| < 0.1 \quad (4.1)$$

$$\delta\phi = |\phi_{hit1} - \phi_{hit2}| < 0.3 \quad (4.2)$$

The larger value for $\delta\phi$ (in Equation 4.2) is due to the different granularity of the Vertex sensors in z (η) and x (ϕ) directions.

There are two distinct ways to combine the Vertex hits into a tracklet. First, a hit from the Inner layer is chosen as a starting point (the *Seed layer*). All possible tracklet combinations with hits from the Outer layer (*Search layer*) are then formed. Iterating through all hits from the Seed layer and forming all possible tracklets for each seed hit gives the total number of tracklets for the Top Vertex detector. The procedure could be performed in reverse, i.e. selecting the Outer layer for the Seed, Inner for the Search layer.

Some tracklets share a common hit in the Search layer. The tracklet with smallest $\delta\eta$ residual is retained (known as the second pass condition). The total number of tracklets in the Vertex detector is a sum of the tracklets reconstructed in the Top and Bottom Vertex. As described in (44), the results obtained with the two different search methods are consistent and all results presented here are with the Outer Vertex as the Search layer.

Not all tracklets, reconstructed in the above manner, will be real. Some will be random combinations of hits which happen to point back to the event vertex. These tracklets are known as the *Combinatorial background* tracklets, see Section 4.2.1. To summarize, the number of charged particles ($dN/d\eta$) is found by reconstructing all tracklets in the Vertex detector ($N_{tracklets}$) and subtracting the combinatorial background (N_{comb}). Finally, to appropriately account for missed or over-counted tracklets (in the full azimuth) a common correction factor to the total number of reconstructed tracklets is applied, see Equation 4.3. The overall correction factor is denoted by α .

4.2 Corrections

All corrections are based on the MC studies using the HIJING event generator (34) and a full GEANT (37) simulation of the PHOBOS detector. The standard PHOBOS “smearing” is applied to all detector hits in the MC (see Section 3.1).

For each event the number of reconstructed tracklets in data and MC is corrected for combinatorial background, geometrical acceptance of the detector, tracklet reconstruction efficiency and feed-down (mostly weak decays of neutral strange particles). Most of these corrections depend on the multiplicity of the produced charged particles in the event (OHB) and the z -vertex position.

$$\frac{dN}{d\eta}(OHB, z_{vertex}) = \frac{N_{tracklets}^{Data} - N_{comb}^{Data}}{\alpha} \quad (4.3)$$

$$\alpha(OHB, z_{vertex}) = \frac{N_{tracklets}^{MC} - N_{comb}^{MC}}{N_{primaries}^{MC}} \times \Delta\eta \quad (4.4)$$

For the multiplicity measurement using the Vertex detector, the acceptance in η is between -1 and +1, which gives a total pseudorapidity region of two units, i.e. $\Delta\eta = 2$, see Equation 4.4.

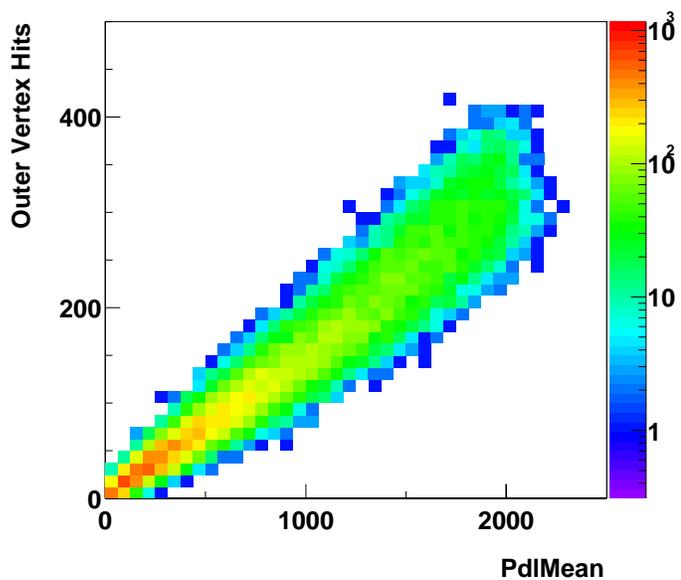


Figure 32. 200 GeV data, Outer Vertex hits versus Paddle Mean. This illustrates that the Outer Vertex hits can be used as a measure of centrality.

The multiplicity variable *Outer Hit Bin*, OHB, is introduced as the way to account for the change in correction factor, α , as a function of the event centrality (see Figure 32). This uses a measure directly from data, and is an alternative to the usual Paddle Mean centrality variable. Because the Vertex detector samples only a quarter of the ϕ space distribution, flow effects for

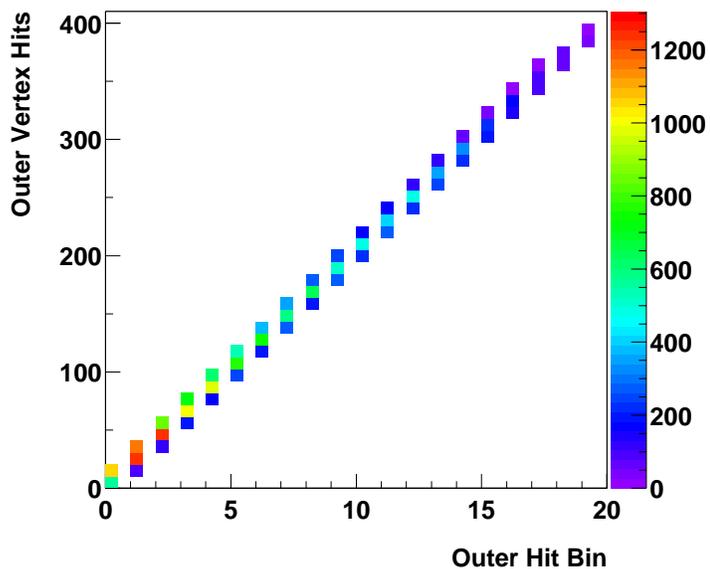


Figure 33. 200 GeV data, Outer Vertex hits versus OHB.

events within the same centrality class could be large (up to 8% in 200 GeV (45)). These effects would not be taken into consideration in a correction factor explicitly based on the centrality class (Paddle Mean). OHB, on the other hand, is a direct measure of multiplicity in the Vertex detector, independent of collision orientation effects. The OHB, for a given event, is found by dividing all Vertex hits in the Outer Vertex planes by an integer number, chosen to be 20 for all energies, Figure 33. The huge advantage of using the OHB is that the same correction factors can be used for all energies and introducing new centrality measures is decoupled from the analysis.

4.2.1 Combinatorial background

In order to measure the number of random combinations of hits which form tracklets, the two Inner detector planes are rotated 180° around the beam pipe, in software. This measure is accurate only when the number of hits in the Top and Bottom Vertex is approximately the same. For the case of asymmetric hit distributions, the level of combinatorial background tracklets will be different between the true and rotated positions of the detector. For example, if the beam has an offset in y the number of Vertex hits will not be the same. However, the procedure will still work due to the average of hits in the definition of OHB, a lower level in the top planes would be counter-balanced by an excess in the Bottom Vertex detector.

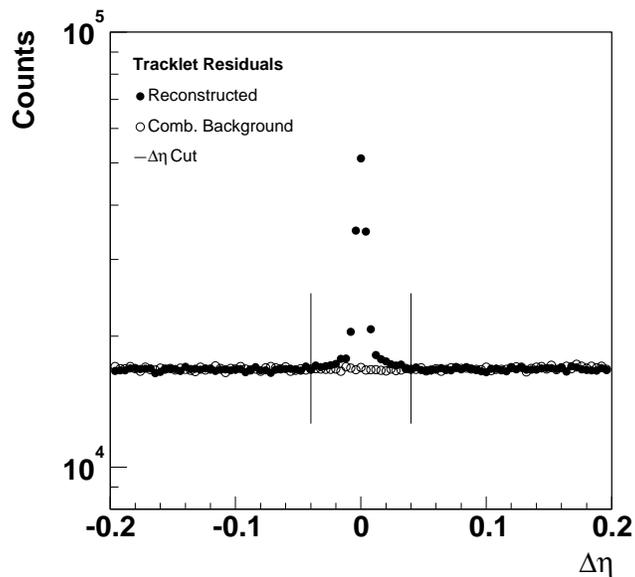


Figure 34. Tracklet residuals in η for OHB 5 for data.

An additional cut position on the tracklet residuals of $|\delta\eta| < 0.04$ is imposed, where the signal and background in data (or MC) are found to no longer deviate, see Figure 34. The fraction, β , is calculated as the ratio of integrals of background (Inner layers rotated) and signal (true position) histograms, between ± 0.04 units of $\Delta\eta$. The fraction of combinatorial background tracklets are found to be the same in data and MC for each energy up to the statistically significant OHB (Figure 35).

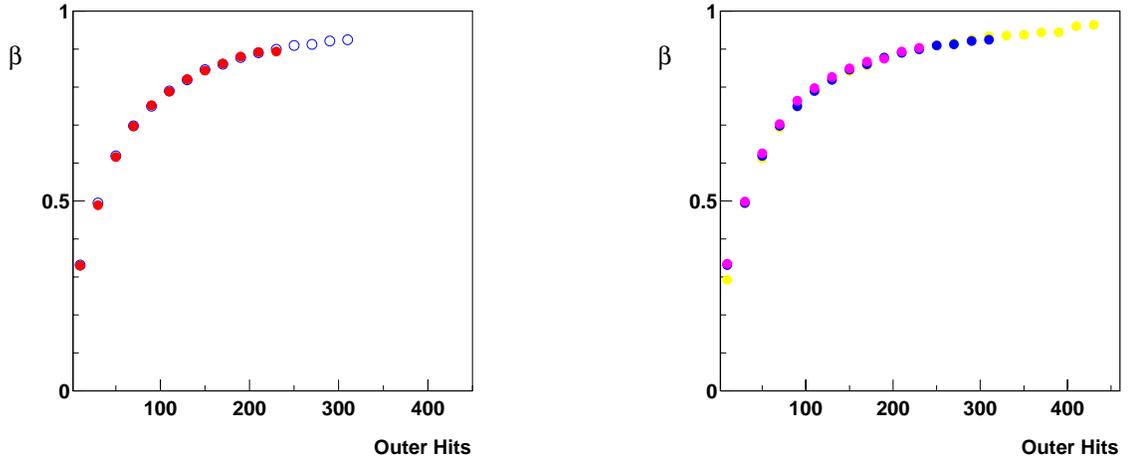


Figure 35. β versus the number of hits in the Outer Vertex. The left panel illustrates the 62.4 GeV data (blue) and MC (red). The right panel shows data for 200 (yellow), 62.4 (blue) and 19.6 GeV (purple).

The combinatorial background tracklets have to be subtracted from the total number of reconstructed tracklets for each event for data and MC, see Equation 4.3 and Equation 4.4.

$$N_{tracklets}^{Data} - N_{comb}^{Data} = N_{tracklets}^{Data} \times \left(1 - \frac{N_{comb}^{Data}}{N_{tracklets}^{Data}} \right) = N_{tracklets}^{Data} \times (1 - \beta) \quad (4.5)$$

$$N_{tracklets}^{MC} - N_{comb}^{MC} = N_{tracklets}^{MC} \times \left(1 - \frac{N_{comb}^{MC}}{N_{tracklets}^{MC}} \right) = N_{tracklets}^{MC} \times (1 - \beta) \quad (4.6)$$

Then, the term $(1 - \beta)$ in each equation will cancel out when calculating the multiplicity. Thus, explicit subtraction of the combinatorial background tracklets event by event is not necessary. This is especially helpful in 19.6 and 62.4 GeV, where the Vertex hits in HIJING MC are significantly less than in data (Figure 36). In these cases, extrapolation to higher OHB would be vital to find β . Studies performed with and without subtracting the combinatorial background yielded consistent results (see Section 4.6.1.1). Without the full subtraction, the correction factor α then has to be modified to include the combinatorial background tracklets, known as α' , see Equation 4.7 and Equation 4.8.

$$\frac{dN}{d\eta}(OHB, z_{vertex}) = \frac{N_{tracklets}^{Data}}{\alpha'} \quad (4.7)$$

$$\alpha'(OHB, z_{vertex}) = \frac{N_{tracklets}^{MC}}{N_{primaries}^{MC}} \times \Delta\eta \quad (4.8)$$

4.2.2 Acceptance and efficiency correction factor α'

The correction factor α' is derived by comparing the number of reconstructed tracklets to the number of all charged primaries in the full azimuth (and $|\Delta\eta| < 1$) for a given z -

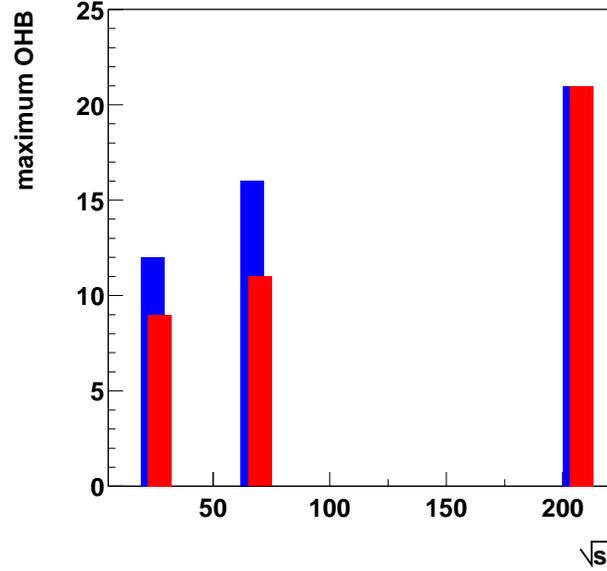


Figure 36. Maximum OHB versus energy, for data (blue) and MC (red).

vertex position and OHB, Figure 37. In this way, α' can be understood as a factor that arises primarily from geometrical considerations. α' is also affected by the intrinsic tracklet reconstruction algorithm efficiency, vertex-finder efficiency and tracklets from combinatorial and other background. The z -vertex dependence (in α') describes the geometrical acceptance of collisions away from the nominal interaction point. The multiplicity dependence (OHB) is closely connected to the tracklet finding efficiency as well the number of tracklets from secondaries and random combinations. The event vertex is restricted to ± 10 cm in z by the event selection, more details can be found in Section 3.5.

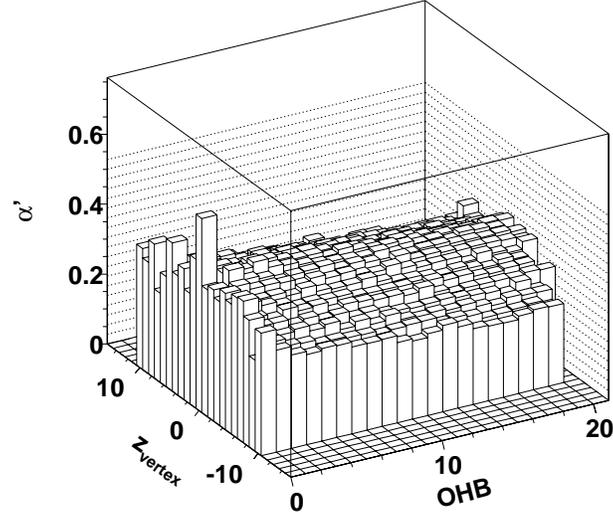


Figure 37. The α' correction factor for 200 GeV collisions.

The advantage of using the correction factor defined as above is that there is no collision energy dependence. If the MC has fewer OHB than in data, a correction obtained from higher energy simulations can be used, see the left panel of Figure 38. The correction factors also can be extrapolated to higher values of OHB, using a well defined function (e.g. first order polynomial). Both methods have been shown to give results consistent to within 1%, see Section 4.6.1.1.

4.2.2.1 Geometrical correction component in α'

The geometrical acceptance of the detector is the biggest single contribution to the correction factor. The Vertex detector acceptance in ϕ is $\approx 90^\circ$ (or 25%). The dependence of the

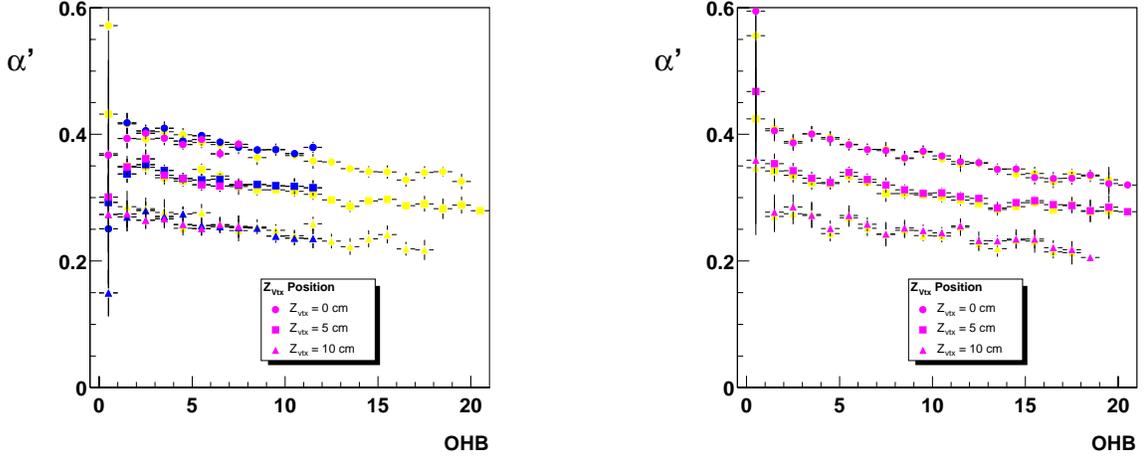


Figure 38. The left panel shows α' for all energies, 200 GeV (yellow), 62.4 (blue) and 19.6 GeV (purple). The RMSSel vertex finder is used for 200 and 62.4 GeV, SpecMain is used at 19.6 GeV. The right panel shows α' for 200 GeV with different vertex finding algorithms, RMSSelVertex (yellow) and SpecMainVertex (purple).

acceptance on z -vertex and η is shown in Figure 39. Although the geometrical acceptance can be calculated precisely, it is been folded into α' through the MC simulations. As will be shown in Section 4.6.1.1, the results with geometrical acceptance as a separate correction factor are consistent with the ones obtained with the correction α' discussed here.

4.2.2.2 Dead/Hot channel correction component in α'

When the non-working silicon channels are found and masked out in data, the reduction in the acceptance is accounted for by masking the same non-working channels in the MC. Importantly, the percentage of non-working channels is different for different datasets. Due to the radiation damage, the most recent datasets have more silicon channels masked as non-working.

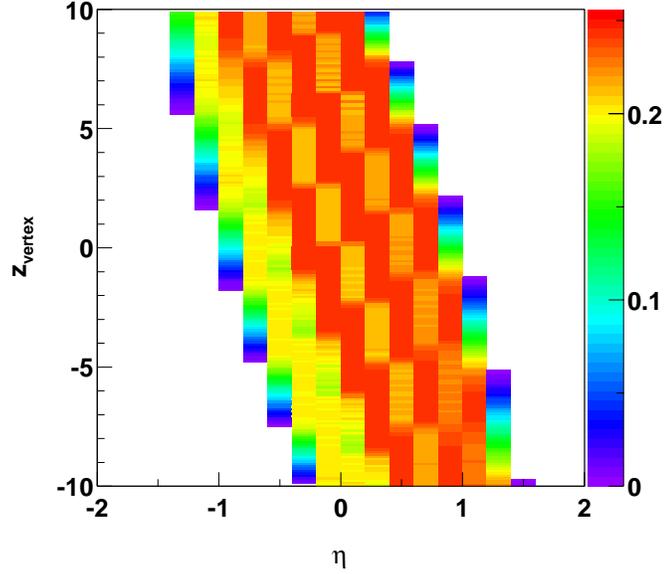


Figure 39. Acceptance in z , η for the Outer Vertex detector.

The different number of non-working channels affects α' , although this effect is small between the different years, see Table III. When a cross-check with a correction factor determined for different energy is used, the dead channel map applied to MC has to correspond to the one applied to the data.

4.2.2.3 Reconstruction efficiency component in α'

The tracklet reconstruction efficiency depends on the search method (shown in (44)) and on the intrinsic vertex finder resolution. As described in Section 3.4.1 three different vertex finders were used to obtain the multiplicity results. The vertex reconstruction efficiency and

Year	N ^o NW channels	NW channels (%)	$\langle OuterHits \rangle$ PdM>1800	$\Delta\alpha'$ (%)
no dcm	0	0	331.9 ± 1.4	0
PR01pre	401	4.9	313.5 ± 1.2	-4.7
PR01post	436	5.3	315.6 ± 1.2	-5.5
PR04	435	5.3	314.6 ± 1.0	-5.5

TABLE III

NON-WORKING (“NW”) CHANNELS FOR ALL PHOBOS DATASETS. THE KNOCK-ON EFFECT TO THE CORRECTION FACTOR ALSO SHOWN.

resolution is folded into α' . The effect of using a particular vertex finder is more obvious for the low energy or peripheral data. This will be discussed later in this Chapter. For the top 50% of the cross-section, all three vertex finders can be used resulting in the same α' correction factor. Figure 38 (right panel) shows that α' from RMSSelVertex and SpecMainVertex derive the factor to within the statistical error. It is obvious that the vertex finding efficiency can significantly reduce the data sample and one should be careful to ensure that any vertex bias applied at this level is accounted for in the associated $\langle N_{part} \rangle$ value.

4.2.3 Secondary interactions

Particles produced as a result of interactions with the beam pipe and other parts of the detector are called secondaries. This is also known as background. For example, some energetic electrons (δ -electrons) can be created when particles travel through the detector material. Thus, a tracklet could be created and reconstructed. The contamination of these tracklets is reduced to $\approx 5\%$ of the total number of tracklets due to the requirement that the tracklet points back

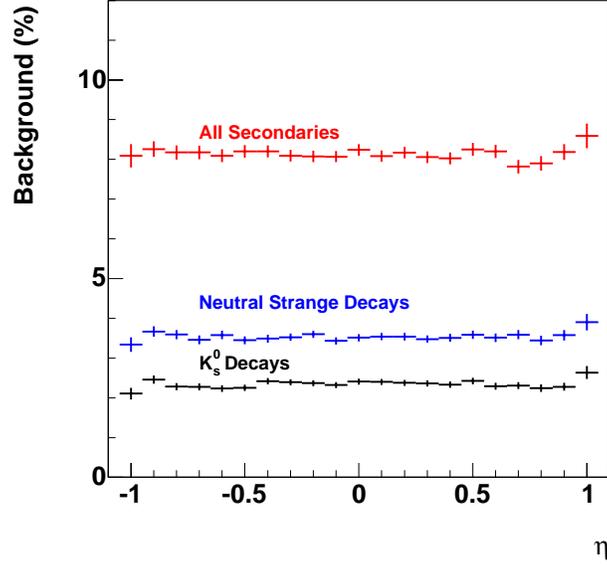


Figure 40. Percentage of all tracklets (red) which are reconstructed from secondary particles (interactions and decays). Also shown, products of all decaying neutral strange particles (blue) and K_s^0 (black) in the Vertex detector acceptance.

to the reconstructed vertex (see Figure 40). The remaining effect of these tracklets is included in the α' correction factor.

4.2.4 Decays

The number of reconstructed tracklets which are a result of decaying neutral strange particles has been studied using the HIJING event generator. Cross-checks with the VENUS (46) generator produced consistent results. Neutral particles decay in flight and produce charge particles, possibly later reconstructed as tracklets. The strange neutral particles, which have

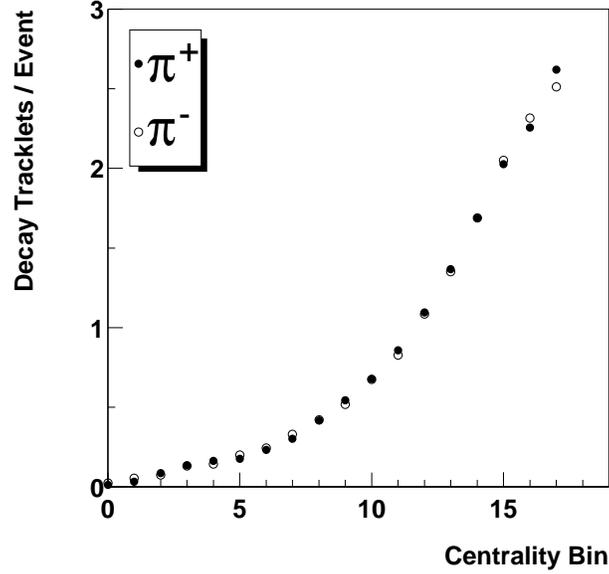


Figure 41. Reconstructed number of tracklets per event from K_s^0 decay products, 200 GeV HIJING. The centrality bin is defined from Paddle Mean.

a relatively short flight time when decaying weakly, are the largest contribution to the decay tracklets.

As an example, Figure 41 gives the number of tracklets per event from weak decay products of K_s^0 ($\langle c\tau \rangle \approx 2.7cm$) in HIJING for 200 GeV. This number increases smoothly as a function of centrality bin. The fraction of decay tracklets is found to be similar for all three energies (see Table IV), and is slightly less for central events. Studies were performed for other neutral strange (decaying) particles. Figure 40 shows that the total number of tracklets from decays

Energy	$\langle N_{tracklets} \rangle$	$\langle N_{decaytracklets} \rangle$	% contribution
200 GeV Central	312	5.7	1.8
Peripheral	64	1.2	1.9
62.4 GeV Central	174	3.2	1.8
Peripheral	44	0.8	1.8
19.6 GeV Central	130	2.1	1.6
Peripheral	34	0.6	1.8

TABLE IV

FRACTION OF WEAKLY DECAYING K_S^0 PRODUCTS (RECONSTRUCTED AS TRACKLETS) COMPARED TO THE NUMBER OF HIJING TRACKS (RECONSTRUCTED AS TRACKLETS). CENTRAL CORRESPONDS TO THE MOST CENTRAL 3% CROSS-SECTION AND MID-CENTRAL TO 35-40%).

for 200 GeV, integrated for all centralities, is $\approx 3.5\%$ for the Vertex detector acceptance, $\frac{2}{3}$ of which (2.3 %) are due to the decay of K_s^0 .

To conclude, the total (fractional) contribution from neutral strange decays is similar for all energies and does not vary as a function of multiplicity, for the most central 50% of the data. The contribution of these decay particles is corrected for by α' (they are part of the secondaries). However, there is an uncertainty of the total number of decaying particles in the event generator. This uncertainty is estimated from measurements made by other experiments and is included in the final systematic error.

4.3 Reconstruction

Applying the above tracklet reconstruction procedure to a MC sample derives the same result as the input (“Truth”) distributions of the charged particle pseudorapidity density. Figure 42 illustrates the 200 GeV MC reconstruction. The reconstruction is consistently within

2.0% . In this analysis, the data is not additionally corrected for these small point to point differences between MC truth to reconstructed MC multiplicity, known as *tweaks*, see (44). These tweaks are calculated as the difference from a MC reconstructed value for a given centrality bin to a fit to MC truth. Such an approach does not account for effects such as binning data into fractions of cross-section, errors on N_{part} , vertex efficiency effects on reconstructed tracklets (not considered in MC truth), event selection bias etc. As the tweaks could potentially lead to additional unknown uncertainties in the final result, they are not considered.

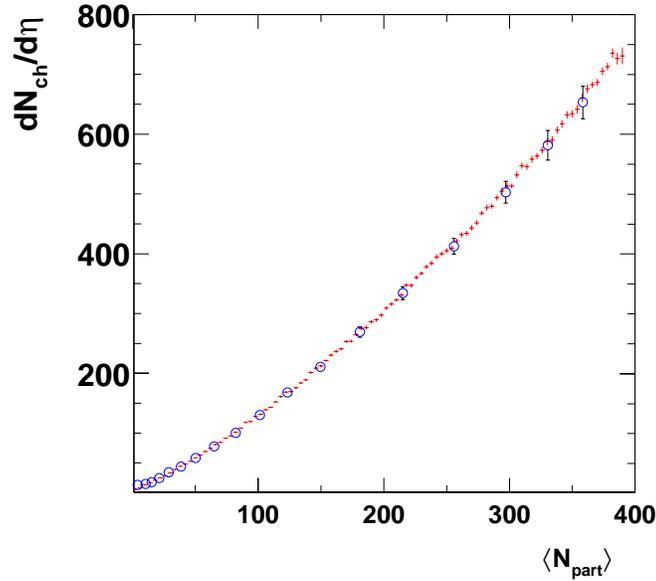


Figure 42. Truth (red symbols) and reconstructed tracklets (blue circles) in MC for 200 GeV. Errors are statistical only. The error from N_{part} is not considered.

4.4 Low centrality studies

The tracklet method described in the previous Section is used to reconstruct the multiplicity for the most central 50% of the cross-section. To progress to a more peripheral centrality region (i.e. smaller $\langle N_{part} \rangle$) where the multiplicity falls rapidly, changes to the above procedure are necessary. Specifically, the method to deduce correction factors determined for the more central data, has to be modified to account for the lower multiplicities and vertex finding resolution and efficiency. Also, further studies are required to ensure that the $\Delta\eta$ and $\Delta\phi$ residual cuts remain valid.

4.4.1 Vertex reconstruction quality

From Section 3.4.1 it can be seen that the resolution of the vertex finders deteriorate with centrality (multiplicity). An accurate vertex is essential in the tracklet reconstruction process, as this directly affects the tracklets residuals. From Figure 43, a less accurate vertex will result in the mis-calculation of the η and ϕ of a Vertex hit. The corresponding residuals will then have to be larger than the ones with a “true” vertex. From Figure 44 it can be seen that if the vertex resolution is greater than 0.2 cm the tracklet residuals will become so wide that the reconstruction process will not be reliable. The tracklet signal will be increasingly difficult to distinguish from the combinatorial background. The $\delta\eta$ cut should be widened from the current 0.04 to 0.06 units to account for a vertex resolution of 0.2 cm, see the right panel of Figure 44.

Studies of the vertex resolution for ZVertex and SpecMainVertex (at $\sqrt{s_{NN}} = 62.4$ GeV) show that these two vertex finders could be used to reconstruct low multiplicity tracklets with a maximum of 0.2 cm resolution, see Figure 20. The Vertex finder efficiency for data are also

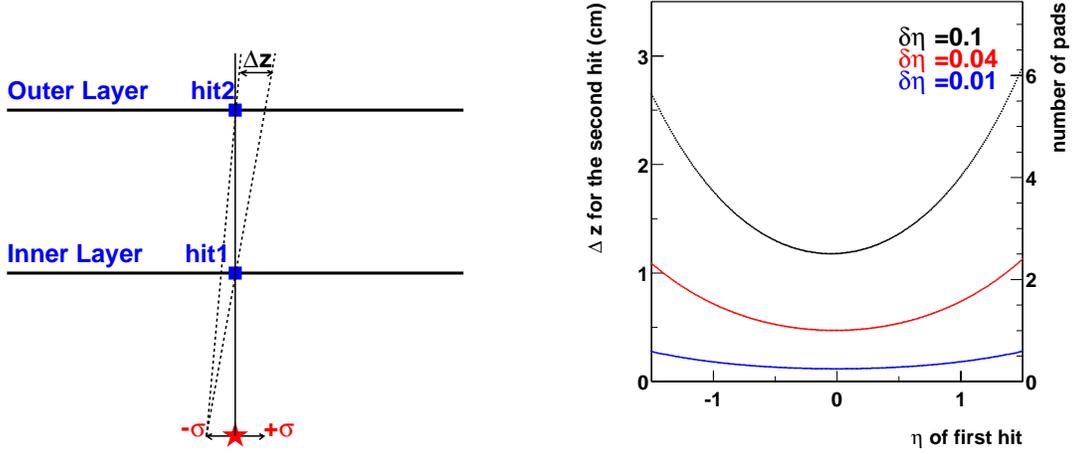


Figure 43. In the left panel, the effect of a shift in the event vertex by $1\text{-}\sigma$ on the difference in z between two hits, directly impacting the $\delta\eta$ residual. The right panel shows the maximum difference in z (or number of pads) between tracklet hits when a tracklet residual cut of $\delta\eta$ is varied. The black line illustrates the initial cut (0.1), red and blue illustrate possible final cuts applied due to analyses with different vertex resolutions. Most of the reconstructed tracklets are with residuals of 0.01 (see Figure 34).

shown in this figure. The efficiency falls dramatically below a Paddle Mean signal of ≈ 100 units, which corresponds to the top 65% of the inelastic cross-section. To counteract this decreasing effect (to improve statistics) when obtaining the global correction α some modifications were considered in the next Section.

One final note here is that for the new data ($Cu + Cu$ collisions at 200 GeV) a new vertex algorithm has become available, OneTrackVertex. This uses a single track traversing the Spectrometer or Vertex detector to find the most appropriate vertex. This has been found to have an integrated resolution of $\sigma = 0.13$ cm, which is within the 0.2 cm limit, and imposes no

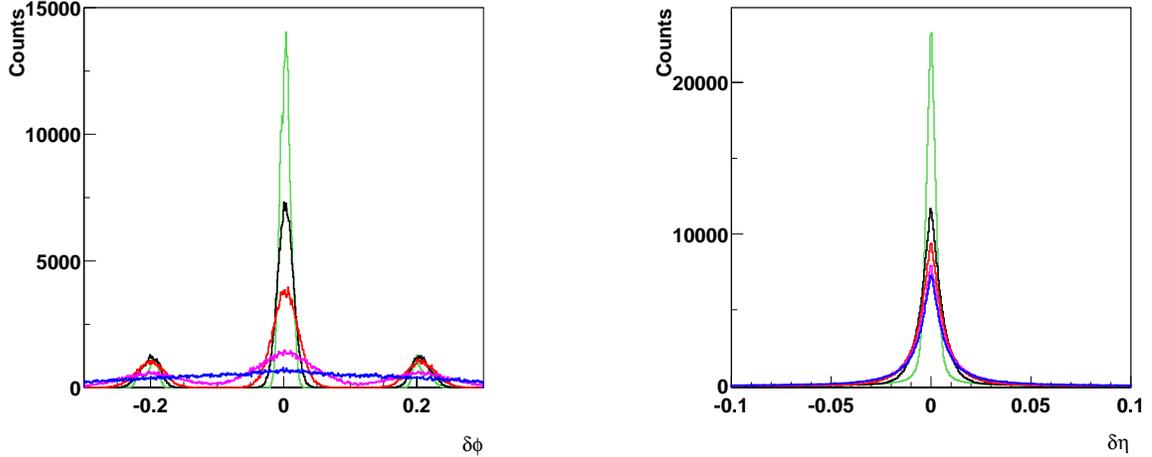


Figure 44. Effect on tracklet residuals from the vertex resolution. Vertex resolutions here are $\sigma = 0$ (true vertex (green)) 0.1 (black), 0.2 (red), 0.5 (purple) and 1cm (blue). Left figure is for the ϕ residual, right is for η .

bias on the data. This could provide the vertex for other collision systems, but is currently a work-in-progress.

4.4.2 Modifications to the α -matrix

If one subtracts the number of combinatorial background tracklets from α' (Figure 37) the correction factor α is obtained. This was originally introduced in Equation 4.4 and is shown in Figure 45. If the geometry is already accounted for in these two (α) correction factors, see Figure 46, it becomes possible to merge together all bins in z -vertex position. This will improve the statistics for the lowest multiplicity or OHB values such that fewer MC events will be needed to obtain a precise correction factor. From Figure 42, significant deviations from the

input MC are found for $\langle N_{part} \rangle < 60$, translating to $OHB \approx 3$. The improved correction factor determination allows for a more precise reconstruction in this low multiplicity environment.

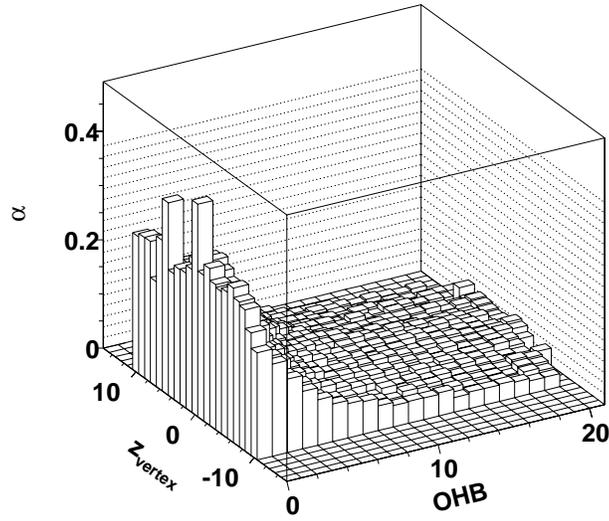


Figure 45. α correction factor (i.e. with combinatorial background subtracted). For $\sqrt{s_{NN}} = 200$ GeV MC.

4.5 Centrality overview

The collision centrality determination is performed using different data observables, both by necessity and as cross-checks. The following considerations are for the centrality determination

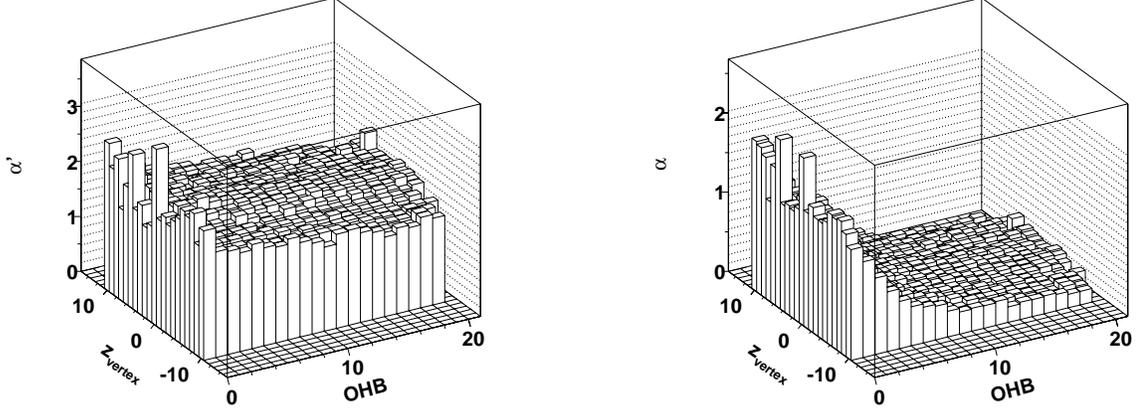


Figure 46. Correction factors with geometrical acceptance accounted for in 200 GeV MC. The left panel shows α' (combinatorial background not subtracted) and the right panel shows α (combinatorial background subtracted).

of the most central 50% of the cross-section. The centrality determination extending to the most peripheral 25% of the cross-section (≈ 20 participants) is currently under development.

4.5.1 19.6 and 200 GeV

The pseudorapidity regions used in the centrality determination for $\sqrt{s_{NN}} = 19.6$ and 200 GeV $Au + Au$ collisions are illustrated in Figure 47. The charged particle pseudorapidity distributions are shown for the top 25% of the inelastic cross-section. As described briefly in Section 3.6, the centrality determination for 200 GeV is based on the energy deposited in two scintillator Paddle counters, regions (b) in the figure. For 19.6 GeV collisions, the collision ge-

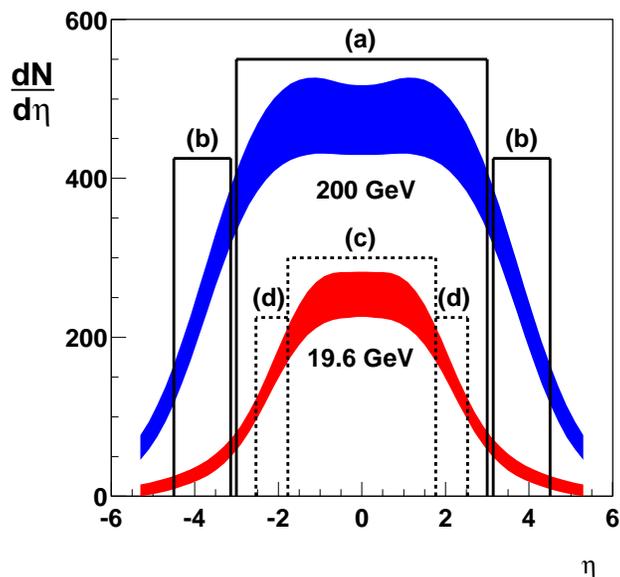


Figure 47. Pseudorapidity regions used to derive the centrality for 200 and 19.6 GeV data.

ometry was determined using a signal proportional to the number of hits in the silicon Octagon detector, region (c).

Having two different methodologies (energy deposited in a scintillator or silicon detector) at different energies to find the centrality posed questions regarding the comparison of the results obtained for these two energies. To check the importance of the details of the centrality determination on the final results, the centrality was performed in the following manner.

Two methods determining centrality away of mid-rapidity were established: regions (b), from the Paddle counters, covering $3.2 < |\eta| < 4.5$ and regions (d), from a subset of the Octagon

detector, covering $1.8 < |\eta| < 2.5$. Regions (d) are calculated as the same Paddle pseudorapidity coverage scaled by the ratio of beam rapidities ($y_{19.6}^{beam} / y_{200}^{beam} \approx 0.561$). For collisions that occur within ± 10 cm of the nominal vertex position this subset (d) lies wholly within the Octagon detector, $|\eta| < 3.2$.

Two mid-rapidity methods were also used, regions (a) and (c). Region (a) covers almost the whole Octagon ($|\eta| < 3.0$) at 200 GeV. Region (c) corresponds to a ‘reduced’ region of $|\eta| < 1.8$ at 19.6 GeV and is derived similarly to regions (d).

The centrality variables used in the above regions are referred to as Paddle Mean and EOctPaddlagon, measuring centrality away from mid-rapidity at 200 and 19.6 GeV. EOct and EOctReduced measure centrality at mid-rapidity.

The rate of increase in multiplicity is known to be different in different regions of pseudorapidity. Thus, for a given centrality measure, the dynamics of particle production could influence the final physics results if linearity with N_{part} was a prerequisite. The use of two centrality methods allows for a close examination of the necessary requirement of a monotonic dependence of the number of participating nucleons, N_{part} , and the particle multiplicity used as a centrality measure. Moreover, this tests whether linearity is a prerequisite assumption. Such an effect is not evident in this analysis. Results from both centrality methods, at both energies, were consistent to within 1%.

The standard centrality determination used for 130 and 200 GeV relied on signals from the Paddle counters. It did not deal with any additional biases but the trigger. It should be noted

that the 200 GeV Paddle based centrality, presented here, is using the same additional vertex bias requirement as imposed by the event selection for 19.6 GeV.

4.5.2 62.4 GeV

For the 62.4 GeV data, centrality methods using both the Paddles (Paddle Mean) and the Octagon (EOct), were considered. The additional vertex finding requirements were not imposed on the Paddle based centrality determination. This was borne out of the 200 GeV results analyzed with and without this restriction for the Paddle centrality method. The final results in that case were again found to be consistent.

4.6 Tracklet analysis systematic errors

The systematic errors are presented in two parts. Errors on the individual energy measurements and errors on the ratio of two energies.

4.6.1 Individual measurement

The initial estimate for the systematic errors on the individual tracklet measurements for 130 GeV data is described in detail in (44). For this reason, only a brief description of the studies which lead to the final error of 7.5% (90% C.L.) will follow. The same studies as for the 130 GeV were performed for all energies. Due to the similarity between them, some illustrations only for the 62.4 GeV dataset will be shown, see Appendix D. More information about how to estimate the systematic errors in a general physics analysis can be found in (47; 48). There is no evidence for additional sources of uncertainty, which could lead to different systematic errors for any of the analyzed data. There are four main contributions to these systematic errors.

4.6.1.1 Tracklet reconstruction uncertainty

The tracklet reconstruction error is estimated by varying some of the chosen conditions imposed in the reconstruction analysis. The effect on the final result from changing the Search Method, performing the analysis in a subset of the detector, changing the z -vertex range or hit and tracklet energy cuts were studied.

As ultimately no difference is observed, no error is assigned for using either the Search Inner or Search Outer method, with the two-pass condition. The effects from dividing the z -vertex range into four reduced regions of 5 cm are small. The error here is dominated by statistics and the deviation is within 1%. Reconstructing the tracklets independently in either the Top or Bottom Vertex detector depends on the y -beam position. This uncertainty is found to be $\approx 1\%$ for $y \approx 0$ cm. The initial energy cuts applied to the Detector hits during the merging procedure can be also varied. No difference is observed for cuts of up to 90% of the mean MIP position and no systematic error is assigned for this.

Changing the cut on the average tracklet energy (obtained from average of the two Vertex hits) leads to no systematic effect. The final systematic error from tracklet reconstruction is estimated to be a total of 1.8%.

4.6.1.2 Real and combinatorial background

The effect of real background from secondaries (due to interactions with material in the detector) was studied in (44). Lowering the initial energy cuts for gammas and electrons in GEANT (from 1000 keV to 125 keV and 25 keV) produces more background. This does not

affect the tracklet results down to the 125 keV level. As no deviation is observed above 125 keV, there is only a 1% uncertainty assigned from this source.

Combinatorial background effects were studied with and without explicit subtraction of the combinatorial background tracklets. This leads to no additional error.

4.6.1.3 Weak decays

The yield of weakly decaying particles is distinct for different generators. $K_s^0(u\bar{s})$ is found to have the largest contribution to the number of reconstructed tracklets in MC ($\sim 2\%$ for all energies, see Section 4.2.4). The dN/dy of K_s^0 decaying particles at mid-rapidity are measured by other experiments for the top 6% of the cross-section at 130 and 17.2 GeV, see (49). The weak decays are corrected for by α' . If the measurements are larger/smaller than those generated by HIJING (with a similar cross-section of 10% and rapidity range), there will be more weak decays in data than are accounted for in the correction factor.

At 200 GeV the K_s^0 yield is found to be the same in data ($dN/dy = 37 \pm 2$)¹ and MC ($dN/dy \sim 35$) within the error of the measurement. Because the data is at a lower energy than MC, this could translate to no additional error from weak decays or a to maximum shift down by 1% for the final result at 200 GeV. Previously, a 2% uncertainty had been assigned from weak decays. The results for 17.2 GeV are from NA47 and NA49 experiments and they differ by 30% ($dN/dy \approx 27 \pm 2$ and 8 ± 2 respectively). As the measured yield is approximately twice (higher or lower) to that found in HIJING (for 19.6 GeV and 10% central MC sample

¹Data at lower energy of 130 GeV and slightly more central than MC to account for this difference.

$dN/dy = 13.5 \pm 1.8$), the assigned error corresponds to the fraction of these products relative to the total tracklets as reconstructed in MC, refer to Table IV. The systematic uncertainty on the measurement from weakly decaying particles is 2% for 19.6 GeV, assigned from this analysis, and the same for 200 GeV, assigned from prior analysis and retained here for consistency.

4.6.1.4 MC generators

Errors from using different MC generators (HIJING, VENUS, RQMD) were first evaluated as a function of centrality ($\langle N_{part} \rangle$) for the first RHIC run of 130 GeV. However, when the studies were performed again recently for the 200 GeV analysis, the previously found deviation between the final results using HIJING and VENUS was not observed. This deviation was the main contribution to the 5% systematic error assigned from MC generators for the early PHOBOS results (50). The over-estimation made before could be due to using the $\langle N_{part} \rangle$ and centrality bins derived from one generator and applying them to the other. There were no centrality studies performed with RQMD for other energies. Because the systematic effects from using different generators were not performed for all energies the 5% error from MC generators was retained for current data, although this could represent an over-estimation.

4.6.1.5 Additional errors

The results for each energy are plotted as a function of (and scaled by) $\langle N_{part} \rangle$, which has its own systematic error. The main considerations for additional errors from $\langle N_{part} \rangle$ on the scaled result in $Au + Au$ collisions are similar to those in $d + Au$. An outline of my work on this subject is described in more detail in Appendix F.

The nucleon-nucleon cross-section (σ_{NN}) used in HIJING calculations is a source of systematic uncertainty. The inelastic cross-sections are calculated from the published total and elastic cross-sections. These are known to better than 1 mb (i.e. $< 3\%$ uncertainty). A Glauber MC is used to calculate the slope of N_{part} versus σ_{NN} . The effects are small and are difficult to separate from statistical effects.

The error on $\langle N_{part} \rangle$ includes uncertainties from MC simulations of the detector response¹ as well as Glauber Model calculations. Studies were performed using a Glauber model with various smearing functions, to mimic different detector responses and different dependences of the centrality variable with N_{part} (the exact monotonic dependence may be different in data from that given in various particle production models).

An additional possible source of systematic mistake is from the determination of N_{part} for each bin, which do not arise from the inelastic cross-section input in Glauber. The accuracy of the percentile of cross-section bin cut positions, associated with the trigger efficiency, should be part of the error on the number of reconstructed tracklets. This effect is centrality dependent and rises smoothly from central to mid-central events, Figure 48. More discussion of this error is left for Section 4.6.2.3.

The total systematic biases arising from $\langle N_{part} \rangle$ have been estimated and are of the order 3% (central) to 9% (peripheral) for each energy.

¹Paddles or Octagon used for the centrality determination

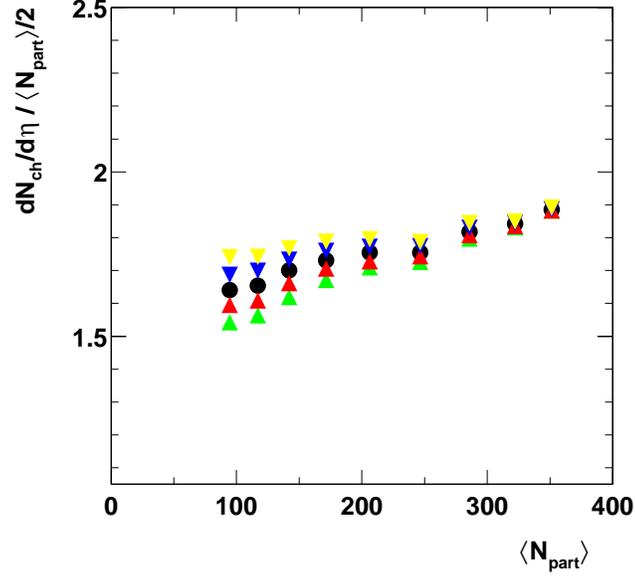


Figure 48. Effect on multiplicity from the uncertainty in the trigger efficiency (ϵ) for $\sqrt{s_{NN}} = 19.6$ GeV data. The black symbols represent the nominal efficiency $\epsilon = 55.4\%$. The other colored symbols represent systematic shifts in the efficiency: yellow $\epsilon + 2$, blue $\epsilon + 1$, red $\epsilon - 1$ and green $\epsilon - 2$.

4.6.2 Ratio of two datasets

Most of the errors on the individual measurement cancel when taking the ratio. The reason for this is due to the analysis being performed with the same method (Vertex tracklets), for the same detector and carefully matched centrality determination. Errors on the ratio are calculated as the combined $1\text{-}\sigma$ statistical and systematic errors. The following discussion is for the ratio of 200/19.6 GeV, but similar considerations are valid for ratios of all datasets.

Assuming that the contributing errors to the final uncertainty on the ratio are not correlated, the fractional error on the ratio can be presented as Equation 4.9, where the fractional errors of type $\delta R_x/R_x$ are denoted as R_x .

$$R = \sqrt{R_\alpha^2 + R_{\beta_{200\text{GeV}}}^2 + R_{\beta_{19.6\text{GeV}}}^2 + R_{N_{rec}}^2 + R_{N_{part}}^2} \quad (4.9)$$

Five factors (components) contribute to the final error on the ratio:

1. R_α - uncertainty due to the overall acceptance and efficiency of the detector.
2. $R_{\beta_{200\text{GeV}}}$ - systematic error from the combinatorial background in data and MC for a given energy (for 200 GeV).
3. $R_{\beta_{19.6\text{GeV}}}$ - systematic error from the combinatorial background in data and MC for a given energy (for 19.6 GeV).
4. $R_{N_{rec}}$ - Systematic and statistical uncertainties from tracklet reconstruction (counting).
 - (a) r_{stat} - Direct counting statistics.
 - (b) $r_{TrigEff}$ - Uncertainty from the estimation of the overall detector triggering efficiency
5. $R_{N_{part}}$ - Uncertainty in the N_{part} estimation.

4.6.2.1 R_α

R_α has two main contributions: the overall acceptance of the Vertex detector and the tracklet finding efficiency. The geometrical portion of α' (Section 4.2.2) will cancel precisely. Geometrical acceptances for the two datasets are identical as the data were taken back-to-back

with the same apparatus and overall beam conditions. Any other effects that arise solely from the z -vertex position will also cancel, since the ratios were performed for data restricted to the same z -vertex range. The multiplicity portion of α' is also independent of the collision energy in the overlap OHB region. This was verified both by comparison of α' at all energies (Figure 38, right panel) as well as performing a data check by comparing 19.6 GeV results analyzed using the efficiency correction factors for 200 and 19.6 GeV (similar checks done for 62.4 GeV). The largest difference found did not exceed 1%. Thus the maximum centrality independent systematic uncertainty in the ratio is estimated to be 1%. This is strictly a 90% C.L. error, but it was conservatively put as $1\text{-}\sigma$. The efficiency correction factors at two different collision energies do not overlap for higher OHB (multiplicity). Because the data is analyzed in percentile bins of cross-section, not OHB, the ratio of the correction factors may have a portion which doesn't cancel. This potential systematic effect for central events at the higher of the two energies can be a consequence of the incorrectly determined combinatorial background tracklets or tracklets from secondaries (weak decays). The combinatorial background tracklets can be measured in data and MC and they are found to have no effect on the final results (see Section 4.6.2.2). The background from secondaries due to interactions with surrounding material behaves as the geometrical efficiency and will cancel in the ratio.

The contribution from secondaries was presented in Section 4.2.3. If no correction for weak decays to the number of reconstructed tracklets is performed, this could lead to a correlated systematic effect of less than 1%. Because the correction is already done in MC, this relies entirely on MC predicting the background correctly for both energies. As discussed in Sec-

tion 4.6.1.3, there is uncertainty in HIJING to determine the K_s^0 yields, which could be about half of that observed in data for 19.6 GeV.

Thus, the initial effect of 1% (was doubled and) is estimated to be 2% due to a possible systematic mistake for which the bias cannot be appropriately accounted for. R_α is estimated to be a total of 2%.

4.6.2.2 $\underline{R_\beta}$

The combinatorial background in data was found to be the same at both energies and it matched the combinatorial background in MC extremely well (as in Section 4.2.1). α' includes the background fraction that has been conservatively estimated for above. When individual results were obtained with α , the results were consistent. Any remaining correlated systematic mistake should cancel in the ratio . The main contribution here comes from the uncertainty in the measured y -position of the collision vertex. It is due to both vertex-finding and MC geometry (detector alignment) uncertainties. If this uncertainty is conservatively put at 1 mm, this translates to 0.4% shift in the reconstructed yield, part of which could be due to the background subtraction. Thus the uncertainty on the ratio from combinatorial background subtraction was estimated as $R_\beta = 0.4\%$ for each energy. Another possible source of systematic uncertainty could arise from the offset of the vertex position in data for 19.6 GeV, which is not present in 200 GeV. This will be discussed in Section 4.6.2.4.

4.6.2.3 $\underline{R_{N_{rec}}}$

$R_{N_{rec}}$ is estimated to be 2.2% on the ratio for the most central bin. The efficiency of finding tracklets is included in the correction factor α' . The remaining considerations on the error on

the ratio from the tracklet reconstruction include: the direct counting statistics (r_{stat}), accuracy of the percentile of cross-section bin cut positions ($r_{TrigEff}$), any possible additional biases in data that could affect the number of reconstructed tracklets in one of the two datasets.

The statistical uncertainty on the ratio is event based and includes the statistical error from both data and MC samples. These are propagated through the full calculation of $dN/d\eta/(\langle N_{part} \rangle/2)$ at each energy. This error was found to be almost independent of centrality for the considered part of cross-section and depends on the size of the data and MC sample used at each energy.

$$r_{stat} = \sqrt{\left(\frac{\delta N_{stat}^{200}}{N_{stat}^{200}}\right)^2 + \left(\frac{\delta N_{stat}^{19.6}}{N_{stat}^{19.6}}\right)^2} = \sqrt{0.02^2 + 0.01^2} = 0.022 \quad (4.10)$$

Another uncertainty comes from the estimation of the trigger efficiency, which has a cumulative effect as one moves from central to mid-central collisions. $r_{TrigEff}$ is therefore a strongly centrality dependent factor, varying smoothly from 0% for the most central collisions to 6% for the mid-central. To determine the magnitude of this, the trigger efficiency value was varied by the estimated 3% relative error from the PHOBOS minimum bias trigger efficiency (actually is 90% C.L.) and the data was reanalyzed. Figure 48 illustrates the effect of the trigger efficiency on the individual energy result. This error is then calculated as Equation 4.11.

$$r_{TrigEff} = \sqrt{\left(\frac{dR_{200/19.6}}{de}\right)^2 \left(\frac{de}{R_{200/19.6}}\right)^2} \quad (4.11)$$

There are two limits that can be considered. A low limit comes from a fully “correlated” efficiency, when the assumption is made that the trigger efficiency values are systematically higher or lower by 3% for both energies. The upper limit comes from a fully “uncorrelated” situation, when the trigger efficiency for one of the energies is systematically higher by 3% and respectively systematically lower by the same amount for the other energy. The expectation is that the efficiencies will be strongly correlated due to the fact that this is the same detector and trigger used for all energies. However, considering that the efficiency estimation and centrality determination methods are slightly different for 200 and 19.6 GeV (Paddle hit method and EOct shape matching) possible uncorrelated effects cannot be ruled out. After careful consideration, the assigned values for the error were chosen to reflect the possibility that the efficiency could be partially uncorrelated.

The known offset of 5 mm in the y -position of the beam orbit for 19.6 GeV is the remaining possible source for systematic error in the number of tracklets for the two energies. The beam offset changes the geometrical acceptance of the Top and Bottom Vertex detectors. This known bias was considered in two different ways. The systematic bias is minimized in the analysis because the number of reconstructed tracklets is an average of the number of tracklets in the Top and Bottom Vertex. If no corrections were done, using geometrical considerations, we obtain that a shift of $\delta y = 0.5$ cm in the y -vertex position will correspond to a maximum uncorrected percentage shift in the reconstructed yield at one energy of 3%.

$$Shift(\%) = \frac{r_0^2}{2} \left(\frac{1}{(r_0 + \delta y)^2} + \frac{1}{(r_0 - \delta y)^2} \right) - 1 \quad (4.12)$$

where $r_0 = 5$ cm is the distance from the nominal vertex position to the Inner Vertex detector. Additionally, the data was analyzed using MC with and without this beam orbit offset, resulting in a 2% systematic difference for the ratio of the final multiplicities. This value is very close to the simple geometrical considerations above. Since this bias is known, understood and corrected for in the analysis, no additional error to the $R_{N_{rec}}$ is assigned from this source.

4.6.2.4 $R_{N_{part}}$

$R_{N_{part}}$ includes uncertainties from MC simulations of the detector response as well as Glauber Model calculations. The considerations for the individual measurement were described above.

$$R_\sigma = \sqrt{\left(\frac{dN_{part}^{200}}{d\sigma^{200}}\right)^2 \left(\frac{d\sigma^{200}}{N_{part}^{200}}\right)^2 + \left(\frac{dN_{part}^{19.6}}{d\sigma^{19.6}}\right)^2 \left(\frac{d\sigma^{19.6}}{N_{part}^{19.6}}\right)^2} \quad (4.13)$$

A Glauber MC is used to calculate the slopes of N_{part} versus σ_{NN} . The effects from the uncertainty in the nucleon-nucleon cross-section in Glauber are distinguishable for a variation of 2 mb (although it is known to better than 1 mb) for each energy. This leads to an average value of 0.4% in the ratio.

All systematic effects due to detector smearing should cancel in the ratio, as the same detector (Octagon or Paddles) was used for centrality determination. If the smearing effects were to have a large effect, the ratios using results from different centrality variables (EOct and Paddles) would not agree, an effect not apparent in the data. The individual systematic biases have been calculated and are of order 3-9% as a function of centrality for each energy. Traditionally, this error is considered together with the uncertainty in the detector efficiency

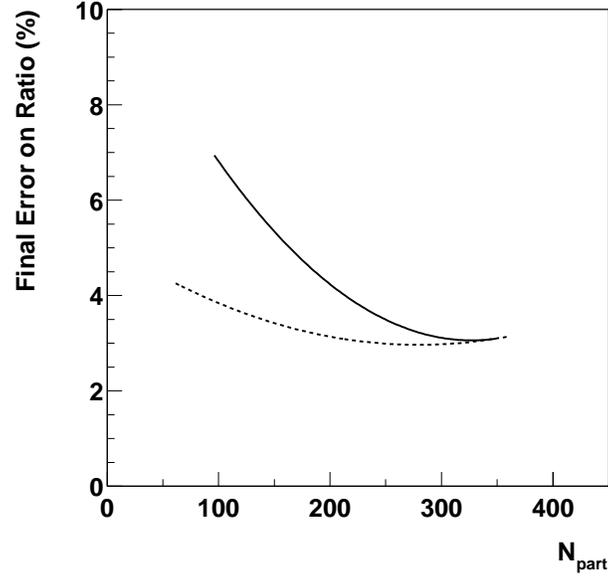


Figure 49. Final error on the ratio of tracklets results for 200/19.6 (solid line) and 200/62.4 GeV(dashed line) as a function of N_{part} .

and centrality bin determination. The remaining effects should cancel in the ratio, leaving only an error of 0.4% from the uncertainty in the measured σ_{NN} .

4.6.2.5 Final error on the ratio

The final, 1- σ , combined systematic and statistical error on the ratio for the two datasets are centrality dependent (see Figure 49). The contribution of the different factors are presented in Table V. By adding all factors, described above, in quadrature, the final error is 3% for central and 7% for mid-central events.

contribution to the final error on ratio	value(%) 200/19.6 GeV	value(%) 200/62.4 GeV
R_α	2.0	2.0
$R_{\beta_{200\text{GeV}}}$	0.4	0.4
$R_{\beta_{19.6(62.4)\text{GeV}}}$	0.4	0.4
$R_{Nrec}(r_{stat})$	2.2	2.0
$R_{Nrec}(r_{TrigEff})$	0.0/6.0 (*)	0.0/3.0 (*)
R_{Npart}	0.4	0.4
total	3.1/6.7 (*)	2.9/4.2 (*)

TABLE V

CONTRIBUTION TO THE FINAL ERROR ON THE RATIO FOR 200/19.6 AND 200/62.4 GEV. (*) SHOWN FOR CENTRAL/MID-CENTRAL DATA.

4.6.2.6 Final error on the ratio for 200/62.4 GeV

The final error on the ratio (52) (for mid-central collisions) is lower compared to that of the 200/19.6 GeV case, entirely due to the determination of the $r_{TrigEff}$ uncertainty. The trigger efficiency values for 200 and 62.4 GeV are assumed to be fully “correlated”, using either EOct or Paddle based centrality determination, and the same method for estimating the trigger efficiency. The final error on the ratio, shown in Table V and Figure 49 as a dashed line, is 3% for central and 4% for mid-central events.

CHAPTER 5

RESULTS FROM MID-RAPIDITY CHARGED PARTICLE MULTIPLICITY MEASUREMENTS

The results from the mid-rapidity multiplicity Tracklet analysis at $\sqrt{s_{NN}} = 200, 19.6$ and 62.4 GeV are presented in two parts. In the first part the results for the individual measurements for the top 50% of the cross-section are shown for various centrality determinations. Also, the ratio of these data are shown with respect to the 200 GeV dataset.

In the second part, results for the energy density using the Bjorken estimate are presented for all considered energies.

5.1 Results for individual energy measurements, 0-50% most central data

Experimental results are presented for the charged particle multiplicity, $dN/d\eta$, and also collision geometry scaled, $dN/d\eta/\langle N_{part} \rangle/2$, both as a function of $\langle N_{part} \rangle$. Two different centrality determinations are used, either based on information from the Octagon detector (EOct centralities) or the Paddle counters (Paddle Mean centralities). Collisions representing only the top 50% of the inelastic cross-section are considered, except for the 19.6 GeV, which is shown for the top 40%. The details of the centrality determinations have already been described in Sections 3.6 and 4.5. The error presentation as ellipses is based on work from B.Back and an elegant description and derivation from M.Baker can be found in D.

5.1.1 Centrality dependence for 200 GeV

The Paddle Mean centrality determination for this work is modified compared to the one initially published in (51). The same vertex restrictions as in 19.6 GeV were applied to 200 GeV data to allow for a better comparison between the two datasets. The same vertex restriction is always used for all Octagon based centrality determinations (Section 3.6.2).

The data results for charged particle pseudorapidity density for two centralities are presented in Figure 50 and all values are collated in Table VI.

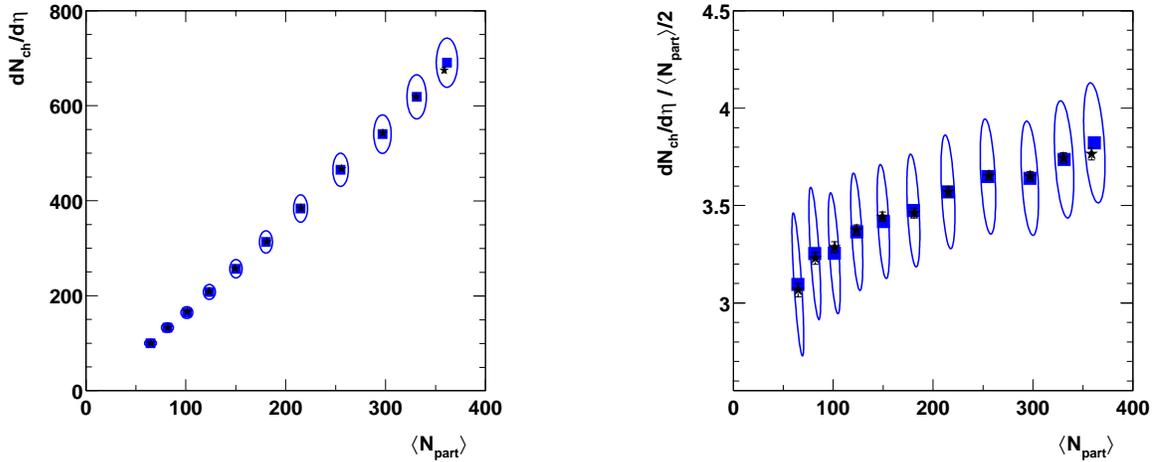


Figure 50. Results for charged particle multiplicity as a function of centrality for $\sqrt{s_{NN}} = 200$ GeV Au+Au. Square (star) symbols correspond to the EOct (Paddle Mean) centrality determination. The right panel shows the results scaled by the number of participant pairs.

Bin (%)	EOct			Paddle Mean		
	$dN_{ch}/d\eta$	$\langle N_{part} \rangle$	$\frac{dN_{ch}/d\eta}{\langle N_{part} \rangle/2}$	$dN_{ch}/d\eta$	$\langle N_{part} \rangle$	$\frac{dN_{ch}/d\eta}{\langle N_{part} \rangle/2}$
0-3	691±52	361±11	3.82±0.31	675±51	359±11	3.77 ±0.31
3-6	619±46	331±10	3.74±0.30	619±46	330±10	3.74±0.30
6-10	540±41	297±9	3.64±0.30	542±41	297±9	3.65± 0.30
10-15	465±35	255±8	3.65±0.30	467±35	256±8	3.65 ±0.30
15-20	384±29	215±7	3.57±0.29	384±29	215±7	3.57 ±0.29
20-25	313±24	180±7	3.47±0.30	313±23	181±7	3.46±0.29
25-30	257±19	150±6	3.42±0.29	257±19	149±6	3.44 ±0.29
30-35	208±16	124±6	3.37±0.30	208±16	123±6	3.37±0.31
35-40	165±12	101±6	3.25±0.31	166±12	101±6	3.29±0.31
40-45	133±10	82±6	3.25±0.34	132±10	82±6	3.23±0.34
45-50	100±8	65±6	3.10±0.38	100±8	65±6	3.07±0.38

TABLE VI

EXPERIMENTAL RESULTS FOR THE CHARGED PARTICLE PSEUDORAPIDITY DENSITY AT 200 GEV FOR TWO CENTRALITY DETERMINATIONS. THE MOST CENTRAL COLLISIONS ARE LABELED AS BIN 0-3%. ERRORS REPRESENT 90% C.L. SYSTEMATIC LIMITS.

The two centrality determinations lead to the same values of $dN_{ch}/d\eta$ for equivalent percentile of cross-section bin within the presented systematic errors. The largest difference in the mean values of the charged particle multiplicity and $\langle N_{part} \rangle$ is observed for the 3% most central collisions. The $\langle N_{part} \rangle$ for the Octagon based centrality, which uses a signal from mid-rapidity, is higher than that obtained from the Paddle counters (away from mid-rapidity). This is due to fluctuations in the centrality variable distributions EOct and Paddle Mean, which are largest for the most central data. The changes in $dN_{ch}/d\eta$ for the most central bin follow the changes observed in $\langle N_{part} \rangle$ from MC studies.

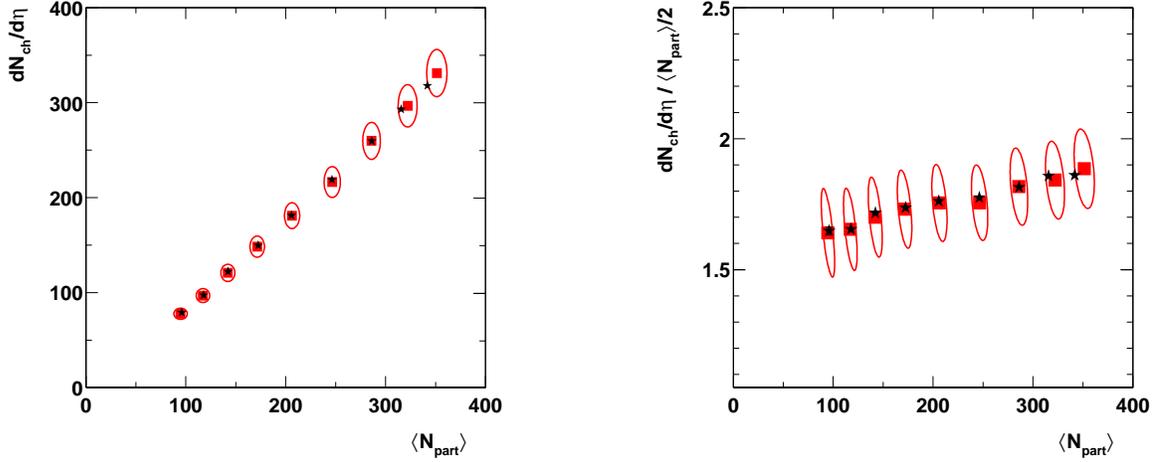


Figure 51. Results for charged particle multiplicity as a function of centrality for $\sqrt{s_{NN}} = 19.6$ GeV Au+Au. Square (star) symbols correspond to the EOctRed (EOctPdlgon) centrality determination. The right panel shows the results scaled by the number of participant pairs.

5.1.2 Centrality dependence for 19.6 GeV

The two centrality variables for 19.6 GeV are determined using the Octagon detector. As described in Section 4.5, EOctRed and EOctPaddlgon are chosen in order to be comparable centrality variables to those of 200 GeV. The data results (Table VII), shown in Figure 51, are equivalent within the systematic errors. Again, the major difference between the two centrality determinations is observed for the most central values of the charged particle multiplicity and $\langle N_{part} \rangle$. The mid-rapidity centrality determination, EOctRed, has a higher $\langle N_{part} \rangle$ values for the top 6% and 3% bins, compared to only the top 3% for 200 GeV.

Bin(%)	EOctRed			EOctPdlgon		
	$dN_{ch}/d\eta$	$\langle N_{part} \rangle$	$\frac{dN_{ch}/d\eta}{\langle N_{part} \rangle/2}$	$dN_{ch}/d\eta$	$\langle N_{part} \rangle$	$\frac{dN_{ch}/d\eta}{\langle N_{part} \rangle/2}$
0 3	331±24	351±11	1.89±0.15	318±24	342±11	1.86±0.15
3 6	297±22	322±10	1.84±0.15	293±22	315±10	1.86± 0.15
6 10	260±20	286±9	1.82±0.15	260±20	286±9	1.81±0.15
10 15	216±16	247±8	1.76±0.14	219±16	246±8	1.76±0.14
15 20	181±14	206±8	1.75±0.15	181±14	206±8	1.76±0.15
20 25	148±11	171±7	1.73±0.15	150±11	173±7	1.74±0.15
25 30	121± 9	142±7	1.70±0.15	122± 9	142±7	1.72±0.15
30 35	97± 7	117±7	1.65±0.16	97± 7	118±7	1.65±0.15
35 40	78± 6	95±7	1.64±0.17	79± 6	96±7	1.65±0.17

TABLE VII

EXPERIMENTAL RESULTS FOR THE CHARGED PARTICLE PSEUDORAPIDITY DENSITY AT 19.6 GEV FOR TWO CENTRALITY DETERMINATIONS. THE MOST CENTRAL COLLISIONS ARE LABELED AS BIN 0-3%. ERRORS REPRESENT 90% C.L. SYSTEMATIC LIMITS.

5.1.3 Centrality dependence for 62.4 GeV

For the results here (52), Paddle centrality determination is performed without additional vertex restrictions. The full EOct from the Octagon detector was also used to obtain the results, see Table VIII. The results are the same within the systematic errors. As in the other datasets, the largest deviations are seen for the most central data, in this case, only for the top 3% of the cross-section. Results are shown in Figure 52. Slight deviations in the mid-central region could be due to not applying the more restrictive vertex selection (Section 3.6.2) for the Paddle based centrality determination used here.

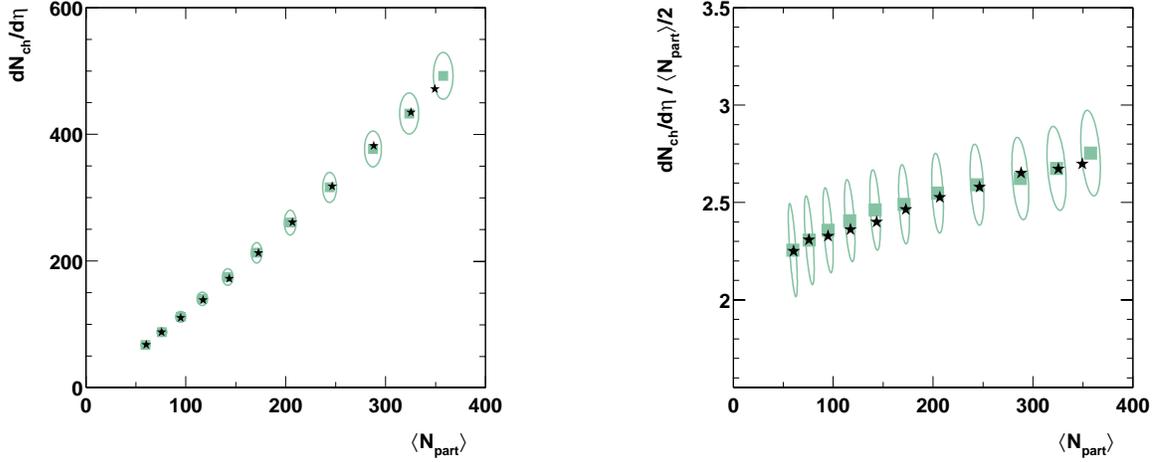


Figure 52. Results for charged particle multiplicity as a function of centrality for $\sqrt{s_{NN}} = 62.4$ GeV Au+Au. Square (star) symbols correspond to the EOct (Paddle Mean) centrality determination. The right panel shows the results scaled by the number of participant pairs.

5.2 Results for ratio measurements, 0-50% most central data

In this Section, the ratios for the geometry scaled charged particle multiplicity as a function of $\langle N_{part} \rangle$ for 200 GeV with respect to 19.6 and 62.4 GeV for equivalent centrality determinations (EOct and Paddles) are presented. The ratio with 19.6 GeV is considered for the top 40% of the cross-section, 200/62.4 is for the top 50%.

5.2.1 Ratio 200/19.6 GeV

The ratio for the 200 and 19.6 GeV with EOct and EOctRed methods is shown on Figure 53. For the same fixed fraction of cross-section $\langle N_{part} \rangle$ is different for the two energies. For this reason, the ratio was calculated in two distinct ways. First, the result presented with closed

Bin(%)	EOct			Paddle Mean		
	$dN_{ch}/d\eta$	$\langle N_{part} \rangle$	$\frac{dN_{ch}/d\eta}{\langle N_{part} \rangle/2}$	$dN_{ch}/d\eta$	$\langle N_{part} \rangle$	$\frac{dN_{ch}/d\eta}{\langle N_{part} \rangle/2}$
0 3	492±37	358±11	2.75±0.22	471±35	349±11	2.70±0.22
3 6	433±32	324±10	2.68±0.21	435±33	325±10	2.67±0.21
6 10	377±28	287±8	2.62±0.21	382±29	288±8	2.65±0.21
10 15	316±24	244±6	2.59±0.21	318±24	247±6	2.58± 0.20
15 20	261±20	205±6	2.55±0.21	261±20	207±6	2.53±0.21
20 25	213±16	171±6	2.49±0.21	213±16	173±6	2.46 ±0.20
25 30	175±13	142±6	2.46±0.21	172±13	144±6	2.40±0.21
30 35	140±11	116±6	2.41±0.23	138±10	117±6	2.36±0.21
35 40	112± 8	95±5	2.36±0.21	110± 8	95±5	2.33±0.21
40 45	88± 7	76±5	2.31±0.24	87± 7	76±5	2.31±0.24
45 50	67± 5	60±4	2.26± 0.23	68± 5	60±4	2.25±0.22

TABLE VIII

EXPERIMENTAL RESULTS FOR THE CHARGED PARTICLE PSEUDORAPIDITY DENSITY AT 62.4 GEV FOR TWO CENTRALITY DETERMINATIONS. THE MOST CENTRAL COLLISIONS ARE LABELED AS BIN 0-3%. ERRORS REPRESENT 90% C.L. SYSTEMATIC LIMITS.

squares in Figure 53, is obtained by averaging the individual $\langle N_{part} \rangle$ values. Second, the ratio with open squares is formed by completely reanalyzing the data with a new centrality determination method, which varies the percentile of cross-section bin width in an iterative fashion in order to ensure the same, fixed $\langle N_{part} \rangle$, for the two energies. These two ways of performing the ratio yield consistent results and show no systematic effect due to the specific $\langle N_{part} \rangle$ determination between energies. Furthermore, the slopes for both ratios are consistent with zero within the errors, showing no centrality dependence on the ratio $R_{200/19.6}$ for the top 40% of the inelastic cross-section. The most probable mean value found for the fixed cross-section method is $R_{200/19.6} = 2.03 \pm 0.02 \pm 0.05$ (53).

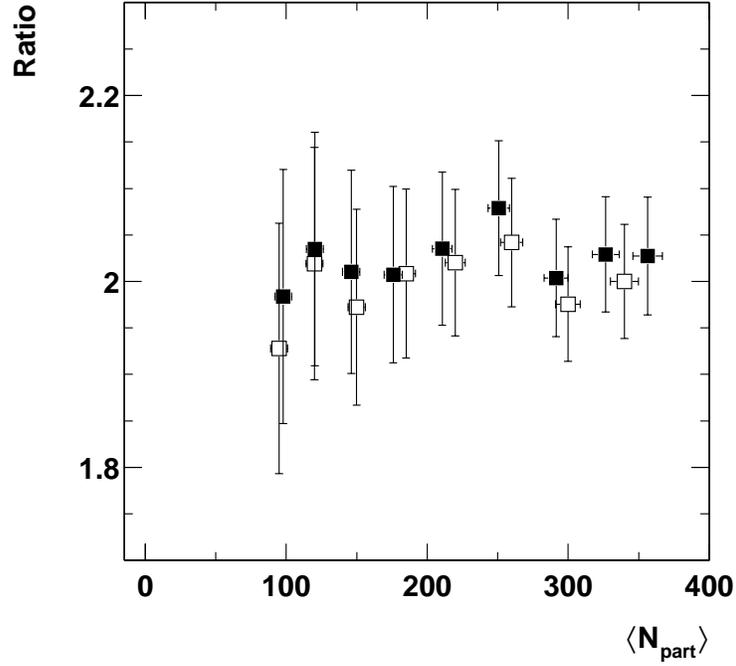


Figure 53. Ratios for the scaled charged particle multiplicity ($dN/d\eta/\langle N_{part}/2 \rangle$) as a function of $\langle N_{part} \rangle$ for 200 and 19.6 GeV for the Octagon based centrality. Closed symbols are for the fixed cross-section bins, open symbols are for the fixed $\langle N_{part} \rangle$ bins.

The ratio of the charged particle multiplicities per participant pair with Paddle Mean and EOctPdlgon centrality methods is performed only for the fixed cross-section bin case and is consistent with the value above. Because the markers are overlapping, it is not shown on Figure 53 for clarity.

5.2.2 Ratio 200/62.4 GeV

The ratios (52) for both EOct and Paddle Mean methods for the same fixed fraction of cross-section are presented in Figure 54. The most probable values for the two ratios show no centrality dependence for the studied part of the cross-section, both slopes are consistent with zero. The corresponding most probable values are $R_{200/62.4} = 1.39 \pm 0.01 \pm 0.02$ and $1.40 \pm 0.01 \pm 0.02$.

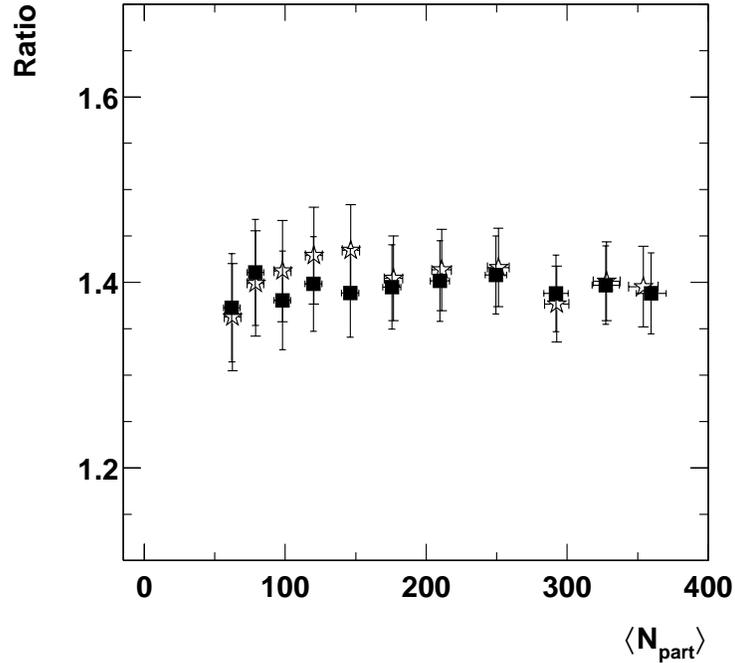


Figure 54. Ratios for the scaled charged particle multiplicity ($dN/d\eta/\langle N_{part}/2 \rangle$) as a function of $\langle N_{part} \rangle$ for 200 and 62.4 GeV for fixed cross-section bins. Closed (open) symbols are for the Octagon (Paddle) based centrality method.

5.3 Energy density

The energy density is calculated from data at mid-rapidity using Bjorken’s estimate, Equation 2.1. Starting from the measured $dN_{ch}/d\eta$ we can obtain dE_T/dy by first correcting for the change of the variable (i.e. $dN_{ch}/d\eta = a \times dN_{ch}/dy$ - see Appendix D) by using HIJING in this case. According to (1; 54) the value of $(dE_T/d\eta)/(dN_{ch}/d\eta)$ at mid-rapidity is ≈ 0.9 GeV¹, which has been found to be independent of centrality. Within experimental uncertainties the same ratio is found over an energy range of 17.2 GeV (from both WA98, NA49 at the SPS) to 200 GeV (from PHENIX at RHIC).

The effective collision area (overlap of the two nuclei), $S = \pi R^2$, was calculated by approximating the effective radius for a collision using $R = (r_0 A^{1/3})$, where the parameter $r_0 = 1.18$ fm is obtained from fits to data² (20). The change of the effective area with centrality, due to change of the impact parameter b , is accounted for by substituting atomic number A with $N_{part}/2$. This method will be used as default and the results can be directly compared to the estimated energy density from other experiments.

Apart for the most central collisions, the effective collision area is not a circle, see Figure 8. Alternatively, this collision overlap (or “almond”) area can be calculated using Equation D.14.

¹This value represents an increase from an earlier measurement of 0.8 GeV (1). The change was due to a redefinition of E_T . The estimate of the energy density can be done using other assumptions, see for example (4)

² r_0 can vary in range between 1.18 (used by other RHIC experiments and here as default for this method) to 1.40 fm, which results in 30% lower energy density. This will be discussed later in text.

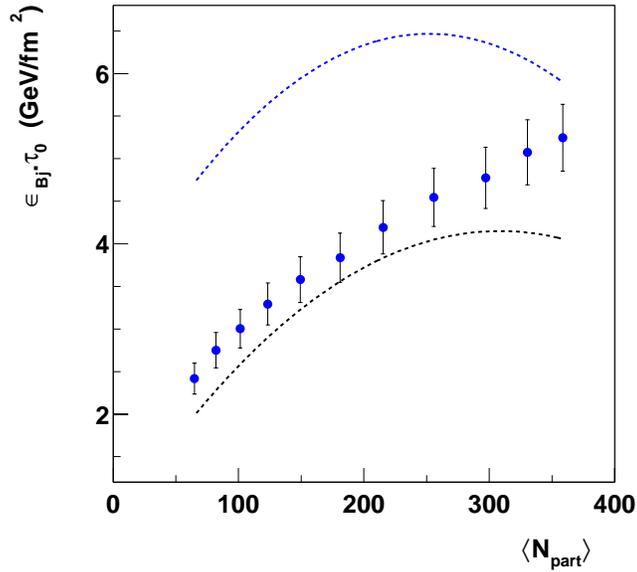


Figure 55. Energy density estimated for 200 GeV. Symbols are for the standard calculation method, dashed lines are limits for the almond calculation (see text).

The impact parameter for a given centrality bin is derived using Glauber model calculations, refer to left panel of Figure 9.

As can be seen from Figure 55 the two ways of obtaining the effective collision area lead to different results. The shape of the energy density is very similar, excluding the central collisions (above 250 participants), where the “almond” result (upper dashed line) is turning compared to the default method (closed circles), which increases monotonically from peripheral to central collisions. This is due to the impact parameter not being zero even for central (3%) events.

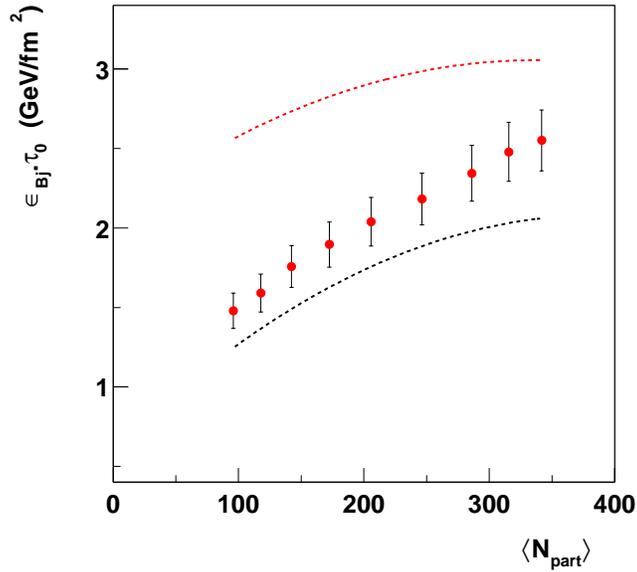


Figure 56. Energy density estimated for 19.6 GeV. Symbols are for the standard calculation method, dashed lines are limits for the almond calculation (see text).

The main uncertainty on the results for all center-of-mass energies is dominated by the large systematic errors on measured charged particle multiplicity. The errors from determining N_{part} are included in those errors. Additional uncertainties from other parameters are small compared to the error on $dN_{ch}/d\eta$ and thus are not included. However, the value of the nuclear radius is a concern when using either method. As discussed in 2.2.2, the nucleon density within the nucleus can be described by a Woods-Saxon distribution; for the case of the gold nucleus

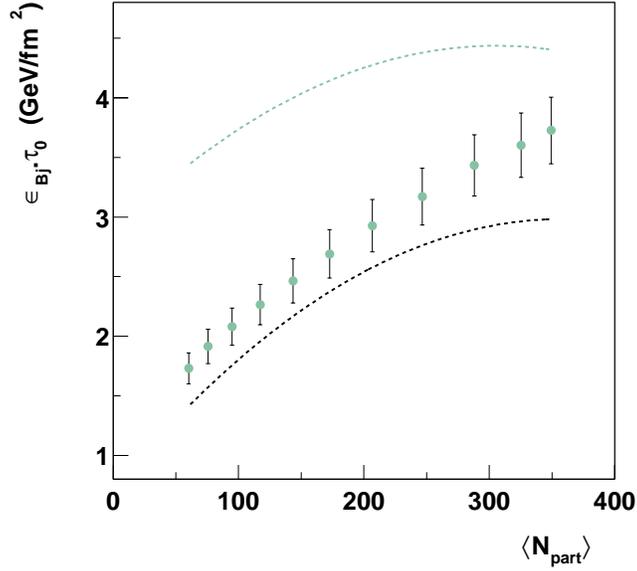


Figure 57. Energy density estimated for 62.4 GeV. Symbols are for the standard calculation method, dashed lines are limits for the almond calculation (see text).

the radius is measured to be 6.8 fm^1 (Figure 10). Two limits (for the radius) are considered and illustrated for the “almond” case. The upper limit (upper dashed line in Figure 55) corresponds to $R = (1.18 \text{ fm} \times 197^{1/3}) = 6.87 \text{ fm}$, which includes the skin width. The lower limit (lower dashed line) is with $R = (1.40 \text{ fm} \times 197^{1/3}) = 8.15 \text{ fm}$ and includes the extreme edges of the nucleus, and possibly accounts for an increase in radius due to the neutron density distribution².

¹radius plus skin depth

²as the measured distribution is for protons only

Bin (%)	200 GeV		19.6 GeV		62.4 GeV	
	EOct	Paddle Mean	EOctRed	EOctPdlgon	EOct	Paddle Mean
0-3	5.34±0.40	5.25±0.39	2.61±0.20	2.55±19	3.83±0.29	3.73±0.28
3-6	5.07±0.38	5.06±0.38	2.48±0.19	2.48±19	3.60±0.27	3.60±0.27

TABLE IX

ESTIMATED RESULTS FOR THE ENERGY DENSITY FOR 200, 19.6 AND 62.4 GEV FOR TWO CENTRALITY DETERMINATIONS. THE MOST CENTRAL COLLISIONS ARE LABELED AS BIN 0-3%. ERRORS REPRESENT 90% C.L. SYSTEMATIC LIMITS.

This uncertainty in the radius can lower the results by 30% but is not included in the final uncertainty.

The formation time of the plasma (τ_0) is usually taken to be ≈ 1 fm/c. Opinions expressed in (55) put the lower limit to 0.2 fm/c, though other experimental considerations (Elliptic flow) put the upper limit to 2 fm/c (4). Because of the importance of the formation time, which signals a system in equilibrium, the results are presented here as $\epsilon_{Bj} \times \tau_0$.

The energy density results for the two most central cross-section bins are presented in Table IX for all three energies. This estimation is based on the multiplicity derived with the ‘‘Paddle’’ centrality methods. The measurements deviate only for the top 3% of the cross-section from the energy density estimates based on EOct centrality. This reflects the multiplicity measurements obtained with different centrality methods, see the discussion in Section 5.1.

CHAPTER 6

COMMENTARY ON THE RESULTS

This Section presents the results for the charged particle multiplicity in Au+Au collisions at three center-of-mass energies. A brief look at the estimated energy density produced during the collisions and the possible QGP formation is discussed first. Comparison of the results with the p+p collisions at the corresponding energy follows. Then, the results are presented as a function of collision centrality and compared with theoretical calculations in order to differentiate between competing models of particle production. Discussion of the observed collision geometry scaling is augmented by other experimental measurements from PHOBOS.

6.1 Energy density versus collision energy

From our measurements we can conclude that a high energy density is reached when Au+Au ions are collided at RHIC (see Figure 58). The estimated energy density, ϵ_{Bj} , is based on measurements of produced charged particle multiplicity with the obtained values, depending on the formation time τ_0 , well above the expected density for the onset of the QGP ($1 \text{ GeV}/\text{fm}^3$).

The dependence of energy density on centrality is similar for all collision energies, see Figure 55 to Figure 57. ϵ_{Bj} is above unity for the measured part of the cross-section¹.

¹the centrality dependence of ϵ_{Bj} is in agreement with the results from STAR at 130 GeV(55) and NA50 at 17.2 GeV (56)

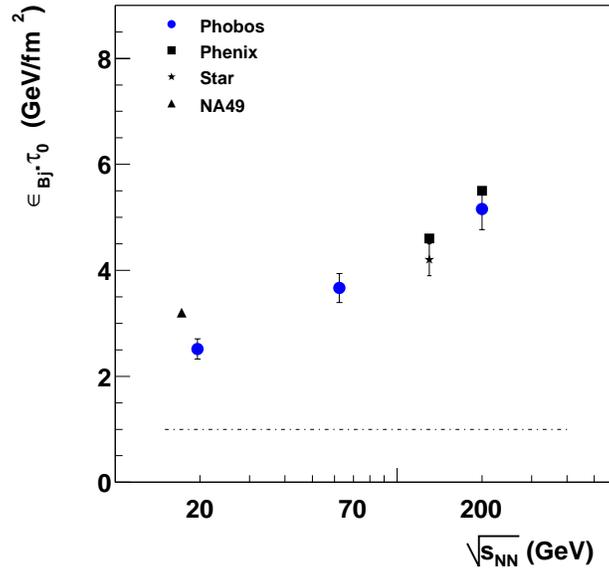


Figure 58. Estimated energy density as a function of $\sqrt{s_{NN}}$. The dashed line represents a lattice calculation (2). Blue symbols are the results for the top 6% of the inelastic cross-section in PHOBOS, square symbols are the results from PHENIX (top 2%) (1; 54) and stars are the results from STAR (top 5%) (55). The black triangle is the result for very central collisions from NA49 (57).

The high energy density reached in central Au+Au collisions at RHIC provides conditions favorable for creating a new state of matter, QGP. Similar energy densities can be reached for p+p collisions at 900 GeV and above (58). The rhetorical question is *what is the minimum energy density needed to create QGP?*

Figure 59 shows that the charged particle multiplicity in Au+Au collisions from $\sqrt{s_{NN}} = 19.6$ to 200 GeV increases logarithmically with collision energy. This trend also holds for other

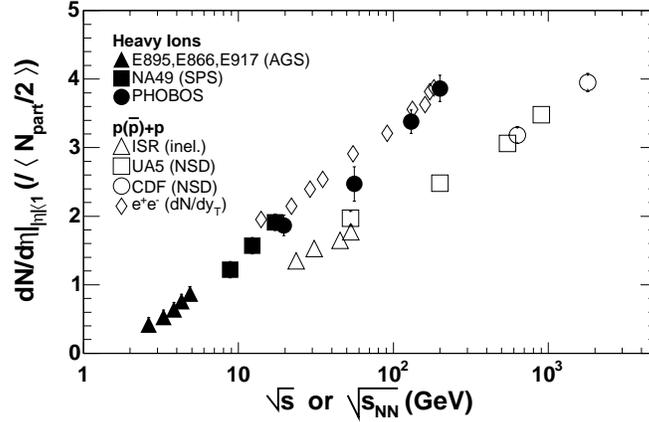


Figure 59. Charged particle multiplicity at mid-rapidity per participant pair as a function of \sqrt{s} . Black circles are the PHOBOS Au+Au results for the top 6% of the cross-section, other markers as labeled on the figure. This figure is from (4).

nucleus-nucleus collisions at much lower energies. Charged particle multiplicity in p+p collisions increases similarly, although the yield of particles is lower.

6.2 Comparison of Au+Au and p+p charged particle multiplicities

The centrality dependence is an invaluable tool to distinguish between models of particle production. The comparison with p+p and other systems at the same collision energy is necessary to reach a better understanding of the Au+Au collisions studied here. Presenting the Au+Au charged particle pseudorapidity density results scaled by $N_{part}/2$ is a way to directly compare with the multiplicity produced by other collision systems. This represents how many more particles are produced per participant pair for the same energy per nucleon collision.

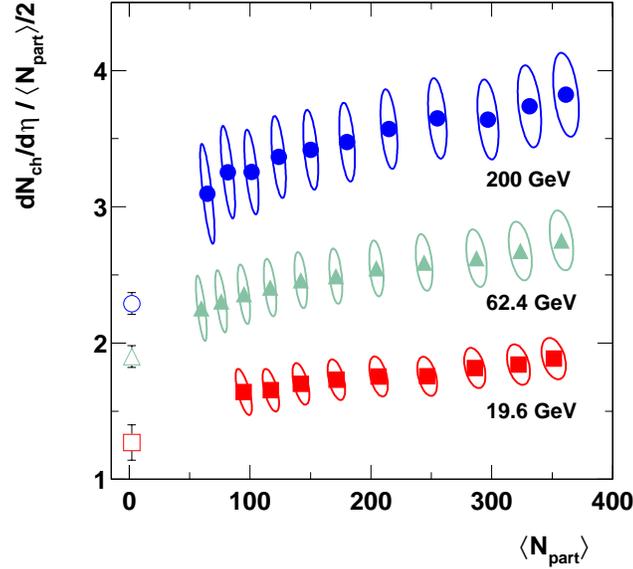


Figure 60. The measured mid-rapidity ($|\eta| < 1$) pseudorapidity density per participant pair as a function of $\langle N_{part} \rangle$ for Au+Au collisions at $\sqrt{s_{NN}} = 19.6$ GeV (red, closed), 62.4 GeV (green, closed) and 200 GeV (blue, closed). The open symbols represent the corresponding $p(\bar{p}) + p$ results (see text). Error ellipses represent 90% C.L. limits.

The inelastic charged particle multiplicity obtained in $p(\bar{p}) + p$ collisions is presented in Figure 60 at $N_{part} = 2$. This is for data obtained at 200 GeV ($dN_{ch}/d\eta|_{|\eta|<1} = 2.29 \pm 0.08$) (23; 59), 62.4 GeV ($dN_{ch}/d\eta|_{|\eta|<1} = 1.90 \pm 0.08$) (60) and extrapolated for 19.6 GeV ($dN_{ch}/d\eta|_{|\eta|<1} = 1.27 \pm 0.13$) (60). Details of the procedure carried out to obtain the data can be found in Appendix D. The $p(\bar{p}) + p$ data are determined over the same pseudorapidity range, $|\eta| < 1$. Clearly, the yield of charged particles per participant pair for the Au+Au collisions is higher than that found in the corresponding $p(\bar{p}) + p$ collisions.

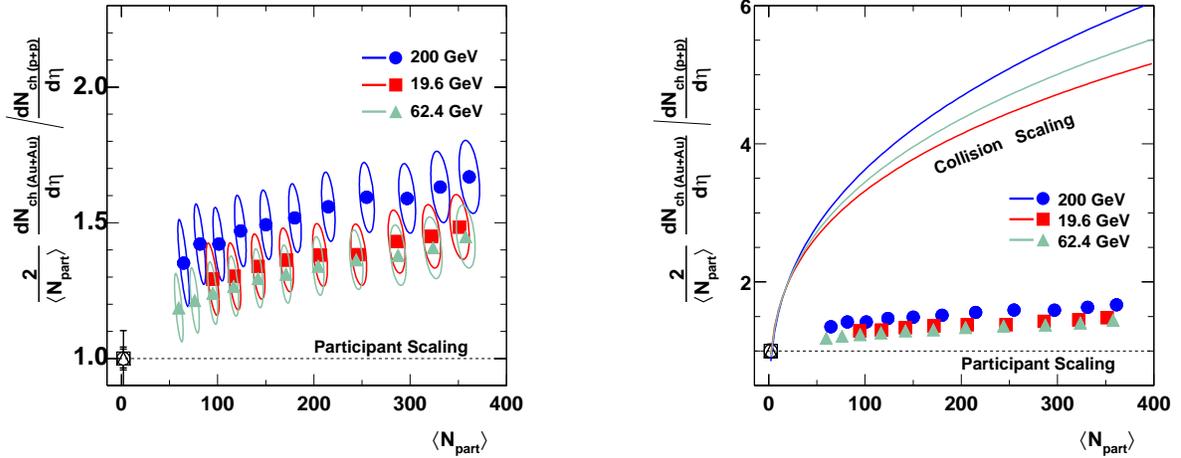


Figure 61. Centrality dependence of the measured Au+Au pseudorapidity density per participant pair divided by the corresponding value obtained in $p(\bar{p}) + p$ collisions. The additional scale error associated with the value of the $p(\bar{p}) + p$ data points (see text) is not taken into account. The horizontal dashed line corresponding to pure N_{part} scaling. The right panel is with the y – axis expanded. Curved lines represent the binary collision (N_{coll}) scaling limit for the three energies.

In order to gain a different perspective on the data, the Au+Au charged particle pseudorapidity density is scaled by the corresponding inelastic $p(\bar{p}) + p$ data, Figure 61. There is an additional scale error associated with the error on the value of the $p(\bar{p}) + p$ data points of 3.5%, 4.2% and 10% for the 200, 62.4 and 19.6 GeV data respectively. Averaged over all measured centralities, the multiplicity in Au+Au collisions exceeds the $p(\bar{p}) + p$ multiplicity by $\approx 40\%$. Due to the uncertainty in the $p(\bar{p}) + p$ values, the similar excess yield in all Au+Au data could be accidental. Within the systematic error, we cannot say that the excess yield for the 62.4 GeV

results is lower compared to the other two energies. As the presented Au+Au systematic errors are not point-to-point, it is unlikely that the observed slope with centrality is accidental.

The dashed horizontal line in Figure 61 represents the expectation for pure participant (N_{part}) scaling. The right panel of Figure 61 also shows the data with an expanded y -axis range and additional curved lines illustrating the expectations for pure binary collision (N_{coll}) scaling at the three energies. In this representation, it is clear that the data at the three energies follow more closely an N_{part} -like dependence, far less than expectations of multiplicity formed from independent p+p collisions, which would follow pure binary scaling.

Comparison of the multiplicity at mid-rapidity produced in Au+Au, d+Au and p+p collisions at 200 GeV is presented in Figure 62. Fewer particles are produced in d+Au collisions than in Au+Au ones and similar to the measurements from p+p collisions. There is no apparent centrality dependence of the d+Au data.

To conclude, the measured multiplicity per participant pair at different energies in central Au+Au collisions is higher than that produced in p+p and d+Au collisions at the same energy. From the centrality dependence, there seems to be a difference in the way particles are produced in Au+Au and d+Au collisions.

6.3 Comparison with lower energy A+A

The WA98 experiment has published a detailed centrality dependence (62) of the mid-rapidity charged particle multiplicity from Pb+Pb collisions at $\sqrt{s_{NN}} = 17.2$ GeV. The evolution with centrality is found to be similar to the measurement at 19.6 GeV presented here. However, on average, their charged particle multiplicity is $\approx 20\%$ higher than that measured by

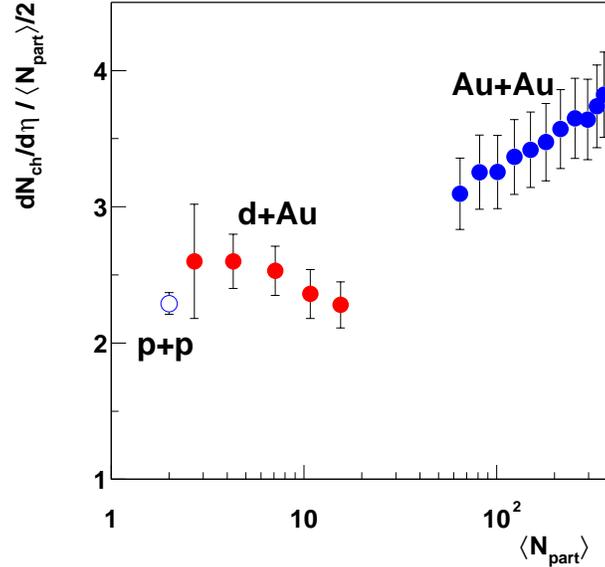


Figure 62. The measured mid-rapidity ($|\eta| < 1$) pseudorapidity density per participant pair as a function of $\langle N_{part} \rangle$ at 200 GeV. The blue (red) circles represent the Au+Au (d+Au) collisions. d+Au data are from (61). The open symbols represent the corresponding $p(\bar{p}) + p$ result. Error on $\langle N_{part} \rangle$ is not included, only the systematic uncertainties are shown.

PHOBOS, see Appendix D.4. There is also an agreement with the results from NA49 (63; 64) for central Pb+Pb collisions at the highest SPS energy of $\sqrt{s_{NN}} = 17.2$ GeV, see Figure 59.

6.4 Comparison with theoretical models

In this Section, only the results for the 19.6 GeV and 200 GeV data will be considered, a factor of ten difference in energy. Even with the large systematic errors (7.5%) on the experimental measurements, comparison of the data can be used to distinguish between the different models of particle production.

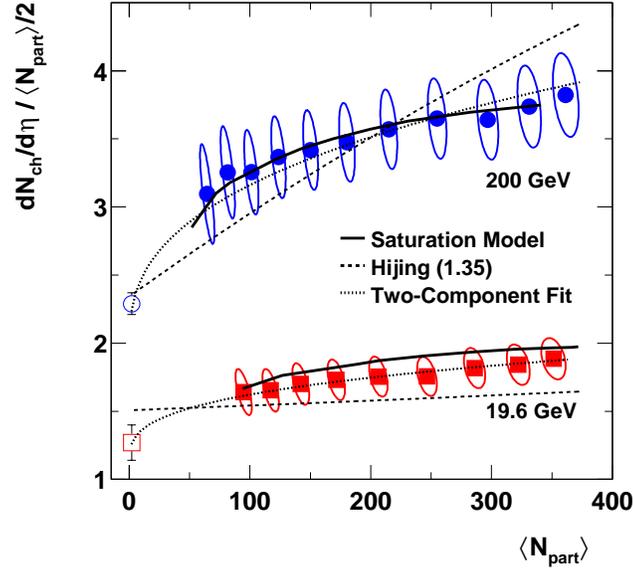


Figure 63. The scaled mid-rapidity multiplicity as a function of $\langle N_{part} \rangle$ for Au+Au collisions at $\sqrt{s_{NN}} = 19.6$ GeV (closed squares) and 200 GeV (closed circles). The open symbols represent the corresponding $p(\bar{p}) + p$ results. Error ellipses represent 90% C.L. limits. The three curves give two model calculations and one fit result (see text).

Initially, the two component parameterization was thought of as a simple but powerful tool to understand the interplay between soft and hard interactions. The dotted line in Figure 63 is a fit to the data using this parameterization, Equation 2.2, proposed in (30). N_{coll} is determined using a Glauber model calculation and it is found to depend on the number of participants, N_{part} , through a simple power law ($N_{coll} = A \times N_{part}^\alpha$). The parameters $A = 0.33$ and 0.37

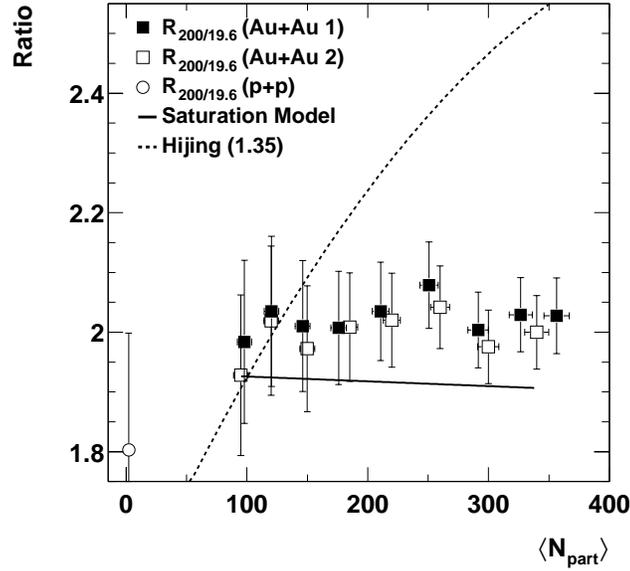


Figure 64. The ratio of 200 and 19.6 GeV, $R_{200/19.6}$, of the data in Figure 63, binned by fraction of cross-section (closed squares) and by matching $\langle N_{part} \rangle$ (open squares). Curves give various calculations. The vertical error bars are combined statistical and systematic 1- σ uncertainty.

and $\alpha = 1.37$ and 1.32^1 are obtained for 200 and 19.6 GeV, respectively. The difference in these parameters at the two energies is due to the measured nucleon-nucleon cross-sections at $\sqrt{s_{NN}} = 200$ GeV ($\sigma_{NN} = 42 \pm 1$ mb) and 19.6 GeV ($\sigma_{NN} = 33 \pm 1$ mb). The remaining

¹these values here as cited in (53) are now been superseded by the ones published in the white paper (4). It was realized that the N_{coll} and N_{part} are very strongly correlated and the α values have to be considered to four significant figures. The new values were actually used in the derivation of new X parameters and did not change the results.

parameters in Equation 2.2 are $\frac{dN_{ch}^{pp}}{d\eta} = n_{pp}$, the yield obtained in $p(\bar{p}) + p$ collisions, and X , which represents the contribution from “hard” processes, assumed to scale with N_{coll} .

The large systematic errors on the data preclude a simultaneous extraction of both n_{pp} and X solely from the Au+Au data. If statistical errors alone are considered, the resulting parameters are $n_{pp} \approx 2.7, 1.3$ and $X \approx 0.09, 0.11$ at 200 and 19.6 GeV, respectively. A value for X can also be obtained by fixing n_{pp} at the measured and extrapolated values (2.29 and 1.27). Again, using only statistical errors, the values are $X = 0.145$ for 200 and $X = 0.120$ for 19.6 GeV, this is depicted by the dotted line in Figure 63. The systematic error on the fit parameter X was determined by allowing the $p(\bar{p}) + p$ value and the data points to vary independently within their systematic uncertainties. As a result, the fraction of hard collisions for both energies is consistent with a single value of $X = 0.13 \pm 0.01(stat) \pm 0.05(syst)$. The equivalence of parameter X at both energies, within the large errors, is surprising as the pQCD cross-section for processes with large momentum transfer is expected to rise from $\sqrt{s_{NN}} = 19.6$ to 200 GeV. This expectation of increasing slope in centrality with collision energy is shown by dashed lines in Figure 63, which represents HIJING predictions, see Section 2.3.2. Although this rise is not conclusively ruled out within the systematics at $\sqrt{s_{NN}} = 200$ GeV, it clearly does not follow the trend found in the data. Calculations from the parton saturation model (35; 65) (solid lines in Figure 63) predict a much weaker centrality dependence for both energies, in better agreement with the experimental data. The two component parametrization will not be

considered for 62.4 GeV¹. In the way it is currently formulated it cannot extract information about the fraction of hard collisions (proportional to the minijet cross-section) at different energies.

Systematic errors dominate the charged particle density measurements at 200 and 19.6 GeV. Performing a ratio is a next logical step as most of the systematic errors cancel (see Section 4.6.2). This leaves a baseline of 3% overall uncertainty on the ratio. The results from the two types of ratio calculations (described in Section 5.2.1) are shown in Figure 64 together with the predictions of two models. As discussed, both sets of data (closed and open squares) are in agreement, even with the significantly reduced systematic errors. Additionally, the slope, and hence the centrality dependence, of both ratios is zero within the errors. With these reduced systematic errors on the ratio, more detailed comparison of the results to calculations can be performed. As shown in Figure 64 model calculations predict a quite different centrality dependence of the ratio over the considered energy range of 200 to 19.6 GeV. HIJING calculation gives the expected increase from pQCD minijet production with centrality over this energy range. This predicted increase is not supported by the data.

The flat centrality dependence of the ratio is relatively well described by the parton saturation model calculation. According to the Saturation model the parameter X is connected with the number of gluons and the increase of multiplicity with centrality should be similar

¹parameters extracted for this energy are equivalent within the error to the ones for 19.6 and 200 GeV

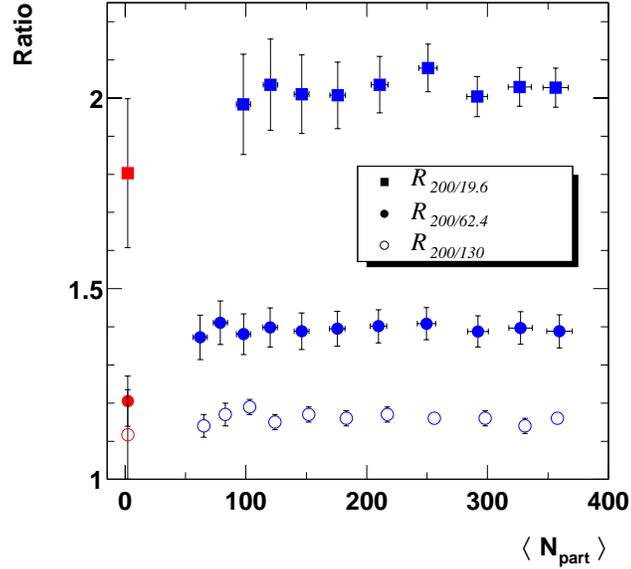


Figure 65. Results of ratios of 200 GeV to all energies. Blue (red) symbols are Au+Au (p+p) data.

for all energies. The energy dependence is expected to rise logarithmically with \sqrt{s} , which is confirmed by the measurements of multiplicity as a function of energy, shown in Figure 59.

The majority of the existing models for particle productions do not describe the data. As will be shown in the next Section, the data exhibits some very simple scaling properties.

6.5 Scaling properties

From Figure 64 one can see that there is no centrality dependence for both the “Au+Au 1” and “Au+Au 2” ratios. The ratio of the measured yields shows a clear geometry scaling for the central 40% of the inelastic cross-section. The same observation is confirmed by the ratios

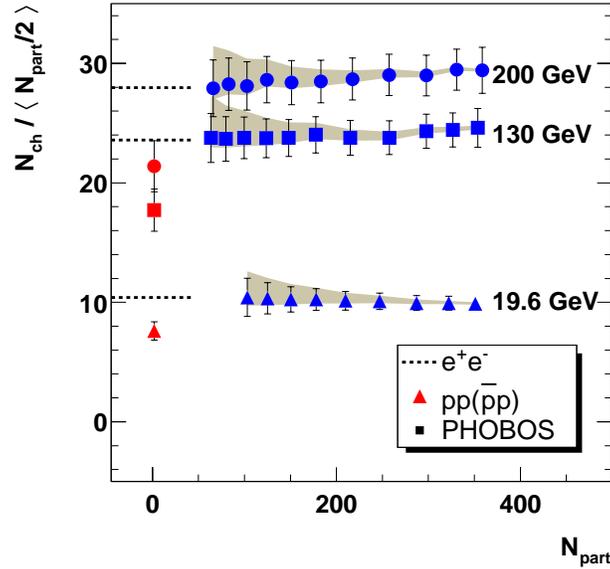


Figure 66. Total number of charged particles versus $\langle N_{part} \rangle$ for three energies. Blue (red) symbols are Au+Au (p+p) data.

of 200 and 130 GeV, $R_{200/130} = 1.14 \pm 0.01 \pm 0.05$ (51), and 200 and 62.4 for the top 50% of the inelastic cross-section. All ratios are shown in Figure 65.

The multiplicity production seems to be driven by the same laws (as a function of centrality) in Au+Au collisions where the energy is different by over an order of magnitude. The results are striking and simple, opening the possibility that simpler physics could be responsible for this observation than that comprising the theoretical models.

This is not the only result from PHOBOS, which exhibits a “geometry scaling”. Figure 66 illustrates that the total charge, N_{tot} , per participant pair is independent of centrality for all

RHIC energies (66). Figure 67 shows the ratio of the hadron p_T yields for 200 and 62.4 GeV for various p_T bins. The same scaling holds for all p_T bins.

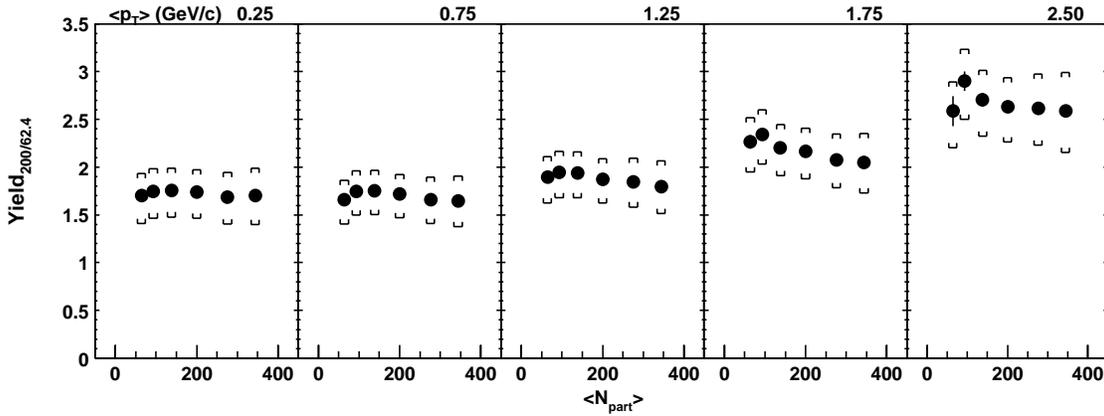


Figure 67. Ratios of charged particle spectra at 200/62.4 GeV for a selection of p_T bins. The data are from (67; 68).

6.6 Discussion on centrality

Centrality has proved to be a very important tool to extract information in heavy ion collisions. This helps to make strong conclusions about the underlying mechanisms that produce the data. As such, the details of the centrality determination may affect the results by which the conclusions are drawn, and one must perform tests to ensure consistency. By forming a centrality method from different regions of particle production (mid-rapidity and away from mid-rapidity), it is possible to measure existing effects.

We have found that for the Au+Au collisions, there are no substantial effects which could change the final conclusions. The best comparison of data is with the scaled results (by $\langle N_{part} \rangle / 2$), where most of the fluctuations from the centrality determination cancel. Only in the most central 0-3% of the inelastic cross-section are effects clearly observed, although the difference in yield derived from different centrality methods is tracked by the $\langle N_{part} \rangle$ found from the MC.

CHAPTER 7

CONCLUSION

This Thesis has presented a measurement of the mid-rapidity charged particle multiplicity using the Vertex Tracklet analysis at three center-of-mass energies: 19.6, 62.4 and 200 GeV. The yield of charged-particles per participant pair, measured in Au+Au collisions, is higher by $\approx 40\%$ than that found in corresponding $p(\bar{p})+p$ collisions. Moreover, the centrality dependence reveals that the multiplicity in Au+Au is different from the multiplicity produced in both the $p(\bar{p})+p$ and d+Au systems; the data trend follows more closely an N_{part} -like dependence, with a mild increase with centrality.

The energy density reached in the collision is estimated to be well above the expected value for the onset of the QGP from theoretical calculations. Energy density results, as a function of center-of-mass energy, exhibit a steady (logarithmic) growth. All results, for the measured part of the cross-section, in all datasets, are greater than that needed for formation of the QGP.

Ratios of the 200 GeV data with respect to 19.6 and 62.4 GeV provide a precise experimental measurement to distinguish between different models of particle production in heavy ion collisions. The expected rise in multiplicity from pQCD processes (minijets) is not observed in data; the KLN Saturation model is found to describe the trend of the data.

The absence of a rise in the ratios as a function of centrality for energies different by an order of magnitude is a remarkable observation. The data appears to exhibit simple scaling

properties for all measured energies. This observation is confirmed by other measurements in PHOBOS and can be used to guide our search for the QGP.

APPENDICES

Appendix A

PHOBOS COLLABORATION 2004

B.B.Back¹, M.D.Baker², M.Ballintijn⁴, D.S.Barton², R.R.Betts⁶, A.A.Bickley⁷, R.Bindel⁷, W.Busza⁴, A.Carroll², Z.Chai², M.P.Decowski⁴, E.García⁶, T.Gburek³, N.George², K.Gulbrandsen⁴, C.Halliwell⁶, J.Hamblen⁸, M.Hauer², C.Henderson⁴, D.J.Hofman⁶, R.S.Hollis⁶, R.Hołyński³, B.Holzman², A.Iordanova⁶, E.Johnson⁸, J.L.Kane⁴, N.Khan⁸, P.Kulinich⁴, C.M.Kuo⁵, W.T.Lin⁵, S.Manly⁸, A.C.Mignerey⁷, R.Nouicer^{2,6}, A.Olszewski³, R.Pak², C.Reed⁴, C.Roland⁴, G.Roland⁴, J.Sagerer⁶, H.Seals², I.Sedykh², C.E.Smith⁶, M.A.Stankiewicz², P.Steinberg², G.S.F.Stephans⁴, A.Sukhanov², M.B.Tonjes⁷, A.Trzupek³, C.Vale⁴, G.J.van Nieuwenhuizen⁴, S.S.Vaurynovich⁴, R.Verdier⁴, G.I.Verés⁴, E.Wenger⁴, F.L.H.Wolfs⁸, B.Wosiek³, K.Woźniak³, B.Wysłouch⁴

¹ Argonne National Laboratory, Argonne, IL 60439-4843, USA

² Brookhaven National Laboratory, Upton, NY 11973-5000, USA

³ Institute of Nuclear Physics PAN, Kraków, Poland

⁴ Massachusetts Institute of Technology, Cambridge, MA 02139-4307, USA

⁵ National Central University, Chung-Li, Taiwan

⁶ University of Illinois at Chicago, Chicago, IL 60607-7059, USA

⁷ University of Maryland, College Park, MD 20742, USA

⁸ University of Rochester, Rochester, NY 14627, USA

Appendix B

PHYSICS FORMULAE

The formulae in this Appendix are solely provided for completeness of the Thesis. These are stated without derivation and one should consult the literature for more discussion.

B.1 The running coupling of the strong interaction

The quark-quark interaction weakens at short distances (“asymptotic freedom”) because of the momentum dependence (or running) of the coupling constant, Equation B.1. This coupling is characterized by the momentum transfer, Q , and the QCD momentum scale, Λ . The final variable concerning the coupling constant is the number of quark flavors, N_f .

$$\alpha_s(Q^2) = \frac{16\pi^2}{(11 - \frac{2}{3}N_f)\ln(Q^2/\Lambda^2)} \quad (\text{B.1})$$

B.2 Energy density

The equation of state for a non-interacting QGP is given by Equation B.2.

$$\epsilon_{SB} = \epsilon_{q+\bar{q}} + \epsilon_g = \left[6N_f \frac{7\pi^2}{120} + 16 \frac{\pi^2}{30} \right] T^4 \quad (\text{B.2})$$

The equation of state for a pion gas (i.e. no barions ($\mu = 0$)) leads to Equation B.3.

$$\epsilon_\pi = \frac{3\pi^2}{30} T^4 \quad (\text{B.3})$$

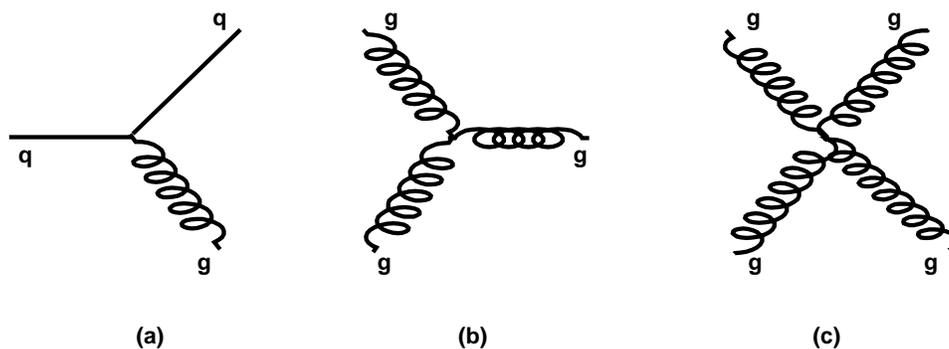


Figure 68. Example diagrams of the strong interactions. (a) quark splitting into a quark and gluon, $q \rightarrow q + g$, (b) gluon splitting in two gluons, $g \rightarrow g + g$, (c) self interaction of gluons, $g + g = g + g$.

B.3 Kinematic variables

In high energy physics the speed of light, c , and the Planck constant, \hbar , are set to 1. The energy and momentum of a particle are described by the four momentum:

$$p^\mu = (E, p_x, p_y, p_z) \tag{B.4}$$

The square of the four momentum, $p^\mu p_\mu$, is a relativistic invariant, i.e. $p^\mu p_\mu = \text{const} = -m^2$ in any reference frame. The energy of a free particle with mass m is described by the relativistic equation, Equation B.5.

$$E^2 = p^2 + m^2 \tag{B.5}$$

In PHOBOS the choice of the coordinate system is such that the z -axis is defined along the beam direction (direction in blue ring), y is vertically up, x is perpendicular to both and points toward the center of the RHIC ring. The polar angle, θ , is the angle between $+z$ and the momentum vector of the particle. The transverse and longitudinal momentum vector magnitudes of a particle are given by Equation B.6 and Equation B.7.

$$p_T = p \sin \theta = \sqrt{p_x^2 + p_y^2} \quad (\text{B.6})$$

$$p_L = p \cos \theta = p_z \quad (\text{B.7})$$

Upon defining the longitudinal “velocity” of particles (or the beams) it is convenient to use a Lorentz invariant quantity. In high energy physics this variable is referred to as “rapidity”, defined in Equation B.8. Being a Lorentz invariant, when shifting to a different reference frame, the change is additive. For example, transforming from the center-of-mass to the rest frame of target nucleus, Equation B.9, requires only knowledge of the target “beam rapidity”. Beam rapidity in the center-of-mass frame is calculated using Equation B.10. β is the relativistic velocity of the particle ($\beta = \frac{v}{c}$). This leads to a simple comparisons of the RHIC and fixed target SPS data.

$$y = \operatorname{atanh} \left(\frac{p_L}{E} \right) = \frac{1}{2} \ln \frac{E + p_L}{E - p_L} \quad (\text{B.8})$$

$$y' = y + y_{beam} \quad (\text{B.9})$$

$$y_{beam} = \operatorname{tanh} \beta = \frac{1}{2} \ln \frac{1 + \beta}{1 - \beta} \quad (\text{B.10})$$

In Table X the beam rapidities (y_{beam}) are calculated for Au+Au collisions at RHIC using Equation B.8.

Also used are $E_{beam} = \frac{\sqrt{s_{NN}}}{2}$ and $p_L^2 = p_{beam}^2 = E_{beam}^2 - u^2$, where u is the atomic mass unit.

energy (GeV)	y_{beam}
19.6	3.05
62.4	4.20
130	4.94
200	5.37

TABLE X

BEAM ENERGIES FOR AU+AU COLLISIONS.

For very relativistic particles $E = p$ ($E \gg m$) we can define a “pseudo” rapidity variable (called pseudorapidity), Equation B.11. This variable is useful when the identity of the particles is not known.

$$\eta = \frac{1}{2} \ln \frac{p + p_L}{p - p_L} = \frac{1}{2} \ln \frac{1 + \cos\theta}{1 - \cos\theta} = -\ln \tan \left(\frac{\theta}{2} \right) \quad (\text{B.11})$$

The transverse mass of a particle is defined as:

$$m_T = \sqrt{p_T^2 + m^2} \quad (\text{B.12})$$

B.4 The transformation from rapidity to pseudorapidity

The transformation between rapidity and pseudorapidity, $dy = a \times d\eta$ (Equation B.13), is shown in Figure 69.

$$\frac{dN_{ch}}{d\eta} = \frac{dN_{ch}}{dy} \sqrt{1 - \left(\frac{m}{m_T \cosh y} \right)^2} \quad (\text{B.13})$$

For the case of mid-rapidity (averaged over $|\eta| < 1$) the factor a found from HIJING for 200 GeV Au+Au collisions(as in Figure 69) is $a = 1.20$. PHENIX uses $a = 1.19 \pm 0.01$ for 130 GeV (1) and $a = 1.20$

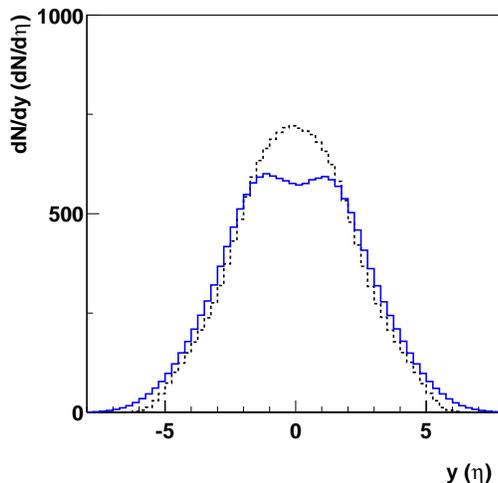


Figure 69. The rapidity density (dN/dy) and pseudorapidity density ($dN/d\eta$) are shown as black and blue histograms for a 200 GeV Au+Au HIJING simulation. The largest difference is observed at mid-rapidity. Shifting the distributions by adding a constant does not change the overall shape of either distribution.

for 200 GeV (54). The STAR collaboration (55) uses Equation B.13, where the m_T are calculated for $\pi^\pm, K^\pm, p, \bar{p}$, but the overall factor is not quoted.

B.5 Kinematics of DIS

The brief introduction here follows from (11). The relevant definitions for the momenta for the electron and proton are shown in Figure 70.

The negative four momentum transfer squared, Q^2 , is connected to q^2 . This is the momentum transfer by the virtual photon to the hadronic system:

$$Q^2 = -q^2 = (k - k') \tag{B.14}$$

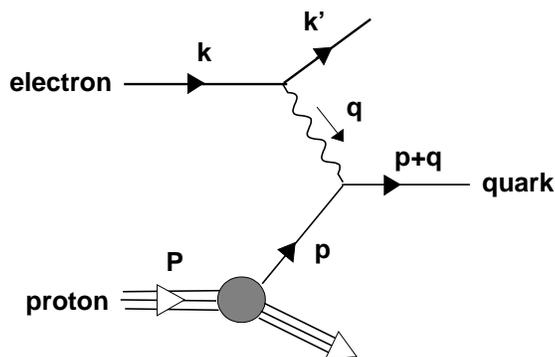


Figure 70. Deep inelastic scattering in QCD. High energy electron scatters from a quark taken from the proton wavefunction.

The longitudinal fraction of the constituent (of the incoming proton), ξ , takes a value $0 < \xi < 1$. Thus, from the figure, $p = \xi P$ (P is the initial proton momentum). For elastic electron-quark scattering $\xi = x$ and in the literature x is used interchangeably with ξ ; x is known as the fraction of proton momentum, or Bjorken- x .

$$x = \frac{Q^2}{2P \cdot q} \quad (\text{B.15})$$

Inelasticity y in the proton rest frame ($y = q^0/k^0$) is the fraction of the incident electron's energy transferred to the hadronic system.

$$y = \frac{2P \cdot q}{2P \cdot k} = \frac{2P \cdot q}{s} \quad (\text{B.16})$$

From these definitions Q^2 is related to the center-of-mass energy by Equation B.14.

$$Q^2 = xys \tag{B.17}$$

The cross-section for a deep inelastic scattering is used to derive the cross-section for a hard scattering processes in hadron collisions; $h + h \rightarrow q + q$. The formulae in (11), (pages 563-6), are used in HIJING to calculate the jet cross-section σ_{jet} .

B.6 Accelerator variables

Equation B.18 is an approximation used to convert the energy from a fixed target reference frame to a center-of-mass reference frame.

$$E_{CM} \approx \sqrt{2 \times E_{Lab}} \tag{B.18}$$

A schematic representation of a beam interacting with a target is presented in Figure 71. The flux of a beam through a target with cross-sectional area A is defined as:

$$\Phi_a = \frac{\dot{N}_a}{A} \tag{B.19}$$

$$= n_a v_a \tag{B.20}$$

where Φ_a is the flux, \dot{N}_a is the number of particles passing a point in space per unit time. One can simplify the Equation B.19 to Equation B.20, where n_a is the density of particles in the beam and v_a is the beam velocity.

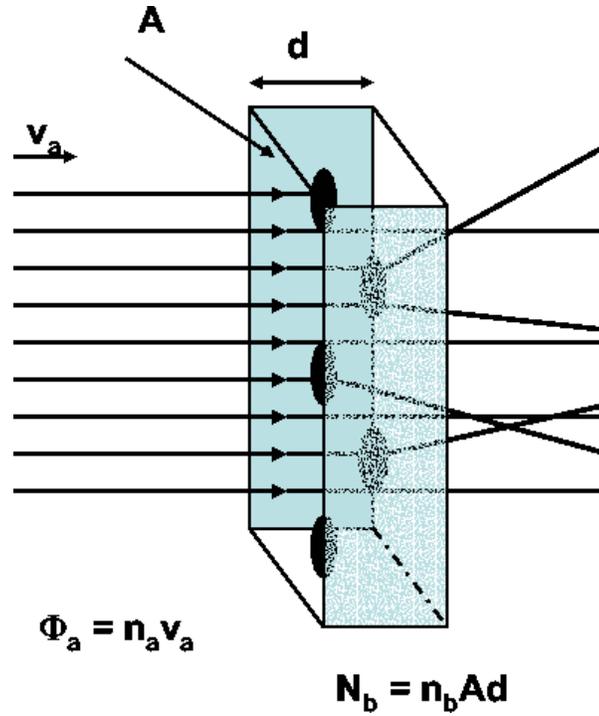


Figure 71. Beam interaction with a target.

The reaction rate R (number of collisions per unit time $\dot{N} = N/t$) (measured in units s^{-1}) is determined by the flux of the beam, the number of *target* particles within the beam cross-sectional area N_b and the effective area of one single (target) scattering center σ_b (the cross-section).

$$R = \Phi_a N_b \sigma_b = \mathcal{L} \sigma_b \quad (\text{B.21})$$

Here, $\mathcal{L} = \Phi_a N_b$ denotes the luminosity and is measured in $cm^{-2}s^{-1}$. Number of interactions (events) (N) is found by integrating the luminosity over the time (L - known as the integrated luminosity).

$$N = \sigma_b \int \mathcal{L} dt = \sigma_b L \quad (\text{B.22})$$

For colliders, here RHIC:

$$\Phi_a = \frac{\dot{N}_a}{A} = \frac{N_a}{A} \frac{nv}{C} = \frac{N_a \cdot n \cdot f}{A} \quad (\text{B.23})$$

$$\mathcal{L} = f \frac{nN_a N_b}{A} = f \frac{nN_a N_b}{4\pi\sigma_x \sigma_y} \quad (\text{B.24})$$

1. N_a and N_b : number of particles per bunch (e.g blue beam) for each beam,
2. C : circumference of the ring,
3. n : number of bunches per beam,
4. v : velocity of the accelerated particles,
5. f : revolution frequency,¹
6. A : beam cross-section,
7. σ_x, σ_y : standard deviation of the beam profile in x, y .

¹The accelerator constant (or period) can be calculated using the equation for particle with charge q and mass m moving in a homogeneous magnetic field B , such that

$$qvB = \frac{mv^2}{r} \quad \text{const } T = \frac{2\pi r}{v} = \frac{2\pi m}{qB} \quad (\text{B.25})$$

Appendix C

FROM THE ACCELERATOR TO THE DETECTORS

C.1 RHIC

The Relativistic Heavy Ion Collider at Brookhaven National Lab began operation in 1999. For the past five years the collider has provided collisions of gold ions and polarized protons to four experiments. Currently, during 2005 operation, the RHIC machine accelerates and collides beams of copper to a maximum energy of $\sqrt{s_{NN}} = 200$ GeV. The maximum energy to which a single heavy ion beam can be accelerated is 100 GeV/u and 250 GeV/u for protons. The limitation to the size of the heaviest ions (gold), which can be accelerated, is subject to available ion source. The collider-accelerator complex consists of two superconducting hadron collider rings, built in a 3.8 km circumference tunnel, and utilizes prior hadron accelerators as an injector to the collider rings: Alternating Gradient Synchrotron (AGS), Booster and the Tandem Van de Graaff. Additionally, the existing Proton Linac is used as a source for polarized protons.

C.1.1 The collider

The RHIC acceleration process for the case of gold ions is described in (69), see Figure 72. At injection, three accelerators in a chain, boost the energy of the produced ions and strip the electrons. The process starts in the Tandem Van de Graaff. Negatively charged gold ions from the ion source are partially stripped with foil of their electrons and then accelerated to 1 MeV/u. At the end of the Tandem, with the help of bending magnets, the positively charged gold ion beam (+32) is delivered to the Booster. The Booster Synchrotron further accelerates the ions to 95 MeV/u and at the exit strips them to charge +77. The ions are then injected in 24 bunches to the AGS. The AGS is the last stage which completes the injection. The ions are accelerated to the RHIC injection energy of 10.8 GeV/u.

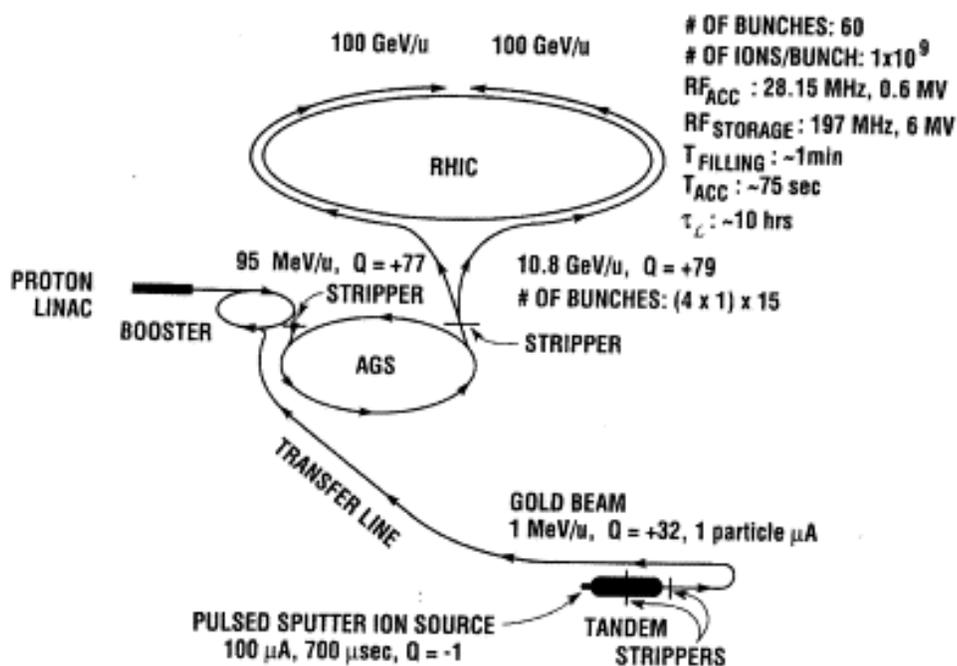


Figure 72. The RHIC complex.

The 24 bunches are debunched and then rebunched into 4. At the exit of the AGS the ions are fully stripped to +79. The four bunches are ejected from the AGS, one at a time, to RHIC through the “AGS to RHIC beam transfer line”.

The RHIC collider has two quasi-circular accelerator/storage rings, known as “blue” (where ions move in a clockwise-direction) and “yellow” (counter-clockwise direction). A two Radio Frequency (RF) system is used for acceleration and storage of beam bunches: 28 MHz to capture the bunches from the AGS and accelerate them to the top energy; and 197 MHz to provide collisions for the experiments. The transition from the injection to the top RHIC energy is provided with the help of superconducting magnets. Ions in one bunch have some spread in energy. During acceleration, when the “transition” point (35 GeV/n) is reached, the fastest particles, traveling on the outside in the ring, are in step (have

the same frequency) with the slower ones, traveling on the inside. This point is critical in the acceleration process in order to keep the beam stable. When the desired top energy is reached, the beams can be steered to a co-linear path for head on collisions at six possible interaction point by a pair of dipole magnets situated at approximately 23 and 10 m from the interaction points.

For gold beams at the maximum energy of 100 GeV/u, the expected luminosity of the machine is $2 \times 10^{26} \text{ cm}^{-2} \text{ s}^{-1}$, with 60 bunches per ring. The maximum lifetime for any one store is expected to be up to 10 hours.

C.2 Experiments

Currently, there are four heavy ion experiment operating at RHIC. Two small ones, BRAHMS and PHOBOS (the experiment concerned in this Thesis), and two big ones, PHENIX and STAR. Though the size of the experiments is determined by comparison of the dimensions of the detectors and the number of people working on them, the quality of physics provided by all experiments is at the same high level. RHIC experiments are important for the heavy ion physics community, providing complementary and high quality measurements.

C.2.1 BRAHMS

The experiment's name stands for Broad RAnge Hadron Magnetic Spectrometer. The main part of the detector consist of two movable magnetic spectrometer arms. One measuring and identifying particles traveling in the forward direction, with very high p_T and large rapidities, and one very close to the nominal interaction point, covering the particles produced at mid-rapidity. The moving of the spectrometer arms ensures exploration of wide range of kinematic regions, providing detailed information and precise measurements of the momentum spectra and yields of produced particles. The rapidity region covered by BRAHMS is the largest of all RHIC experiments, making BRAHMS' results unique for exploring new physics and comparing to model predictions in all collision systems. More about the experiment layout and all detector systems can be found in (70).

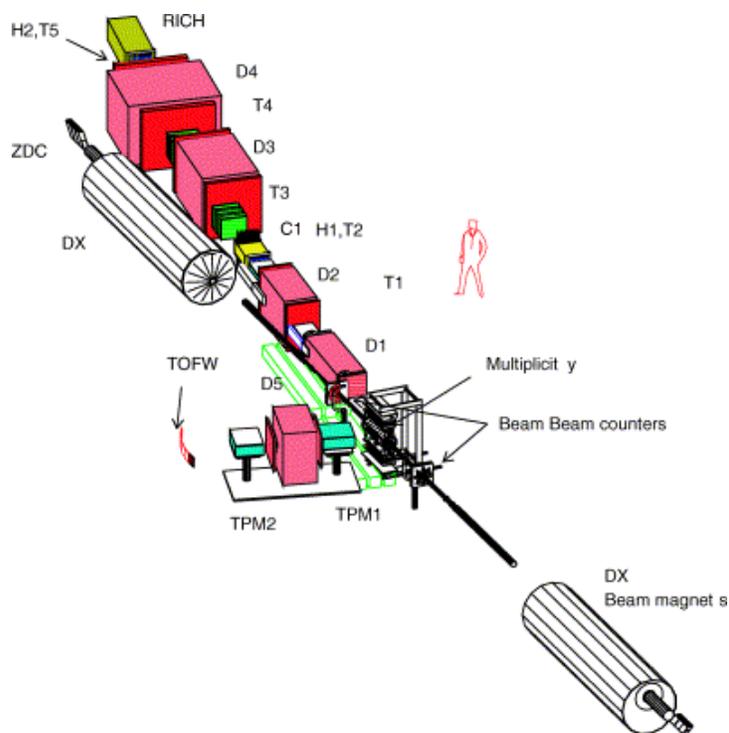


Figure 73. The BRAHMS detector at RHIC. Schematic drawing from (70).

C.2.2 PHENIX

PHENIX detector, as described in (71), is designed to measure a broad variety of signals from heavy ion and polarized proton-proton collisions, sensitive to all stages of the collisions.

The detector consists of central two arm spectrometer, made from concentric layers of various detectors, which reconstruct particle tracks in a selected solid angle. Two muon arms augment the detector, providing a hadron and electron identification over a broad transverse momentum range. A major part of the experiment program is dedicated to measurement of leptonic signals and direct photons emerging from the collision, jets from the hard scattering of the constituent quarks and gluons, as well as study of the created deconfined state in the collision by measuring of the expected J/ψ suppression. The possible

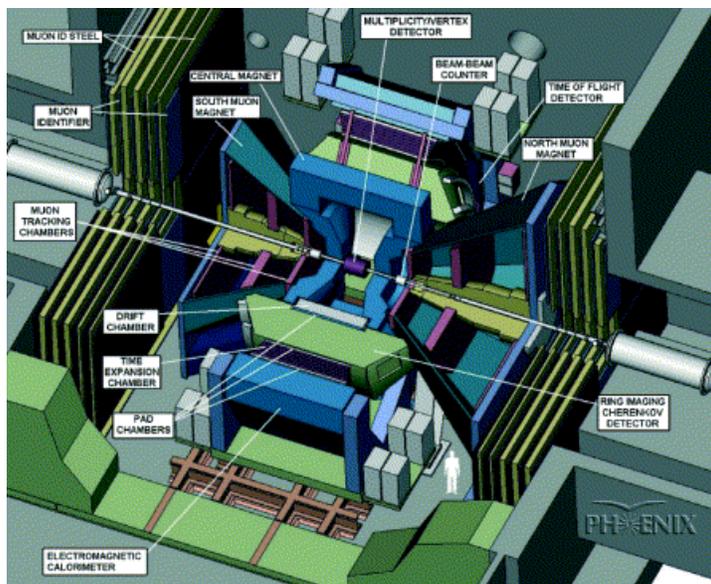


Figure 74. The PHENIX detector at RHIC. Schematic drawing from (71).

changes in the lifetime and width of ϕ , ρ and ω mesons as a result of the chiral symmetry restoration and consequent reduction in the quark mass can also be studied.

C.2.3 STAR

The STAR detector (for detailed information see (72)) has close to 4π tracking capability for measuring of hadron production over a large solid angle. It has a solenoidal design with large cylindrical Time Projection Chamber (TPC) inside a magnetic field. The TPC can reconstruct a large number of tracks with high precision, with identification over significant momentum range at mid-rapidity. The photon and electron detection is provided by the Barrel and End-cap Electromagnetic calorimeters. STAR is focusing on measurements of produced hadron and global observables even for very peripheral collisions, particularly on event-by-event characterization of the heavy ion collisions and produced hadronic jets.

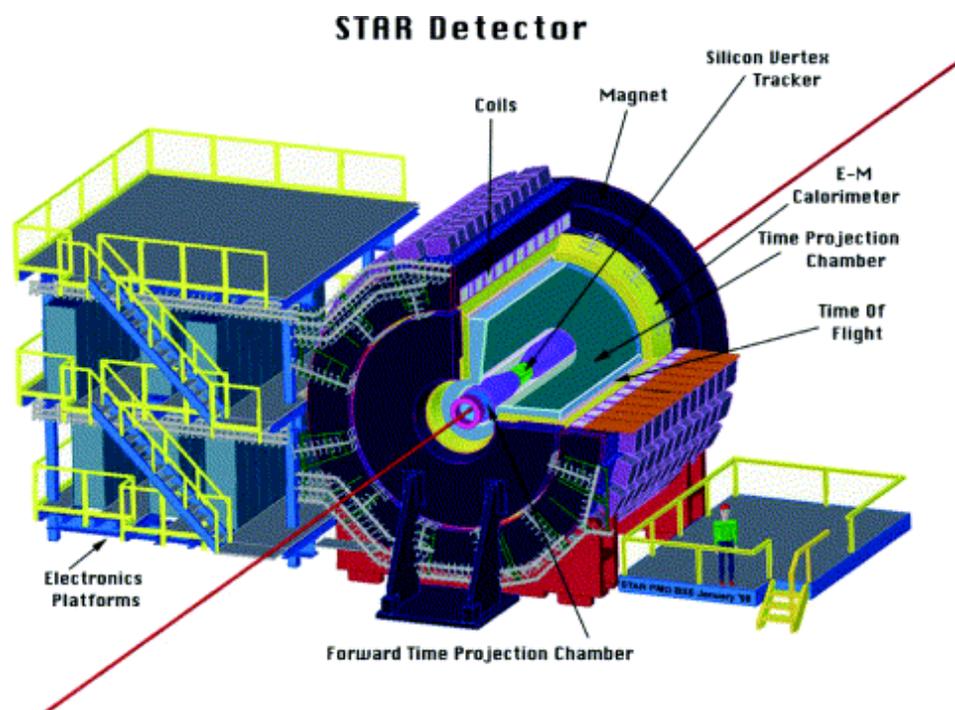


Figure 75. The STAR detector at RHIC. Schematic drawing from (72).

The experiment has a program on spin physics from polarized protons to study the spin structure of the proton.

C.3 PHOBOS

The PHOBOS detector comprises of three major sub-systems. The multiplicity detectors, magnetic Spectrometer and trigger detectors. The most recent detector configuration is shown in Figure 76. PHOBOS has a left hand coordinate system. Z -axis points along the beam pipe in the direction of the blue beam and toward the spectrometer (from bottom right to the top left corner on the plot), Y is vertically up and X -axis is horizontal. In the case of $d+Au$ collisions, the deuteron was moving in the positive Z direction (blue beam), the gold ion was moving in the negative Z direction (yellow beam).

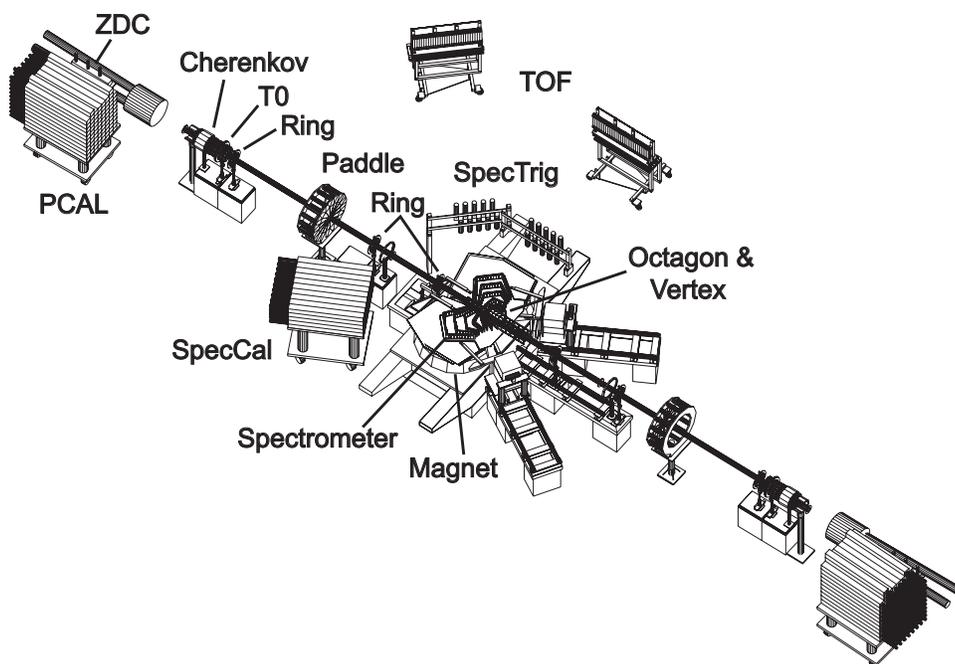


Figure 76. Schematic drawing of the PHOBOS detector for the PR04 Au+Au run. The beam collide at the point in the middle of the Vertex detector. ZDC and PCAL detectors are located further than shown.

The multiplicity detectors have almost full 4π coverage of the solid angle. They consist of a single layer Si pad detectors, which measure the total number of charged particles produced in a collision, their distribution in azimuthal and polar angles. The multiplicity detectors provide accurate information for the event vertex position. The Vertex and Octagon detector are situated closest to the interaction point. They are mounted on a common frame, see Figure 77. The Octagon detector covers $|\eta| < 3.2$, completely surrounding the beam pipe, except for openings for the Vertex detector¹ and Spectrometer.

¹Vertex Detector is described in Chapter 3.3.1

The three annular Rings, situated symmetrically on the two sides of the interaction point, extend the pseudorapidity coverage up to 5.4 units.

The silicon sensors of the Spectrometer are mounted on eight frames; each arm consist of 16 layers, the magnetic field is 2T. The total coverage of the Spectrometer is $0 < \eta < 2$ and 0.1 radians in azimuth for particles traversing all Spectrometer arms. Particle identification is based either on the energy loss measured in the Spectrometer and momentum information from the reconstructed tracks or by the two Time of Flight walls (TOF). The hadron calorimeter (SpecCAL) was installed for the Au+Au PR04 run to measure the energy of high p_T particles emerging from one of the Spectrometer arms.

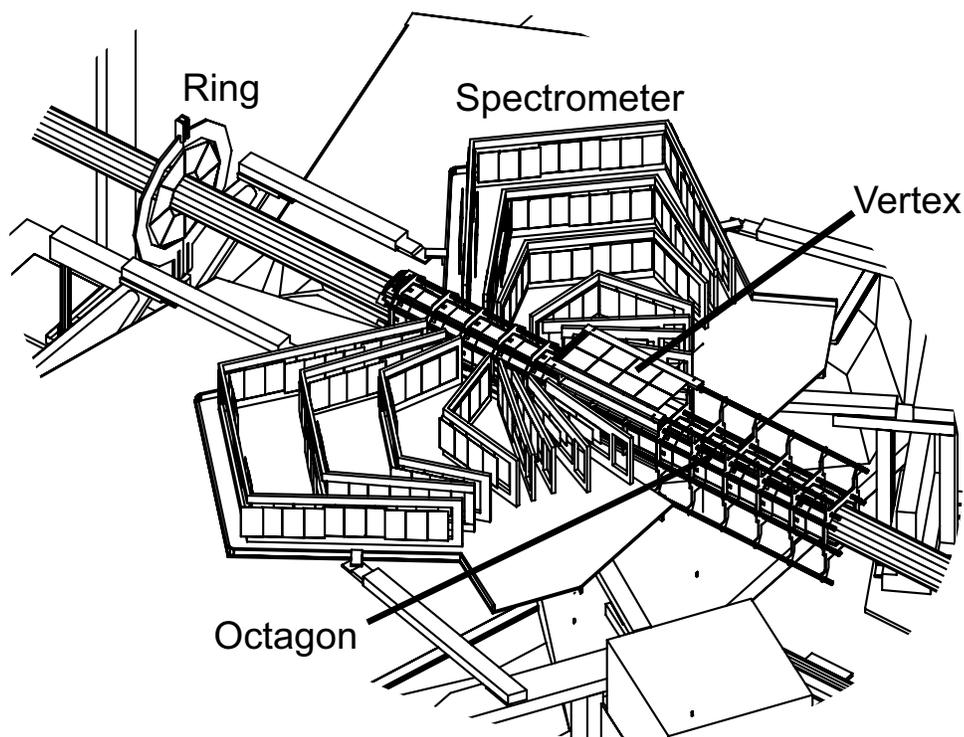


Figure 77. A view of the detectors in PHOBOS situated close to the interaction point.

The main trigger detectors were discussed in Chapter 3. The Proton calorimeter (PCal) is a new addition to the PHOBOS detector for the d+Au PR03 run. The two towers are located behind the first accelerator magnets, which bend the spectator protons and shower the PCal. PCal is used for centrality determination in the d+Au system.

Appendix D

SUPPORTING ANALYSIS PLOTS AND DATA INFORMATION

D.1 Data runs

Information about the data and MC used for the analysis.

D.1.1 19.6 GeV data

Dataset: Year = PR01

Runs = 9204-6, 9209, 9211-20

DV tag = ONLV_2_1_8

MCset: Runs = 6001-3

Smearing version = SMV_19GEV_7

D.1.2 200 GeV data

Dataset: Year = PR01

Runs = 7267,7269,7284,7293-5,7301,7314

DV tag = ONLV_2_1_6

MCset: Runs = 5141-3

Smearing version = FILTERED

D.1.3 62.4 GeV data

Dataset: Year = PR04

Runs = 14313,14442,14444,14447-8,14583

DV tag = ONLV_5_1_0

MCset: Runs = 11250-65,11280

Smearing version = SMV4LE_1

D.2 Tracklet reconstruction plots

The figures in this Section are used only for illustration of a point. They are not used for the final data results. 200 and 62.4 GeV data is used.

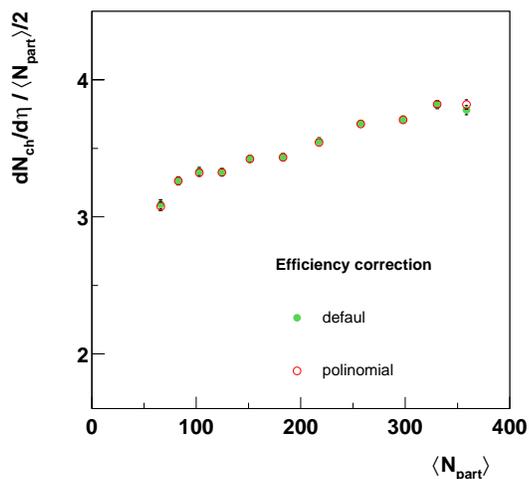


Figure 78. Data reconstruction with the default efficiency and using polynomial. Centrality is Paddle based, results are only for illustration (not final) for 200 GeV.

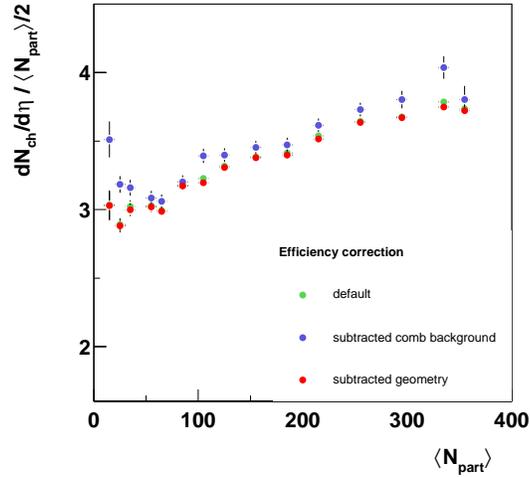


Figure 79. Data reconstruction with the default efficiency and subtracting geometry or combinatorial background. Centrality is Paddle based, results are only for illustration (not final) for 200 GeV. The statistical error for subtracting background case is significant.

D.3 Correction factors

The value of the correction factor α' can be split in three components: a correction for the geometrical acceptance (acc)¹, a correction for background coming from secondary interactions and weakly decaying particles (s+w) and a correction for the combinatorial background. α' and α values (from Chapter 4) are shown in Table XI for the z -vertex position 0 and OHB number 10. The uncertainty on the values for the correction components is a combination of statistical uncertainty and rounding errors, which has a maximum of 5%.

¹this splitting is not precise, for example the tracklet reconstruction efficiency is convoluted in these factors and depends on the Search method

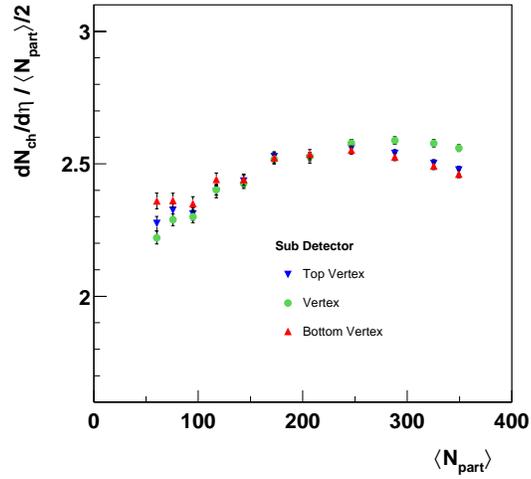


Figure 80. Data reconstruction using the Top and Bottom Vertex detectors individually, 62.4 GeV.

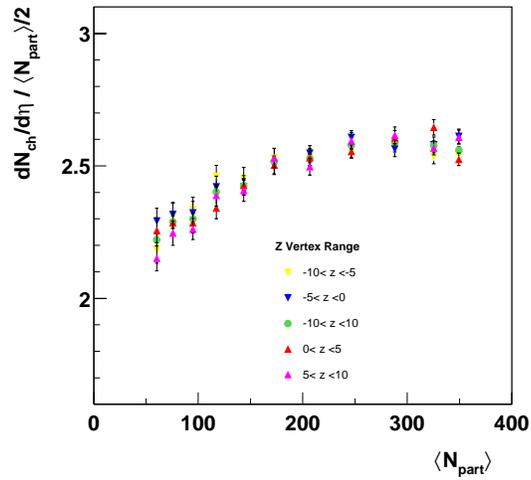


Figure 81. Data reconstruction for different vertex ranges for the collision vertex, 62.4 GeV.

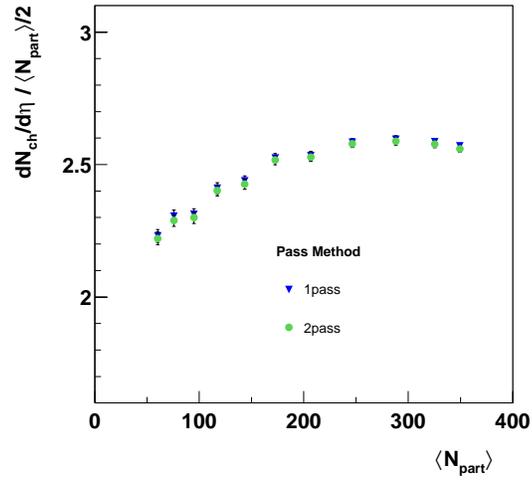


Figure 82. Data reconstruction for Search Outer Vertex method with 1pass and 2pass condition, 62.4 GeV.

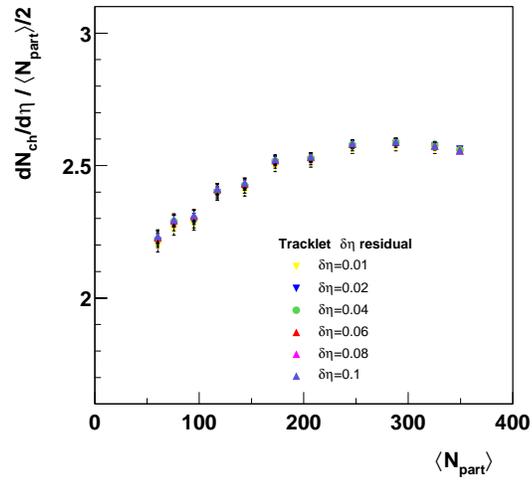


Figure 83. Data reconstruction for different values of the $d\eta$ cut on tracklet residuals, 62.4 GeV.

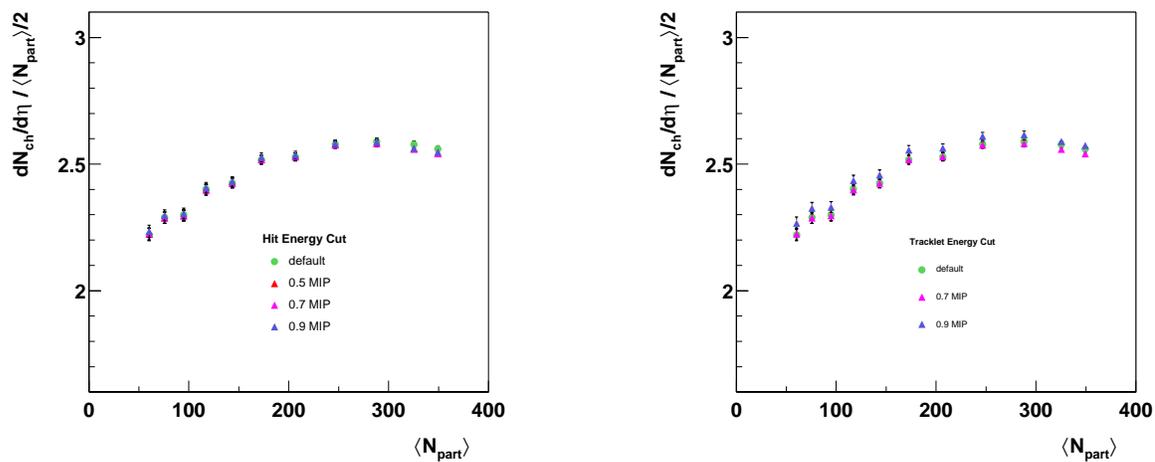


Figure 84. Data reconstruction for different values of the energy cut on the Vertex hits (left panel) and energy cut on the tracklets (right panel), 62.4 GeV.

Figure	Correction factor	value
Figure 37	$\alpha' = (\text{acc}) \times (\text{s+w}) \times (\text{comb})$	0.38
Figure 45	$\alpha = (\text{acc}) \times (\text{s+w})$	0.08
Figure 46	$\alpha' = (\text{s+w}) \times (\text{comb})$	2.02
Figure 46	$\alpha = (\text{s+w})$	0.44

TABLE XI

VALUES FROM DIFFERENT CORRECTION FACTORS FOR Z-VERTEX 0 CM AND OHB 10.

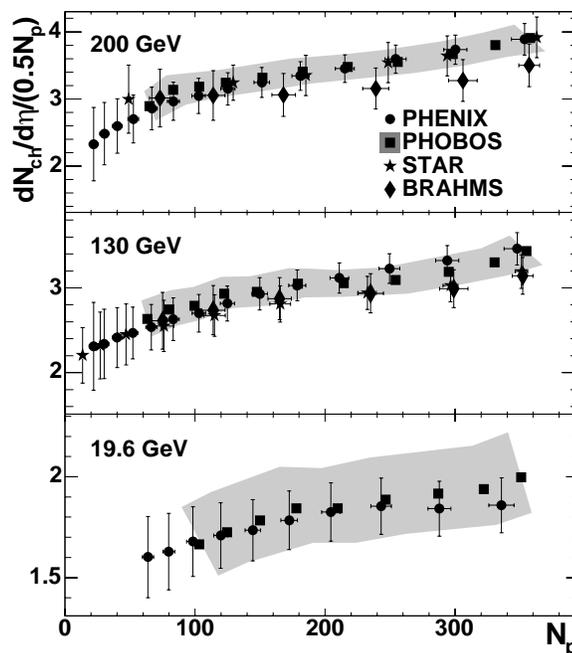


Figure 85. Charged particle multiplicity per participant pair as a function of $\langle N_{part} \rangle$ for $\sqrt{s_{NN}} = 200, 130$ and 19.6 GeV from all RHIC experiments. Compilation from (73).

Analyzing the data in Table XI it is possible to derive the individual components of the correction: (acc)=0.19, (s+w)=0.44 and (comb)=4.60.

D.4 Au+Au results from RHIC experiments

The agreement between the charged particle multiplicity results obtained by all four experiments confirms the high quality of physics carried out in RHIC. In Figure 85 the results from BRAHMS, PHENIX, PHOBOS and STAR experiments are presented for 200 and 130 GeV and 19.6 GeV. PHOBOS data is combined from Vertex and Spectrometer tracklets for 200 and 130 GeV and combined preliminary from Vertex tracklets and Octagon multiplicity analyses for 19.6 GeV.

Comparison with results from WA98 at 17.2 GeV Pb+Pb collisions is shown in (62).

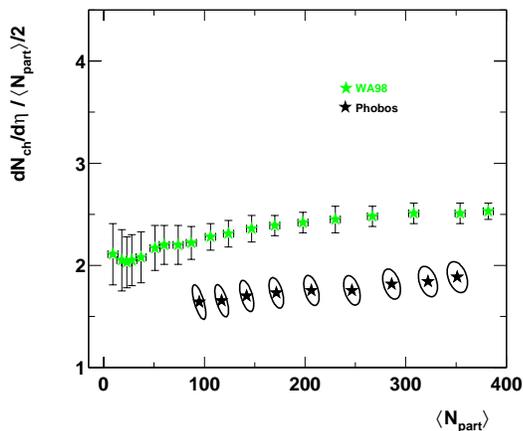


Figure 86. Charged particle multiplicity per participant pair as a function of $\langle N_{part} \rangle$ for $\sqrt{s_{NN}} = 19.6$ GeV (PHOBOS) and 17.2 (WA98) (62).

D.5 p+p data point for 19.6 GeV

The p+p point for 19.6 GeV is extrapolated using (60). The inelastic results is obtained from a log fit from $\sqrt{s}=23$ GeV to 200 GeV with errors estimated at 10% using the errors from the five central points in the presented $dN/d\eta$ distributions. The value doesn't change if the 200 GeV point is dropped.

D.6 Error ellipses

The mathematical derivation of the error ellipses that correspond to an error in $dN/d\eta$ and $\langle N_{part} \rangle$ is based on work from M.Baker (74). The shorter version is presented here¹ not only for further reference, but also as an example how the experimentalist should use proper evaluation of errors.

¹hopefully, without introducing errors

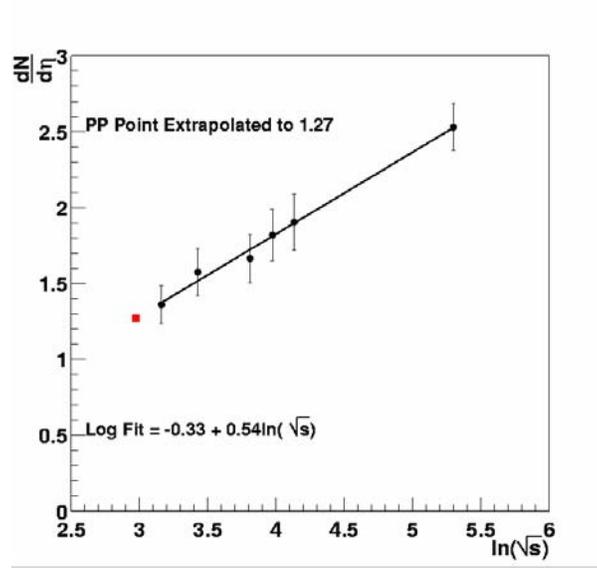


Figure 87. Extrapolation of the p+p result for 19.6 GeV.

D.6.1 General transformation of correlated normal errors in two variables

The covariance matrix is a general description of the error of two variables x and y :

$$\begin{pmatrix} \sigma_x^2 & \sigma_{xy} \\ \sigma_{yx} & \sigma_y^2 \end{pmatrix} \quad (\text{D.1})$$

where $\sigma_x^2 = \langle (x - \bar{x})^2 \rangle$, $\sigma_y^2 = \langle (y - \bar{y})^2 \rangle$, $\sigma_{xy} = \sigma_{yx} = \langle (x - \bar{x})(y - \bar{y}) \rangle$.

The transformation to new variables u and v is given by:

$$\begin{pmatrix} \sigma_u^2 & \sigma_{uv} \\ \sigma_{vu} & \sigma_v^2 \end{pmatrix} = \begin{pmatrix} \left(\frac{\partial u}{\partial x}\right)_y & \left(\frac{\partial u}{\partial y}\right)_x \\ \left(\frac{\partial v}{\partial x}\right)_y & \left(\frac{\partial v}{\partial y}\right)_x \end{pmatrix} \begin{pmatrix} \sigma_x^2 & \sigma_{xy} \\ \sigma_{yx} & \sigma_y^2 \end{pmatrix} \begin{pmatrix} \left(\frac{\partial u}{\partial x}\right)_y & \left(\frac{\partial v}{\partial x}\right)_y \\ \left(\frac{\partial u}{\partial y}\right)_x & \left(\frac{\partial v}{\partial y}\right)_x \end{pmatrix} \quad (\text{D.2})$$

which leads to the equations for the variance of the new variables:

$$\sigma_u^2 = \sigma_x^2 \left(\frac{\partial u}{\partial x} \right)_y^2 + 2\sigma_{xy} \left(\frac{\partial u}{\partial x} \right)_y \left(\frac{\partial u}{\partial y} \right)_x + \sigma_y^2 \left(\frac{\partial u}{\partial y} \right)_x^2 \quad (\text{D.3})$$

$$\sigma_v^2 = \sigma_x^2 \left(\frac{\partial v}{\partial x} \right)_y^2 + 2\sigma_{xy} \left(\frac{\partial v}{\partial x} \right)_y \left(\frac{\partial v}{\partial y} \right)_x + \sigma_y^2 \left(\frac{\partial v}{\partial y} \right)_x^2 \quad (\text{D.4})$$

$$\sigma_{uv} = \sigma_x^2 \left(\frac{\partial u}{\partial x} \right)_y \left(\frac{\partial v}{\partial x} \right)_y + \sigma_{xy} \left[\left(\frac{\partial u}{\partial x} \right)_y \left(\frac{\partial v}{\partial y} \right)_x + \left(\frac{\partial v}{\partial x} \right)_y \left(\frac{\partial u}{\partial y} \right)_x \right] + \sigma_y^2 \left(\frac{\partial u}{\partial y} \right)_x \left(\frac{\partial v}{\partial y} \right)_x \quad (\text{D.5})$$

The inverse transformation has the same form:

$$\sigma_x^2 = \sigma_u^2 \left(\frac{\partial x}{\partial u} \right)_v^2 + 2\sigma_{uv} \left(\frac{\partial x}{\partial u} \right)_v \left(\frac{\partial x}{\partial v} \right)_u + \sigma_v^2 \left(\frac{\partial x}{\partial v} \right)_u^2 \quad (\text{D.6})$$

$$\sigma_y^2 = \sigma_u^2 \left(\frac{\partial y}{\partial u} \right)_v^2 + 2\sigma_{uv} \left(\frac{\partial y}{\partial u} \right)_v \left(\frac{\partial y}{\partial v} \right)_u + \sigma_v^2 \left(\frac{\partial y}{\partial v} \right)_u^2 \quad (\text{D.7})$$

$$\sigma_{xy} = \sigma_u^2 \left(\frac{\partial x}{\partial u} \right)_v \left(\frac{\partial y}{\partial u} \right)_v + \sigma_{uv} \left[\left(\frac{\partial x}{\partial u} \right)_v \left(\frac{\partial y}{\partial v} \right)_u + \left(\frac{\partial y}{\partial u} \right)_v \left(\frac{\partial x}{\partial v} \right)_u \right] + \sigma_v^2 \left(\frac{\partial x}{\partial v} \right)_u \left(\frac{\partial y}{\partial v} \right)_u \quad (\text{D.8})$$

D.6.2 In the case of tracklets

Variables are: $u = x = \langle N_{part} \rangle$, $v = 2dN/d\eta$ and $y = v/u = (dN/d\eta)/(\langle N_{part} \rangle/2)$. The derivatives are:

$$\begin{aligned} \left(\frac{\partial x}{\partial u} \right)_v &= 1 \\ \left(\frac{\partial x}{\partial v} \right)_u &= 0 \\ \left(\frac{\partial y}{\partial u} \right)_v &= -\frac{v}{u^2} \\ \left(\frac{\partial y}{\partial v} \right)_u &= \frac{1}{u} \end{aligned} \quad (\text{D.9})$$

The u and v covariance matrix elements are:

$$\begin{aligned}\sigma_u^2 &= \sigma_{\langle N_{part} \rangle}^2 \\ \sigma_v^2 &= 4\sigma_{dN/d\eta}^2 \\ \sigma_{uv} &= 0\end{aligned}\tag{D.10}$$

Using the equations from the previous Section the x and y covariant matrix elements are:

$$\begin{aligned}\sigma_x^2 &= \sigma_u^2 \\ \sigma_y^2 &= \sigma_u^2 \left(-\frac{v}{u^2}\right)^2 + \sigma_v^2 \left(\frac{1}{u}\right)^2 \\ \sigma_{xy} &= \sigma_u^2 \left(-\frac{v}{u^2}\right)\end{aligned}\tag{D.11}$$

or (the final expression for these elements):

$$\begin{aligned}\sigma_x^2 &= \sigma_{\langle N_{part} \rangle}^2 \\ \sigma_y^2 &= y^2 \frac{\sigma_{\langle N_{part} \rangle}^2}{\langle N_{part} \rangle^2} + 4 \frac{\sigma_{dN/d\eta}^2}{\langle N_{part} \rangle^2} \\ \sigma_{xy} &= -\frac{y}{\langle N_{part} \rangle} \sigma_{\langle N_{part} \rangle}^2\end{aligned}\tag{D.12}$$

D.6.3 Drawing an error ellipse from a 2 x 2 covariance matrix

The rotation angle α , which transforms from (x, y) to a new set of coordinates in which the covariance matrix is diagonal, is not zero if the σ_{xy} element is non-zero (this is true for the general case). The new coordinates are oriented in the direction of the semi-major and semi-minor axes of the ellipse and the angle α is the tilt of the ellipse with respect to the x, y axes. In this solution $-\frac{\pi}{4} < \alpha < \frac{\pi}{4}$ and λ_1 is the

largest of the two eigenvalues. It is close to the original x coordinate only if $\sigma_x > \sigma_y$, which holds for this case where $\langle N_{part} \rangle$ is usually two orders of magnitude larger than $dN/d\eta/\langle N_{part} \rangle/2$.

$$\begin{aligned}
 \lambda_1 &= \frac{1}{2} \left[\sigma_x^2 + \sigma_y^2 + \sqrt{(\sigma_x^2 - \sigma_y^2)^2 + 4\sigma_{xy}^2} \right] \\
 \lambda_2 &= \frac{1}{2} \left[\sigma_x^2 + \sigma_y^2 - \sqrt{(\sigma_x^2 - \sigma_y^2)^2 + 4\sigma_{xy}^2} \right] \\
 \alpha &= \frac{1}{2} \tan^{-1} \left(\frac{2\sigma_{xy}}{\sigma_x^2 - \sigma_y^2} \right)
 \end{aligned} \tag{D.13}$$

D.7 Calculating the effective collision area

The segment (area) of a circle of radius R is used to find the overlap area of two colliding nuclei:

$$area = 2 \times Area_{\frac{1}{2}segment} = 2 \times \frac{1}{2} R^2 (\theta - \sin \theta) \tag{D.14}$$

where $\theta = 2\arccos(b/2R)$. The parameters R and b vary as a function of centrality, see Glauber plot in Chapter 2.

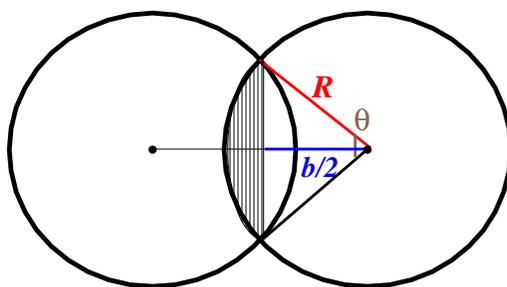


Figure 88. Schematic collision of two nuclei (circles). The area of overlap is calculated using the formula for the area of a segment (shaded area). R is the radius of the nucleus, b is the impact parameter and θ is the angle defining the segment.

Appendix E

TRIGGER INSPECTOR

The Trigger Inspector was introduced during the $d + Au$ run in order to analyze the trigger performance and its reliability after the data is taken on a run by run basis. Later, it was expanded to provide information about the beam quality, included checks for selecting uniform event samples and centrality classes over the whole range of the data.

The primary use is to check all trigger detectors for proper operation. The performance of the trigger logic (trigger bits and latches) are also checked. The Inspector provides all calibration information from the trigger detectors which is later fed into the event selection and centrality variables.

The input information to the Inspector is provided by the PHOBOS Data Production system which initially processes the trigger data into a ROOT tree format. During the data taking the Inspector checks for incoming data trees and automatically analyzes each run. The setup for the Inspector is done at the start of each collision system run (e.g. PR03 $d + Au$), to ensure that all new changes in the trigger system are appropriately reflected in the software. The output information for each run is saved in a file.

Due to the complexity of the collected information by the Inspector, a daily (expert) evaluation of this information is needed. The trigger performance is checked by executing a set of plotting macros which show the information for all data or just for a specific subset. The expert assesses whether any observed changes or shifts are correlated with known changes to the trigger system (e.g. a change of trigger configuration). If a problem is found, the trigger group is notified to resolve it. If everything is found to be correct, all calibrations and other information are provided for the event selection analysis.

E.1 Trigger detectors

The following explanation is for the Paddle counters but similar checks are performed for each of the other trigger detectors.

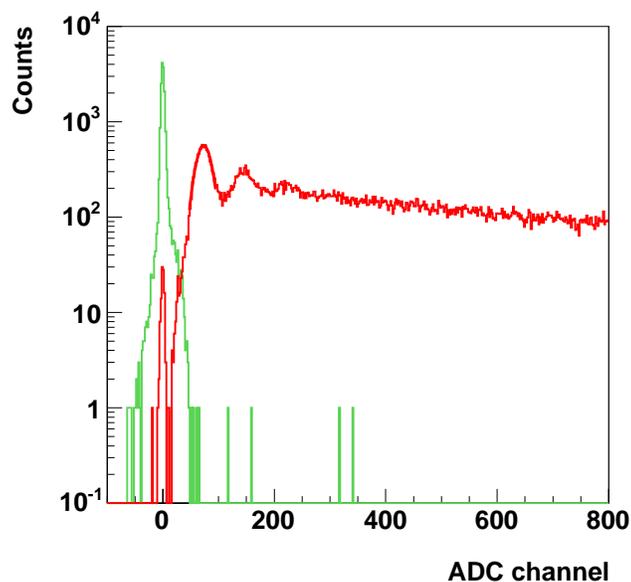


Figure 89. The pedestal (green) and MIP position (red) from a Paddle counter in the Cu+Cu 200 GeV data. This is for Paddle Positive 16.

All ADC (Amplitude to Digital Converter) signals are checked. Information is collected for the pedestals, first MIP, second MIP and the end point of the distribution for all counters. The PHOBOS convention for Positive and Negative side holds, see Figure 90. The Paddles have 8192 channel ADC's.

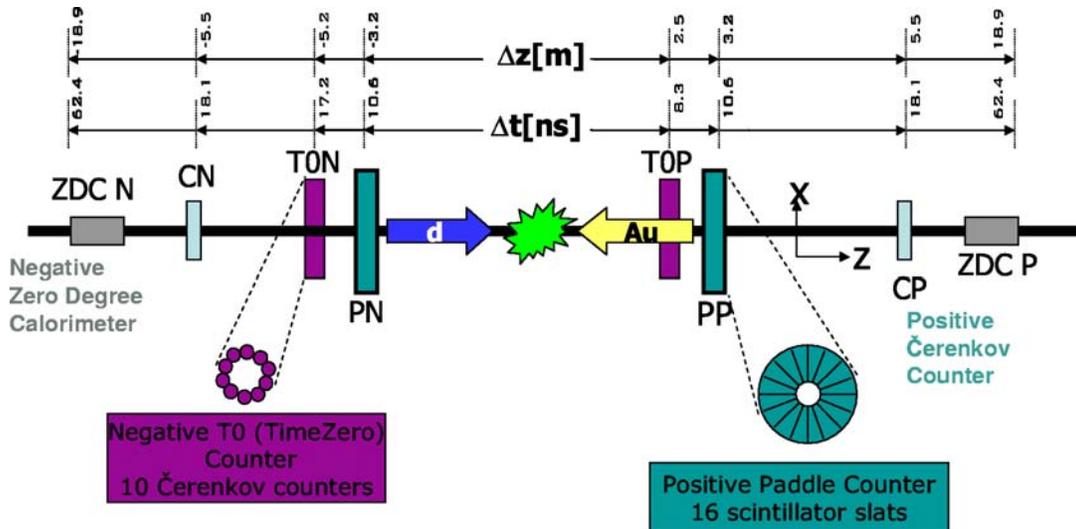


Figure 90. Schematic representation of the trigger detectors, Negative and Positive convention, for the PR03 d+Au run. Distances and times to the detectors, relative to the interaction point, are shown. Gold ions move in the direction of the yellow beam.

In Figure 89 the distribution is shown up to channel 800. The width of the pedestal (green) corresponds to the noise of the detector. First, second and third MIP positions (red) are visible.

The fraction of events during which a counter records a TDC and/or an ADC signal is monitored for all Paddle counters (similarly for no TDC and/or ADC signals). Ideally, every time there is a signal from TDC, there should be signal present from the ADC. Figure 91 shows these fractions for one Paddle counter. These fractions depend on the triggering configuration, e.g. in case of triggering primarily on TOs, the fractions can change. Only TDC signals with no ADC signal (and vice-versa) are considered as undesirable, as this could cause mis-triggering.

Collisions are distinguished from beam-gas interactions by the Paddle time difference measured in each event. This is determined from the time difference between the logical OR of the Paddle counters on the Positive and Negative side. Paddle time difference distribution needs to be defined such that zero

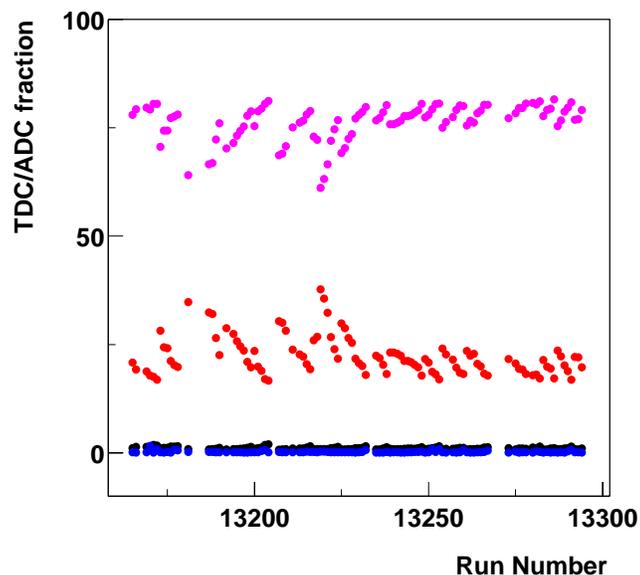


Figure 91. TDC and ADC fractions for Paddle Positive 5, Au+Au 200 GeV PR04. ADC without TDC signal (black), TDC without ADC (blue), ADC and TDC signal (pink), No TDC and No ADC signal (red) are shown.

corresponds to the center of the detector, as a tight cut is used on this variable for the event selection. The centering of the distribution during PR04 run was determined from the relative difference of the Paddle time difference to a collision position calculated from silicon vertex algorithm. Alternatively, this could be performed using the beam gas peaks. However, due to the small fractions of minimum bias data triggered for the majority of the data, this became unreliable. Times from the individual Paddle counters equalized in time have been monitored since the PR04 run, see Figure 92. Single arm times from the OR are shown for the Positive side counters. They are very stable, see Figure 93. This is another important information which forms the decision for good collision event.

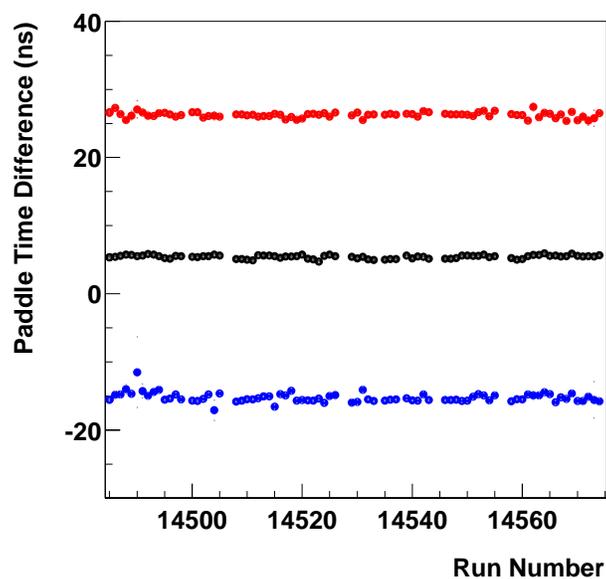


Figure 92. Paddle time difference monitored by the Inspector, range of runs from Au+Au 200 GeV. Collision peak (Positive-Negative) (black), Positive background peak (red), Negative background peak (blue) are shown.

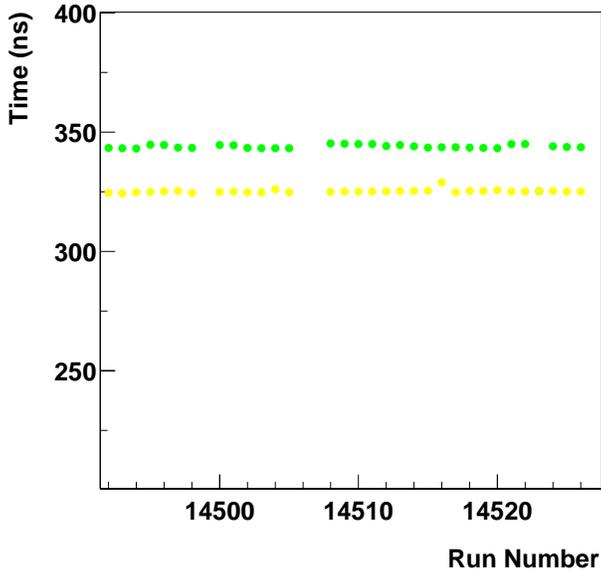


Figure 93. Paddle time for the Positive side monitored by the Inspector, range of runs from Au+Au 200 GeV. Collision peak (red) and background peak (yellow) are shown.

E.2 Data quality

Data quality checks performed by the Inspector are used as a first signal for the amount of “good” data collected. As an example, the average x and y position of the events in each run, known as the *Beam Orbit*, is shown in Figure 94. This information is important for almost all analyses. Ideally, positions closest to 0.0 cm in both x and y is optimal for the geometrical acceptance of the detectors. The restriction of the z -vertex range of the collected events by the TAC is tracked over the whole data taking, see Figure 95, and should be constant in order to select the optimal vertex range for various analyses.

More complex checks for the quality of the data are also performed. Fraction of data flagged by each bit at L0 and L1 trigger decisions is very important for the trigger performance. An example for some of the L1 latches are shown in Figure 16. The fraction of data which passes the collision requirements as well as fraction of “bad” data let through by the trigger can be seen in Figure 96. The fraction of the good data within a valid z -vertex range which will pass the collision requirements is shown in green. This fraction depends on both the trigger configuration and on the beam conditions, e.g at the beginning of some stores the fraction of good events is 10% lower compared to that at the end.

The Inspector can give an estimate for the total number of taken events. Figure 97 shows the total number of events for different polarities during the Au+Au PR04 running, which lasted 3 months. In 88 days of data production total of 257 million events were written to tape. Approximately 15% (38 milion) of them are good collision events¹.

¹defined as a collision AND with a beam orbit within 2.5 mm of the center; a higher fraction could be considered if this beam orbit condition is relaxed

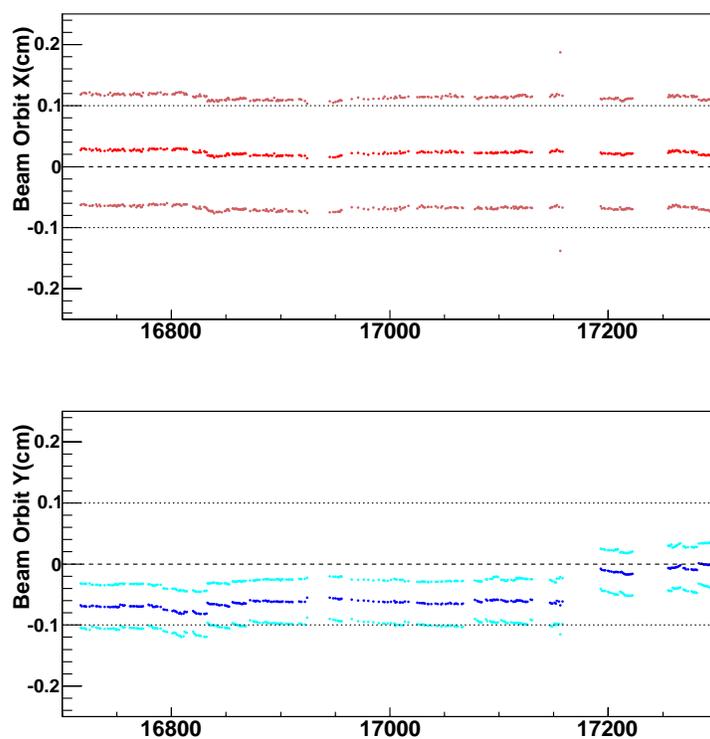


Figure 94. The average x and y positions of the events versus run for the PR05 Cu+Cu 200 GeV data. The symbols represent the average vertex position and $1\text{-}\sigma$ limits on the distribution. The dashed lines are defining the optimal vertex position of 0.0 cm within 0.1 cm.

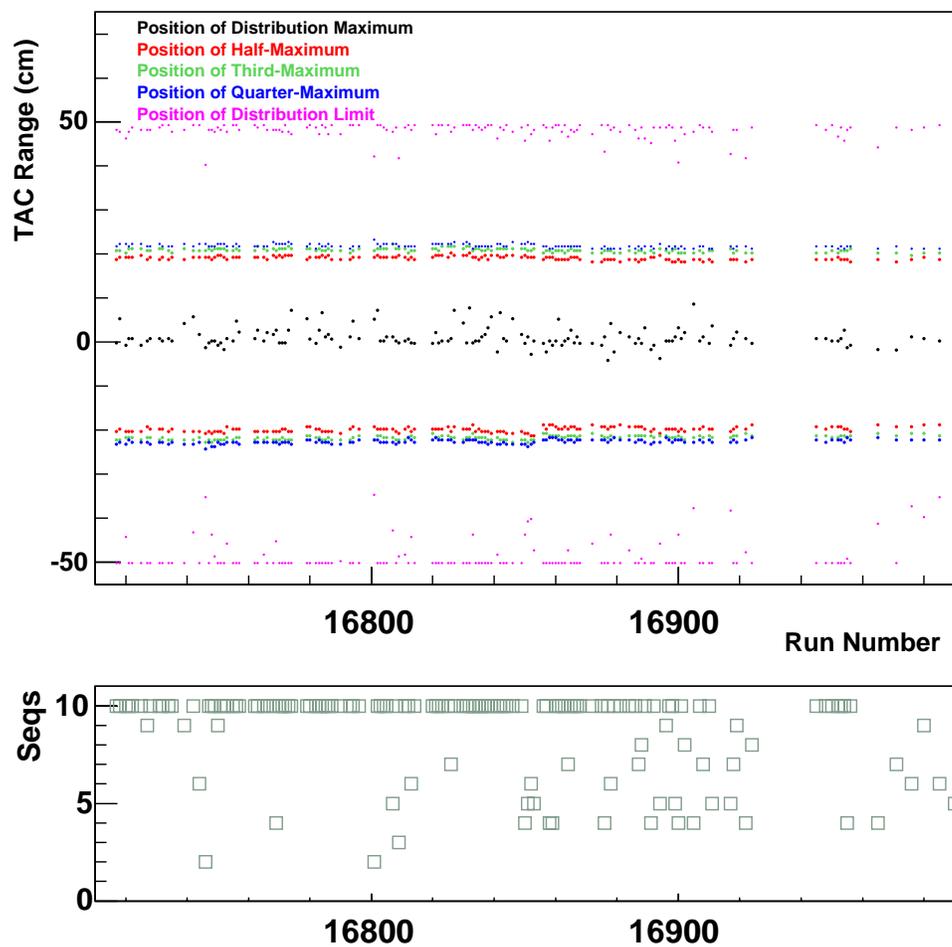


Figure 95. The top panel shows the z -vertex range of the events written to tape, as selected by the TAC, over a range of runs for PR05 Cu+Cu 200 GeV data. The mean position (black), position at half of the distribution maximum (red), and others (as denoted on the plot) are monitored. Bottom panel shows the number of sequences from which the information was extracted. One sequence contains approximately 10000 events.

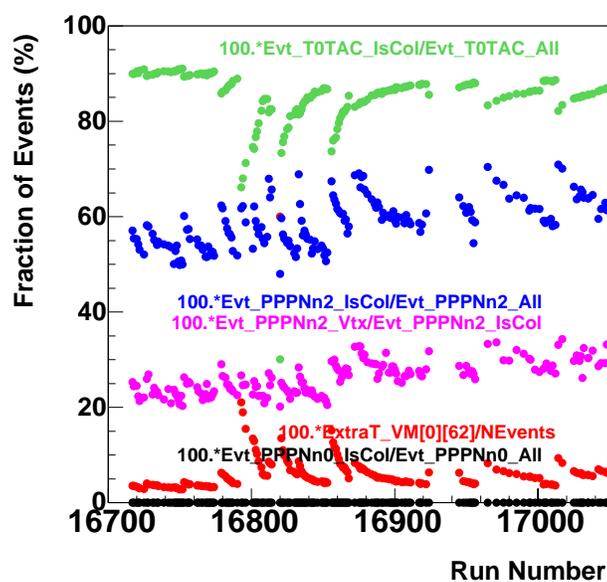


Figure 96. The fraction of good events within the z -vertex from the TAC (green), as monitored by the Inspector for Cu+Cu 200 GeV data. The amount of good events is sensitive to the beam conditions. It can be clearly seen that at the beginning of one accelerator store this fraction can be less compared to that at the end. Other colored markers correspond to the fraction of good events compared to a specific trigger.

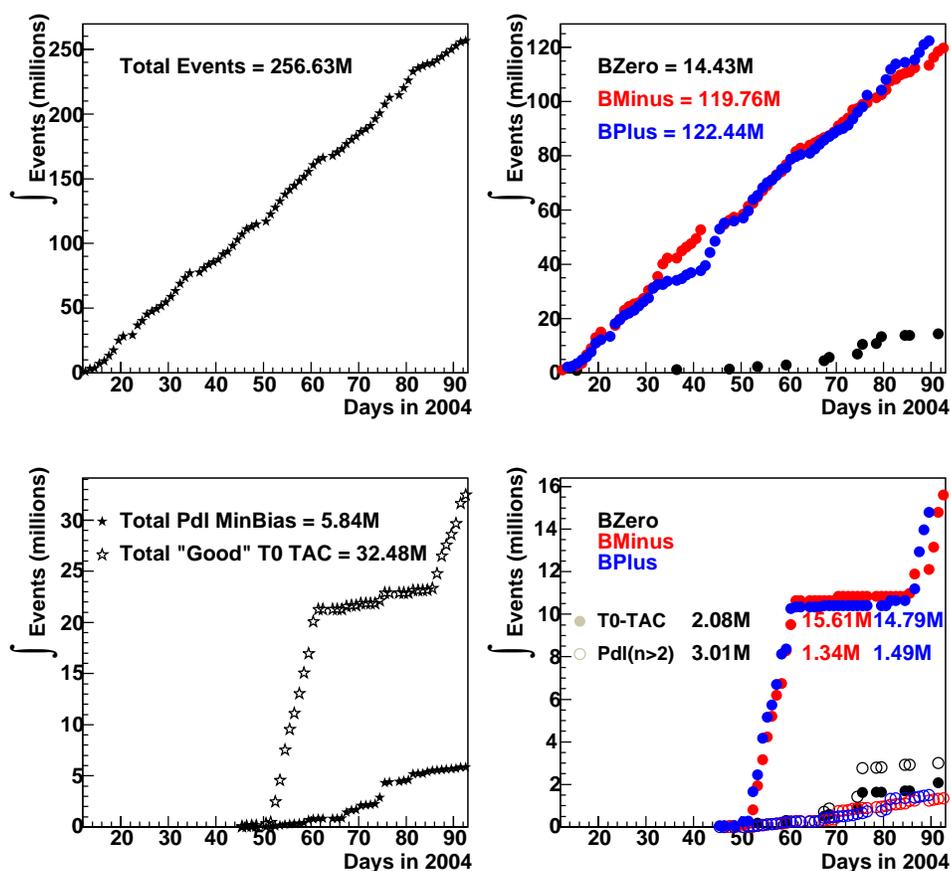


Figure 97. Estimate for the total number of events taken by PHOBOS during the Au+Au PR04 run. The top panels show the total number (left) and split by magnetic polarity (right). Bottom panels represent the estimate for total good events within valid z -vertex range as determined by the TAC and by the minimum bias trigger (left) and split by magnetic polarity (right).

Appendix F

N_{part} SYSTEMATIC STUDIES

This Appendix presents work on determining the systematic errors associated with N_{part} for the d+Au centrality analysis.

F.1 How can we measure N_{part} ?

In any experiment N_{part} cannot be measured directly. An assumption is made that some measured quantity in data correctly reflects the collision geometry. This quantity has to be chosen with great care. As an example, a quantity proportional to the minimum ionizing energy signal in the Octagon detector ($-3 < \eta < 3$) is considered: EOct. N_{part} is calculated using theoretical models. In Monte-Carlo (MC) simulations, the centrality variable (EOct) is mapped to the calculated N_{part} given by the model (see Figure 98). The connection between the data and MC comes from the equivalent cross-sectional fraction of the EOct variable (e.g. most central 10%) in both samples. The N_{part} from the MC can be associated to the data. This Appendix describes the uncertainty in this mapping.

F.2 Obtaining N_{part} for d+Au collisions

From MC studies, a monotonic dependence between N_{part} and EOct is found, shown in Figure 98. The unbiased MC distribution in Figure 99 (left panel) represents the full geometrical cross-section. It is divided into percentile bins of cross-section, six bins in the figure. The corresponding data and MC distribution (with the same bias as the data applied) match reasonably well¹, see the right panel. The percentile cut positions (for the data) are found by multiplying the cut positions found for the MC by

¹for this case a scale factor is applied to MC to match the data in the highest yield region, the values is approximately 1.06

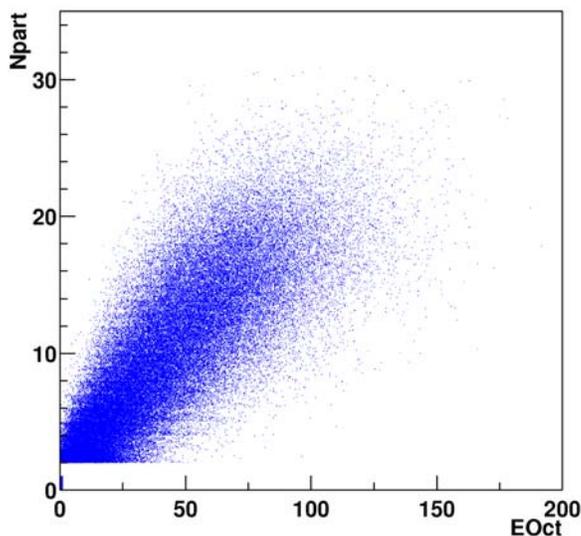


Figure 98. N_{part} and EOct correlation in MC.

the same scale factor (1.06) that matched the distributions. The values $\langle N_{part} \rangle$ are extracted for each bin in the biased MC sample. Figure 100 shows the found $\langle N_{part} \rangle$ values along with the distribution widths.

F.3 Systematic errors on $\langle N_{part} \rangle$

Differently triggered events introduce distinct *Trigger Biases*, which if not properly accounted for can introduce error in the estimated $\langle N_{part} \rangle$ values.

Paddle and T0 counters are used to create PHOBOS basic L0 triggers. The naming convention used in PHOBOS is as follows:

Paddle Single arm triggers require at least one hit in either the Positive or Negative Paddle counters, in coincidence with the Crossing Clock (CC).

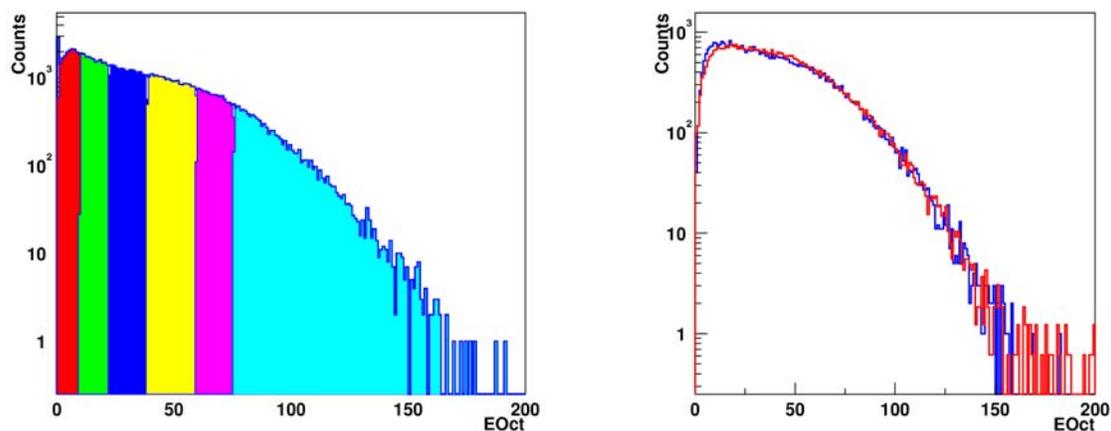


Figure 99. The unbiased MC distribution is sliced in percentile bins of cross-section. On the plot most central bin is in cyan (0-10 % central) and most peripheral is in red (100-80%). In the right panel, data and MC (biased as data) are matched by applying some scale factor along x -axis to the MC distribution.

PPIIPNSingle: Positive OR Negative Paddle Single Arm.

Paddle two arm triggers flag events with at least one hit in each Paddle counter +CC.

PP&PN: Positive AND Negative Paddle Two Arms trigger. Narrow Paddle coincidence removes most of the background events.

The same naming convention as for the Paddle counters is applied for the T0s.

T0P&T0N: Positive AND Negative T0 Two Arms trigger. Narrow T0 coincidence removes most of the background events.

For the $\langle N_{part} \rangle$ values obtained for a particularly triggered data, the bias should be appropriately accounted for, as it represents the missed part of the cross-section. The same statement is valid for any vertex bias. In the d+Au data a silicon vertex algorithm provided a clean data sample. As can be seen

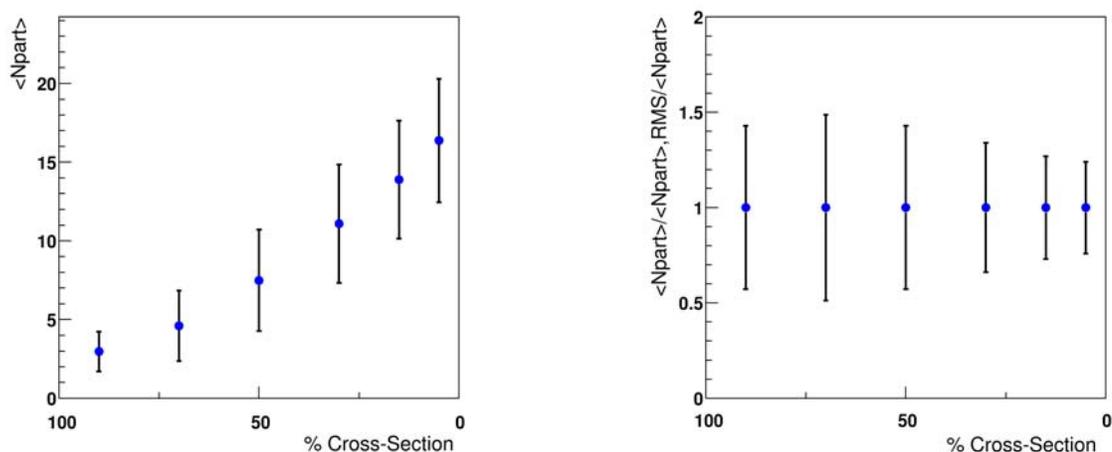


Figure 100. The averaged N_{part} values and the width of the percentile cross-section bins for d+Au. 100% corresponds to peripheral, 0% to central events.

from Figure 101 and Table XII adding the vertex requirement to this trigger ¹ results in an efficiency of $\approx 82\%$. The overall efficiency was calculated from shape matching the EOct distributions. Shape matching data to Glauber EOct distributions (Section F.5) gave an upper limit for the uncertainty of the above value of the order of 10%. When MC (with Trigger+Vertex bias) was compared to MC without bias, the effect was largest for the peripheral bins, see Figure 102.

Over- or under-estimating the event selection efficiency from MC with comparison to the data has an effect on the percentile cross-section cut positions when slicing the EOct distribution. When efficiency was varied up to $\pm 5\%$ the observed effects on the central bins were small. The effects on the peripheral bins are cumulative and therefore become large for peripheral bins.

¹The trigger used in the example here is **PP&PN**

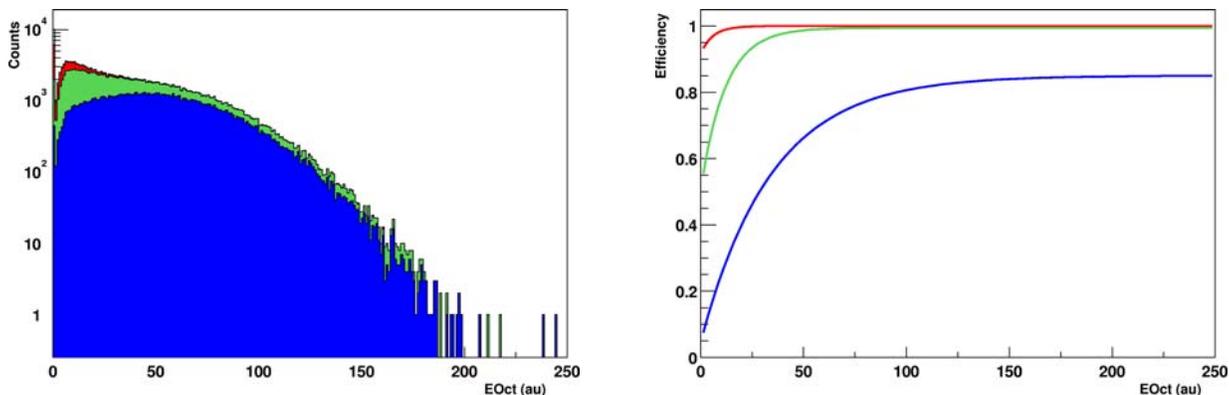


Figure 101. Simulated effects on EOct distribution from different triggers: all MC events (black, difficult to see), *PPIIPNSingle* (red), *PN&PP* (green) and *T0N&T0P* (blue). Efficiencies for these triggers are shown in the right panel and Table XII. *PN&PP + Vertex* bias is not shown in the plots.

F.4 HIJING MC studies

Simulated EOct includes effects from electronic noise and spatial (vertex) distribution. These smearing effects can be seen when the $\langle N_{part} \rangle$ are extracted from the HIJING EOct distribution and from a “true” distribution defined from dividing the N_{part} distribution itself, see Figure 103. Smearing has the largest effect on the most central and peripheral bins, owing to the fact that there is no smearing into these bins from *MORE* central and *MORE* peripheral bins respectively.

$\langle N_{part} \rangle$ were compared for two HIJING versions with different nuclear density profiles for the deuteron, the Woods-Saxon and the Hulthen functions. As can be seen from Figure 104, there are very small differences for the derived $\langle N_{part} \rangle$ values from these versions¹.

¹the Hulthen used here represents the wrongly defined function in the HIJING model, this was later corrected (by the HIJING authors), where the N_{part} distribution was found to be much closer to the one obtained from the Woods-Saxon

Simulated	Efficiency(Overall Event Selection)
All MC events (black)	100%
PPIIPNSingle (red)	97%
PN&PP (green)	91%
TON&TOP (blue)	51%
PN&PP+Vertex	82%

TABLE XII

TRIGGER EFFICIENCIES.

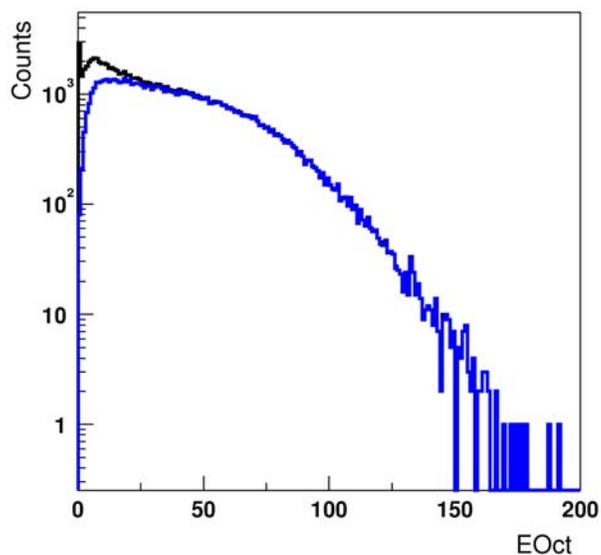


Figure 102. Trigger and Vertex bias effect on MC. The black histogram represents the unbiased MC, the blue histogram is the MC with Trigger and Vertex biased applied. A bias is only seen for the peripheral data.

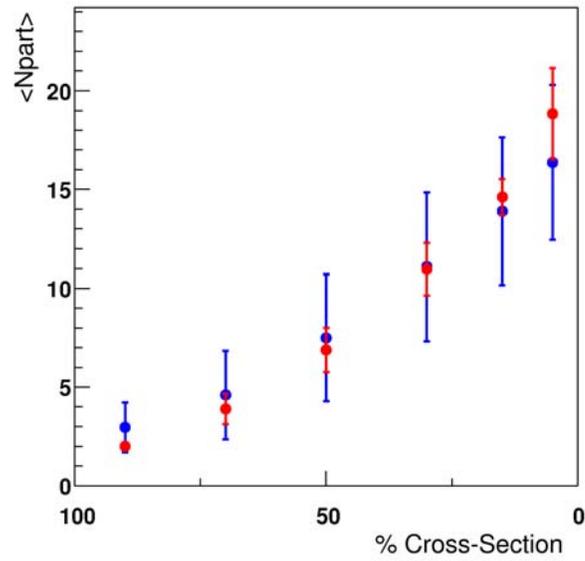


Figure 103. Smearing effects on $\langle N_{part} \rangle$. The difference between $\langle N_{part} \rangle$ found from a divided EOct distribution (blue) and from a divided N_{part} distribution (red).

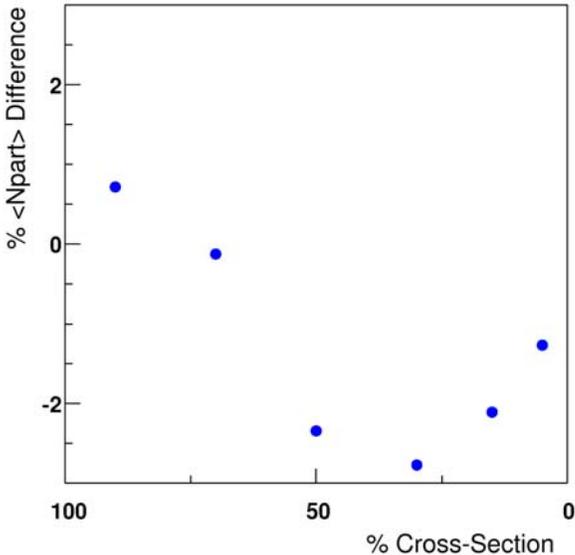


Figure 104. Difference between $\langle N_{part} \rangle$ values from HIJING with a Wood-Saxon and a Hulthen nuclear density profiles for the deuteron.

F.5 Glauber MC studies

HIJING uses MC similar to the Glauber multiple scattering model to calculate N_{part} . What if HIJING calculations are wrong? This Section outlines the studies performed with an N_{part} distribution derived directly from a Glauber model in order to check for any inconsistencies.

In the first case, Figure 105, the distribution from the HIJING EOct and the N_{part} distribution from the Glauber MC¹ are compared. The distributions do not match well here. The $\langle N_{part} \rangle$ values for the most central and peripheral bins obtained from Glauber are different from those in HIJING. However, this case is not realistic, some smearing must be added into the Glauber N_{part} distribution to mimic HIJING EOct.

Smearing is introduced to Glauber N_{part} distribution, see Figure 105 (Case2), in the form of “Gaussian noise”. The amount of smearing increases with N_{part} value as Equation F.1, where S is a random number defined from a gaussian distribution with width $\sqrt{N_{part}}$. A scan was performed for different parameters p . The smearing was closest to that in HIJING EOct for $p \approx 1$.

$$f(N_{part}) = N_{part} + p \times S \quad (\text{F.1})$$

In the third case, additional term proportional to N_{coll} was added to the Glauber N_{part} distribution². After scanning for different parameters, the closest match between the distributions from Glauber MC and HIJING was found. The $\langle N_{part} \rangle$ still deviates from that in HIJING for the peripheral bin. This is the reason that the Trigger and Vertex bias (Figure 105, Case4), which mostly affects the peripheral

¹the same study could be performed with comparison to data. In this case (d+Au), the EOct distributions from data and MC are very close.

²it is clear that the N_{part} is not linear with EOct. Since the nature of the additional source contributing to the EOct distribution is not understood, more scaling and smearing functions of different nature were tested.

$\langle N_{part} \rangle$ values, was also considered in the Glauber studies. Peripheral bins with the Trigger and Vertex bias have a larger $\langle N_{part} \rangle$. The $\langle N_{part} \rangle$ for the most peripheral (80-100%) bin increased by 5%. For the 60-80% bin and 40-60% bin (which have a smaller bias), the $\langle N_{part} \rangle$ increases by 3% and 1% respectively, compared to the unbiased case.

The studies with Glauber MC are used to test the effects on $\langle N_{part} \rangle$ from different sources in HIJING. They were used as an upper limit in determining the final systematic error on $\langle N_{part} \rangle$. In Table XIII an example of the final systematic errors on $\langle N_{part} \rangle$ is presented. The error is found from combining studies from Glauber and HIJING MC with the errors associated with the uncertainty in the estimated trigger efficiency.

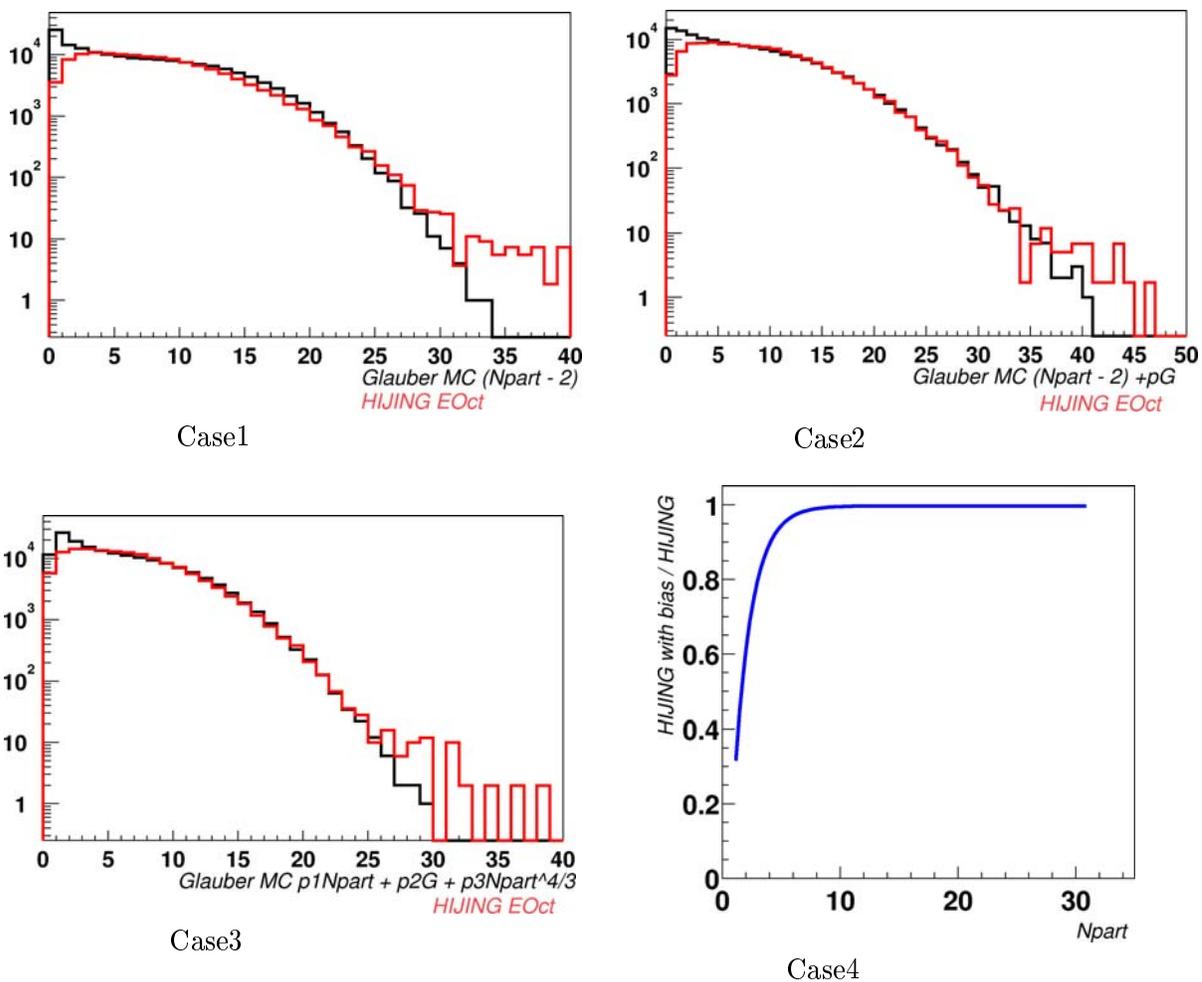


Figure 105. HIJING EOct with smearing (red) compared with Glauber N_{part} distribution (black) for different cases (see text). Case4 shows the Trigger+Vertex bias effect on N_{part} .

Centrality Bin	Errors (Glauber)	Errors (Efficiency)	Final Uncertainty (%)
100-80	14	16	22
80-60	11		
60-40	7		
40-20	5		
20-10	5	↓	↓
10-0	4	4	6

TABLE XIII

EXAMPLE OF THE FINAL SYSTEMATIC ERRORS ON $\langle N_{part} \rangle$ FOR D+AU AT 200 GEV. HERE, THE CROSS-SECTION IS SPLIT IN 6 BINS. 0-10% CORRESPONDS TO THE MOST CENTRAL COLLISIONS AND 100-80% TO THE PERIPHERAL COLLISIONS.

CITED LITERATURE

1. K.Adcox et al.: Measurement of the mid-rapidity transverse energy distribution from $\sqrt{s_{NN}} = 130$ GeV Au+Au collisions at RHIC. Phys.Rev. Letters, 87(052301), 2001. arXiv:nuclex/0104015.
2. Karsch, F.: Lattice results on QCD thermodynamics. Nucl. Phys. A, 698:199, 2002.
3. I.Arsene et al.: Quark gluon plasma and color glass condensate at RHIC? the perspective from the BRAHMS experiment. submitted to Nucl.Phys.A, (nucl-ex/0410020), 2004.
4. Back, B. B. et al.: The PHOBOS perspective on discoveries at RHIC. Submitter to Nucl.Phys.A, 2004.
5. K.Adcox et al.: Formation of dense partonic matter in relativistic nucleus-nucleus collisions at RHIC: Experimental evaluation by the PHENIX collaboration. status of our program to create, detect and characterize quark-gluon plasma. Submitter to Nucl.Phys.A, (nuc-ex/0410003), 2004.
6. J.Adams et al.: Experimental and theoretical challenges in the search for the quark gluon plasma: The STAR collaboration's critical assessment of the evidence from RHIC collisions. Submitter to Nucl.Phys.A, (nucl-ex:0501009), 2004.
7. One event in the STAR detector. www.star.bnl.gov.
8. J.D.Bjorken: Highly relativistic nucleus-nucleus collisions: The central rapidity region. Phys. Rev. D, 27(1):140–151, 1983.
9. Wang, X. N. and Gyulassy, M.: Energy and centrality dependence of rapidity densities at RHIC energies. Phys. Rev. Letters, 86(16), 2001.
10. K.J.Eskola: On predictions of the first results from RHIC. Nucl.Phys. A, 698:78–87, 2002.
11. M.E.Pescin and D.V.Schroedder: An introduction to a Quantum Field Theory. Perseus Books publishing, 1995.
12. S.Bethke: Determination of the QCD coupling α_s . arXiv:hep-ex/0004021.
13. P.Braun-Munzinger, K. and J.Stachel: Particle production in heavy ion collisions. arXiv:nucl-th/0304013.

14. M.Stephanov: QCD phase diagram and the critical point. Prog.Theor.Phys.Suppl, 153(hep-ph/0402115):139–156, 2004.
15. R.D.Pisarski and F.Wilczek: . Phys. Rev. D, 29(338), 1984.
16. Hagedorn, R.: . Nuovo.Cim.Suppl., 35:395, 1965. CERN 1983, Yellow Preprint TH 3684.
17. B.Tomasik and U.A.Wiedemann: Central and non-central HBT from AGS to RHIC. arXiv:hep-ph/0210250.
18. Particle Data Group. Eur. Phys.Journal C, 15(1-4), 2000.
19. R.J.Glauber: High-energy collision theory. Lectures on theoretical physics, I:314–414, 1956. Interscience, New York.
20. John J.Brehm, W. J.: Introduction to the structure of matter. John Wiley and Sons, 1989. eq:14-3.
21. Jager, C. et al.: . Atom. Data Nucl. Data Table, 36:495–623, 1987.
22. G. Dissertori, I. K. and Schmelling, M.: Quantum chromodynamics: High energy experiments and theory. Oxford, 2003.
23. Alner, G. J. et al.: Scaling of pseudorapidity distributions at c.m.energies up to 0.9 TeV. Z. Phys. C, 33:1–6, 1986.
24. H.U.Bengtsson and T.Sjostrand: Pythia. Comp.Phys.Commun., (46,43), 1987.
25. k.J.Eskola et al.: . Nucl.Phys.B, 570:379, 2000. hep-ph/9909456.
26. Gyulassy, M. and Wang, X. N.: A monte carlo program for parton and particle production in high energy hadronic and nuclear collisions. LBL-34246, 1997.
27. L.D.McLerran and R.Venugopalan: . Phys.Rev. D, 49:2233, 1994. hep-ph/9309289.
28. Ritter, H. G. and Wang, X. N.: Quark Matter 2004. IOP.
29. Wiedemann, U. A.: Theoretical overview QM'04. J.Phys.G, 30:S649, 2004.
30. Kharzeev, D. and M.Nardi: Hadron production in nuclear collisions at RHIC and high-density QCD. Phys. Lett. B, 507(1-4):121–128, 2001.
31. A.Bialas, M. and W.Czyz: Multiplicity distributions in nucleus-nucleus collisions at high energies. Nucl.Phys.B, (111):461–476, 1976.

32. B.Andersson, G. and B.Nilsson-Almqvist: A model for low- p_T hadronic reactions with generalizations to hadron-nucleus and nucleus-nucleus collisions. Nucl. Phys.B, 281(199 1-2):289–209, 1987.
33. Nilsson-Almqvist, B. and Stenlund, E.: Interactions between hadrons and nuclei: The Lund monte carlo-Fritiof v1.6. Comput. Phys. Commun., 43:387–397, 1987.
34. Gyulassy, M. and Wang, X. N.: Hijing version 1.35 is used. Comput. Phys. Commun., (83):307, 1994.
35. Kharzeev, D. and Levin, E.: Manifestation of high density QCD in the first RHIC data. Phys. Lett. B, 523(arXiv:nucl-th/0108006):79–87, 2001.
36. Back, B. B. et al.: The PHOBOS detector at RHIC. Nucl.Instrum. and Methods A, (499):603–623, 2003.
37. GEANT 3.21. CERN Program Library. Geneve.
38. Decowski, M. P.: Energy and Centrality Dependence of Mid-Rapidity Charged Particle Multiplicity in Relativistic Heavy-Ion Collisions. MIT, 2002.
39. Bindel, R. et al.: Array of scintillator counters for PHOBOS at RHIC. Nucl.Instrum. and Methods A, 474:38–45, 2001.
40. Adler, C. et al.: The RHIC zero-degree calorimeters. Nucl.Instrum. and Methods A, 470:488, 2001.
41. P. Kulinich, P. S. and Sukhanov, A.: The DAQ system with a RACEway switch for the PHOBOS experiment at RHIC. Nucl.Instrum. and Methods A, 499:603–623, 2003.
42. R.Nouicer et al.: Silicon pad detectors for the PHOBOS experiment at RHIC. Nucl.Instrum. and Methods A, 461:143–149, 2001.
43. Hollis, R. S.: Centrality Dependence of charged particle pseudorapidity distributions in Au+Au and d+Au collisions. UIC, 2005.
44. M.A.Reuter: Charged Particle Pseudorapidity Density Near Mid-rapidity in Ultrarelativistic Au+Au Collisions at RHIC. UIC, 2001.
45. Back, B. B. et al.: Centrality and pseudorapidity dependence of elliptic flow for charged hadrons in Au+Au collisions at $\sqrt{s_{NN}} = 200$ GeV. Submitted to Phys. Rev. C (Rapid Comm.), 2004.
46. K.Werner: The Venus event generator. Phys.Rep.C, 232:87, 1993.

47. R.Barlow: Systematic Errors: Facts and Fictions. The University of Manchester, 2004. arXiv:hep-ex/0207026.
48. Ph.R.Bevington: Data Reduction and Error Analysis for the Physical Sciences. McGraw Hill, 1969.
49. Elia, D. et al.: Energy dependence of K_s^0 and hyperon production at CERN SPS. J.Phys.G, 30, 2004. and references therein.
50. Back, B. B. et al.: Centrality dependence of charged particle multiplicity at midrapidity in Au+Au collisions at $\sqrt{s_{NN}} = 130$ GeV. Phys. Rev.C(R), 65, 2002. 31901.
51. Back, B. B. et al.: Centrality dependence of the charged particle multiplicity near mid-rapidity in au+au collisions at $\sqrt{s_{NN}}=130$ and 200 gev. Phys. Rev.C(R), 65, 2002. 061901.
52. For final 62.4 GeV results and ratios with other energies see future PHOBOS publications.
53. Back, B. B. et al.: Collision geometry scaling of Au+Au pseudorapidity density from $\sqrt{s_{NN}} = 19.6$ to 200 GeV. Phys. Rev.C(R), 70, 2004. 021902.
54. for PHENIX Collaboration, A. B.: Charge particle multiplicity and transverse energy measurements in Au+Au collisions in PHENIX at RHIC. Nucl.Phys.A, (715):486–489, 2003.
55. J.Adams et al.: Production of charged pions and hadrons in Au+Au collisions at $\sqrt{s_{NN}} = 130$ GeV. 2003. arXiv:nuclex/0311017.
56. H.Satz: Limits of confinement:the first 15 years of ultra-relativistic heavy ion studies. Nucl.Phys.A, 715:3–19, 2003.
57. T.Alber et al.: . Phys.Rev.Lett., (75), 1995. 3814, Phenix divided the value by 1.1 to remove enhancement for head on collisions.
58. S.Kabana: A new interpretation of the QCD phase transition and of strangeness as QGP signature. 2001. arXiv:hep-ph/0111394.
59. Ansonage, R. E. et al.: Charged particle multiplicity distributions at 200 and 900 GeV c.m.energy. Z. Phys. C, 43:357–374, 1989.
60. Thome, W. et al.: Charged particle multiplicity distributions in pp collisions at ISR energies. Nucl. Phys.B, 129:365–389, 1977.
61. B.B.Back et al.: Scaling of charged particle production in d+Au collisions at $\sqrt{s_{NN}} = 200$ GeV. Submitted to Phys. Rev. Lett, 2004.
62. Aggarwal, M. M. et al.: . Eur. Phys. J. C, 18(651), 2001.

63. H.Appelhauser et al.: . Phys.Rev.Lett., (82), 1999. 2471.
64. S.F.Afanasiev et al.: . Phys.Rev.C, (66), 2002. 054902.
65. Kharzeev, D., Levin, E., and M.Nardi: The onset of classical QCD dynamics in relativistic heavy ion collisions. hep-ph/0111315.
66. Steinberg, P.: Universal behavior of charged particle production in heavy ion collisions. Nucl. Phys. A, 715, 2003.
67. Back, B. B. et al.: Charged hadron transverse momentum distributions in Au+Au collisions at $\sqrt{s_{NN}} = 200$ GeV. Phys.Lett.B, 578(297), 2004.
68. Back, B. B. et al.: Centrality dependence of charged hadron transverse momentum spectra in Au+Au collisions from $\sqrt{s_{NN}} = 62.4$ to 200 GeV. accepted to Phys.Rev.Lett., (nucl-ex/0405003), 2004.
69. M.Harrison, T.Ludlam, S.: RHIC project overview. Nucl.Instrum. and Methods A, 499:235–244, 2003.
70. M.Adamczyk et al.: The BRAHMS experiment at RHIC. Nucl.Instrum. and Methods A, 499:437–468, 2003.
71. K.Adcox et al.: PHENIX detector overview. Nucl.Instrum. and Methods A, 499:469–479, 2003.
72. K.H.Ackermann et al.: STAR detector overview. Nucl.Instrum. and Methods A, 499:624–632, 2003.
73. Milov, A.: Centrality and $\sqrt{s_{NN}}$ dependence of the $de_T/d\eta$ and $dn_{ch}/d\eta$ in heavy ion collisions at mid-rapidity. submitted to J Phys.
74. M.D.Baker: Error ellipses for scaled $dn/d\eta$ versus $\langle N_{part} \rangle$. private communication, 2004.

VITA**Aneta Iordanova**

CURRENT ADDRESS

Department of Physics
845 West Taylor Street
University of Illinois at Chicago
Chicago IL 60607
USA

e-mail: aiorda1@uic.edu

Phone: (312) 355-3809

Fax: (312) 996-9016

PERSONAL INFORMATION

Place of birth: Pavlikeni, Bulgaria

Date of birth: 11 July 1970

EDUCATION

Ph.D. Program in High Energy Nuclear Physics, August 1999–Present

University of Illinois at Chicago, Chicago, IL, USA

M.Sc. Nuclear and Particle Physics, April 1994

Sofia University, “Saint Kliment Ohridski”, Bulgaria

RESEARCH AND EXPERIENCE

Research Assistant - Department of Physics

University of Illinois at Chicago, Chicago, IL, USA

2001–Present

Teaching Assistant - Department of Physics

University of Illinois at Chicago, Chicago, IL, USA

1999-2001

Physics Lecturer - High School

Kariacem, Bulgaria

1994-1996

Physics Lecturer - Second English Language School

Sofia, Bulgaria

1994

AWARDS

- Student Travel Award for Research Presentation at internationally recognized conferences (Fall 2002).
- Student Travel Award for Research Presentation at internationally recognized conferences (Spring 2004).

PUBLIC TALKS

Collision geometry scaling of mid-rapidity charged particle multiplicity in PHOBOS from $\sqrt{s_{NN}}=19.6$ to 200GeV .

APS meeting, Division of Nuclear Physics, Chicago, IL (October 2004).

Measuring mid-rapidity multiplicity in PHOBOS

International workshop on particle multiplicity in relativistic heavy ion collisions, Bari, Italy (June 2004).

Collision geometry scaling of Au+Au pseudorapidity density from $\sqrt{s_{NN}}=19.6$ to 200GeV .

Brookhaven Seminar, BNL, NY (May 2004).

Npart determination for $\sqrt{s_{NN}}=200\text{GeV}$ d+Au collisions in PHOBOS

APS meeting, Division of Nuclear Physics, Arizona, NM (October 2003)

Energy and centrality dependence of mid-rapidity charged particle multiplicity measured in PHOBOS

APS meeting, Division of Nuclear Physics, Lansing, MI (October 2002)

POSTERS

Npart determination and systematic studies of $\sqrt{s_{NN}}=200\text{GeV}$ d+Au collisions in PHOBOS

Quark Matter 2004, Oakland, CA (January 2004)

Triggering in a Low Multiplicity environment

RHIC-AGS Users Meeting, Brookhaven National Laboratory, NY (May 2003)

Tracklet reconstruction at midrapidity in 19.6GeV Au+Au collisions

Quark Matter 2002, Nantes, France (October 2002)

PUBLICATIONS

Scaling of charged particle production in d+Au collisions at $\sqrt{s_{NN}}=200\text{ GeV}$ arXiv:nucl-ex/0409021 (*submitted Phys.Rev.Lett.*)PHOBOS Collaboration (B.B.Back *et al*)**Charged antiparticle to particle ratios near midrapidity in p+p collisions at $\sqrt{s_{NN}}=200\text{ GeV}$** arXiv:nucl-ex/0409003 (*accepted Phys.Rev.C*)PHOBOS Collaboration (B.B.Back *et al*)**Transverse momentum and rapidity dependence of HBT correlations in Au+Au collisions at $\sqrt{s_{NN}}=62.4$ and 200 GeV** arXiv:nucl-ex/0409001 (*submitted Phys.Rev.C*)PHOBOS Collaboration (B.B.Back *et al*)**Centrality and pseudorapidity dependence of elliptic flow for charged hadrons in Au+Au collisions at $\sqrt{s_{NN}}=200\text{ GeV}$** arXiv:nucl-ex/0407012 (*submitted Phys.Rev.C*)PHOBOS Collaboration (B.B.Back *et al*)**Energy dependence of elliptic flow over a large pseudorapidity range in Au+Au collisions at RHIC**arXiv:nucl-ex/0406021 (*submitted Phys.Rev.Lett.*)PHOBOS Collaboration (B.B.Back *et al*)**Pseudorapidity dependence of charged hadron transverse momentum spectra in d+Au collisions at $\sqrt{s_{NN}}=200\text{ GeV}$** Phys.Rev. C **70** 061901(R) (2004)PHOBOS Collaboration (B.B.Back *et al*)

Collision geometry scaling of Au+Au pseudorapidity density from $\sqrt{s_{NN}}=19.6$ to 200 GeV

Phys.Rev. C**70** 021902(R) (2004)

PHOBOS Collaboration (B.B.Back *et al*)

Centrality dependence of charged hadron transverse momentum spectra in Au+Au collisions from $\sqrt{s_{NN}}=62.4$ to 200 GeV

arXiv:nucl-ex/0405003 (*accepted* Phys.Rev.Lett.)

PHOBOS Collaboration (B.B.Back *et al*)

Particle production at very low transverse momenta in Au+Au collisions at $\sqrt{s_{NN}}=200$ GeV

Phys.Rev. C**70** 051901(R) (2004)

PHOBOS Collaboration (B.B.Back *et al*)

Pseudorapidity distribution of charged particles in d+Au collisions at $\sqrt{s_{NN}}=200$ GeV

Phys.Rev.Lett. **93** 082301(R) (2004)

PHOBOS Collaboration (B.B.Back *et al*)

Centrality dependence of charged antiparticle to particle ratios near midrapidity in d+Au collisions at $\sqrt{s_{NN}}=200$ GeV

Phys.Rev C**70** 011901(R) (2004)

PHOBOS Collaboration (B.B.Back *et al*)

Charged hadron transverse momentum distributions in Au+Au collisions at $\sqrt{s_{NN}}=200$ GeV

Phys.Lett. B**578** 297 (2004)

PHOBOS Collaboration (B.B.Back *et al*)

Centrality dependence of the charged hadron transverse momentum spectra in d+Au collisions at $\sqrt{s_{NN}}=200\text{GeV}$

Phys.Rev.Lett **91** 072302 (2003)

PHOBOS Collaboration (B.B.Back *et al*)

Comparison of the total charged-particle multiplicity in high-energy heavy ion collisions with e+e- and pp/pbar-p data

arXiv:nucl-ex/0301017 (*submitted* Phys.Rev.Lett.)

PHOBOS Collaboration (B.B.Back *et al*)

Significance of the fragmentation region in ultra-relativistic heavy ion collisions

Phys.Rev.Lett. **91** 052303 (2003)

PHOBOS Collaboration (B.B.Back *et al*)

Ratios of charged antiparticles to particles near mid-rapidity in Au+Au collisions at $\sqrt{s_{NN}}=200\text{GeV}$

Phys.Rev. **C67** 021901(R) (2003)

PHOBOS Collaboration (B.B.Back *et al*)

Pseudorapidity and centrality dependence of the collective flow of charged particles in Au+Au collisions at $\sqrt{s_{NN}}=130\text{GeV}$

Phys.Rev.Lett. **89** 222301 (2002)

PHOBOS Collaboration (B.B.Back *et al*)

Centrality dependence of the charged particle multiplicity near mid-rapidity in Au+Au collisions at $\sqrt{s_{NN}}=130$ and 200GeV

Phys.Rev. **C65** 061901(R) (2002)

PHOBOS Collaboration (B.B.Back *et al*)

Energy dependence of particle multiplicities near mid-rapidity in central Au+Au collisions

Phys.Rev.Lett. **88** 22302 (2002)

PHOBOS Collaboration (B.B.Back *et al*)

CONFERENCE PROCEEDINGS

Measuring mid-rapidity multiplicity in PHOBOS

J.Phys.G Conference Series **5** (2005) 97

A.Iordanova for the PHOBOS Collaboration